Effect of plasma on the Growth and Electronic properties of CNT and its Hybrid

THESIS SUBMITTED TO

DELHI TECHNOLOGICAL UNIVERSITY

FOR THE AWARD OF THE DEGREE OF

DOCTOR OF PHILOSOPHY

By

Ms. SHRUTI SHARMA

(2K18/PhD/AP/10)

Under the supervision of

PROF. SURESH C. SHARMA

DEPARTMENT OF APPLIED PHYSICS
DELHI TECHNOLOGICAL UNIVERSITY
SHAHBAD DAULATPUR, MAIN BAWANA ROAD,
DELHI-110042, INDIA

JULY 2024

Dedicated
To
My Loving Family

DELHI TECHNOLOGICAL UNIVERSITY

(Govt. of National Capital Territory of Delhi)
Shahbad Daulatpur, Bawana Road,
Delhi-110042

CERTIFICATE

This is to certify that the thesis entitled "**Effect of plasma on the Growth and Electronic properties of CNT and its Hybrid"** submitted by **Ms. Shruti Sharma (2K18/PhD/AP/10)** to Delhi Technological University (DTU), Delhi, India for the degree of Doctor of Philosophy, is a bonafide record of the research work carried out by her under my supervision and guidance. The work embodied in this thesis has been carried out in the Plasma & Nano Simulation Lab, Department of Applied Physics, Delhi Technological University (DTU), Delhi, India. The work of this thesis is original and has not been submitted in parts or fully to any other Institute or University for the award of any other degree or diploma.

Prof. Suresh C. Sharma
Supervisor
Professor,
Department of Applied Physics
Delhi-110042, India

Prof. A.S. Rao
Head of the department &
Professor,
Department of Applied Physics
Delhi- 110042, India

DELHI TECHNOLOGICAL UNIVERSITY

(Govt. of National Capital Territory of Delhi)
Shahbad Daulatpur, Bawana Road,
Delhi-110042

CANDIDATE'S DECLARATION

I, herby certify that the thesis titled **"Effect of plasma on the Growth and Electronic properties of CNT and its Hybrid"** submitted in the fulfilment of the requirements for the award of the degree of Doctor of Philosophy is an authentic record of my research work carried out under the supervision of **Prof. Suresh C. Sharma**. Any material borrowed or referred to is duly acknowledged.

Shruti Sharma
(2K18/PhD/AP/10)
Delhi Technological University
Shahbad Daulatpur, Bawana Road
Delhi-110042, India

ACKNOWLEDGEMENT

Above all, I express my genuine thanks to the Almighty and Shri Radhakrishna Ji for giving me immense strength and patience to work hard all these years.

I express my heartfelt gratitude to my grandparents, **Late Mr. Ram Kumar Sharma, Late Mrs. Angoori Devi, Late Mr. Shiv Kumar Sharma** and **Late Mrs. Savitri Sharma**. I believe that even from the heavenly abode, they showered me with their immense blessings and strength all these years. I know they would feel proud of their granddaughter.

I wholeheartedly want to thank my guide, **Prof. Suresh C. Sharma**, Professor, Department of Applied Physics for his excellent mentorship, research, patience, motivation, enthusiasm, immense knowledge and continuous support all these years. Without his persistent efforts and guidance, this thesis would not have been accomplished. His guidance helped me research and writing of this thesis. He is genuinely the best advisor and mentor.

My sincere thanks also goes to **Prof. Yogesh Singh**, *Ex-Hon'ble* Vice Chancellor, DTU, **Prof. Prateek Sharma** Hon'ble Vice-Chancellor, DTU and officials of DTU for their precious support and providing ample research facilities to conduct this research.

I would also thank **Prof. A.S. Rao**, Head of the Department of Applied Physics, DTU, and all other faculty and staff members for their help and cooperation throughout my research. Thanks to the **Department of Applied Physics, Delhi Technological University (DTU),** for providing the required facilities so that I can work voraciously, barring the time limit.

I express my gratitude to my seniors, **Dr. Neha Gupta, Dr. Ravi Gupta, Dr. Jyotsna Panwar, Dr. Monika Yadav, and Dr. Umang Sharma** for their valuable suggestions and continuous help during the initial stage of my research work. I would also like to express huge and warm thanks to my other fellow lab mates in Plasma & Nano Simulation Research Laboratory; **Ms. Anshu, Mr. Rajesh Gupta, Mr. Sagar Khanna, Ms. Jyoti, Mr. Harender Mor, Ms. Mansha Kansal, Mr. Aditya, Ms. Ritu, Ms. Monika and Mr. Himank,** for their scientific inputs, fruitful

discussions, motivation, and all the fun we had, kept me going in this challenging yet beautiful journey. Our fun in the last few years kept me sane during my ups and downs. Their personal and professional help, moral support and encouragement have put me at ease. The time I spent with them will remain a memorable golden time in my life. I also explicitly thank my colleague, **Mr. Ankush Dewan and Dr. Umang Berwal** for their generous support.

I want to pay high regard to my father, **Mr. Sanjay Sharma**, my mother, **Mrs. Kiran Sharma**, and my younger brothers **Mr. Laddu Sharma and Mr. Siddharth Sharma**, for their love, constant care, and emotional support throughout my life. Their faith, trust and confidence in me always pushed me toward my goal. I want to thank my husband, **Mr. Ashu Sharma,** for always being there and encouraging me when I lost optimism or felt disheartened. I owe a special thanks to my cousins **Ms. Neha Sharma, Ms. Sonakshi Sharma, Mr. Shaurya Sharma,** as without their love, patience and support in this challenging journey. I am also indebted to my lovely friend **Ms. Purva Gupta** for cheering me at every step.

I want to acknowledge the **Science and Engineering Research Board (SERB) – Department of Science and Technology (DST)**, **Government of India** for providing me with the necessary funding and fellowship to pursue research.

Shruti Sharma

ABSTRACT

CNT-Graphene hybrids are three-dimensional, densely packed carbon atoms organized hexagonally in a three-dimensional lattice. Vertically aligned hybrids are promising candidates for applications such as field emission devices, electronic sensors, and electron emission displays. There are several ways available for synthesizing hybrids; however, plasma-based techniques, such as plasma enhanced chemical vapour deposition (PECVD), are only utilized to manufacture vertically oriented hybrids at low temperatures. The purpose of this thesis is to gain a thorough understanding of the hybrid's growth mechanism in a reactive plasma environment, as well as the field emission characteristics that result.

In this paper, multiscale analytical models characterizing the growth mechanism of the CNT-graphene hybrid on the catalyst-substrate interface are created. The model for hybrid growth in plasma takes into account the hybrid's charging in the plasma, the particle and energy balance of the plasma species (charged and neutral), and the energy balance of the CNT and catalyst surface. For typical glow discharge plasma parameters, the model equations were solved simultaneously. Plasma parameters (number densities and temperatures of electrons and ions), as well as the presence of dopant species (nitrogen species), have been discovered to have a substantial impact on the hybrid's development characteristics and, as a result, its field emission properties.

The multistage model for plasma-assisted catalyzed hybrid growth consists mostly of two sub-analytical models. The plasma sheath model accounts for the excitation of gaseous sources caused by applied plasma power and plasma species kinetics, whereas the surface deposition model incorporates the adsorption and dissociation of carbon bearing species over the catalyst nanoislands active surface (free surface available for plasma species adsorption) to generate building species (carbon species) through a variety of surface processes, including the diffusion of building species over the catalyst nanoislands' surface, the production of carbon clusters, the nucleation and growth of graphene islands, and the vertical growth of hybrids. The model equations were solved using experimentally determined initial conditions. Plasma parameters, doping elements (nitrogen), gas flow rate, catalyst layer

thickness, substrate temperature, and cooling rate all have a significant impact on the hybrid's growth characteristics and, as a result, its field emission properties. Furthermore, it is assumed that graphene sheet formation over the CNT surface is defect guided, and that the density profiles of the defects formed over the CNT surface may be controlled by appropriately altering the plasma working parameters A thorough comparison of the acquired theoretical results to the available experimental observations verifies the current model's appropriateness.

The current thesis work can be extended to build thin and long vertically oriented hybrids for prospective uses in field emitters, as the hybrid's field emission characteristics are determined by its geometrical properties, i.e., height and thickness. Furthermore, the current study might be extended to evaluate the formation of additional carbon-based nanostructures.

List of Publications

International Journals

1 Shruti Sharma and Suresh C. Sharma "Effect of Plasma Control Parameters on the Growth of Nitrogen – Doped Nanocone - Vertical Graphene Hybrid : Theoretical Investigations" (2022) Plasma Chemistry and Plasma Processing 42: 413-433, doi: https://doi.org/10.1007/s11090-022-10229-3 (IF 2.99).

2 Shruti Sharma and Suresh C. Sharma " Analytical modelling of nucleation and growth of graphene layers on CNT array and its application in field emission of electrons" Physica Scripta Vol 99, Issue 7 (2024) (IF 2.9). https://doi.org/10.1088/1402-4896/ad4f6b

International peer reviewed proceedings

1 Shruti Sharma and Suresh C. Sharma, "Numerical analysis on H_2 plasma assisted growth of graphitic leaves on carbon nanotube," 2022 IEEE International Conference on Nanoelectronics, Nanophotonics, Nanomaterials, Nanobioscience & Nanotechnology (5NANO), Kottayam, India, 2022, pp. 1-3, doi: 10.1109/5NANO53044.2022.9828987.

International Conferences

1. 12^{th} International Conference on Plasma Science & Applications (ICPSA-2019), 11^{th}- 14^{th} November, 2019, Lucknow, India and presented poster titled " Role of Nitrogen Doping in the growth and field emission properties of CNT- Graphene Hybrid"
2. DST-SERB Sponsored 2022 IEEE International Conference on Nanoelectronics, Nanophotonics , Nanomaterials, Nanobioscience & Applications; Nanotechnology (5 NANO 2022), organised by Mangalam College of Engineering, Kottayam, Kerala, India on 28^{th} & 29^{th} April 2022 and presented paper titled " Numerical analysis on H_2 plasma assisted growth

of graphitic leaves on carbon nanotubes" with publication in conference proceedings.

3. 3^{rd} International Conference on Plasma Theory and Simulations (PTS-2023) 21-23 September, 2023, Organised by School of Physical Sciences, Jawaharlal Nehru University, New Delhi and presented poster titled " Optimizing the Cobalt film thickness for the growth of carbon nanotube with few layer graphene foliates".

CONTENTS

List of figures

Figure No. Page No.

Chapter: 1

Chapter: 2

Chapter 3:

Chapter 4:

List of tables

Table No. Page no.

Chapter 1:

Chapter 2:

Chapter 3:

Chapter 1

Introduction

Nanomaterials are anchors of nanoscience and nanotechnology. From the past few years, nanostructure science and technology is an extensive and integrative area of research and advancement. It has competence to modernize the techniques, the ways products are created, the range and functionalities that can be acquired. It is commercially significant which will surely upsurge in future. Nanomaterials are those substances whose at least one dimension is less than approximately 100 nanometers (100 millionth of a millimeter). They have a much greater surface area to volume ratio than their conventional forms, which can lead to greater chemical reactivity and affect their strength. Also at the nanoscale, quantum effect can become much more important in determining the materials properties and characteristics, leading to novel optical, electrical and magnetic behavior. Discovery of one dimensional (1-D) carbon nanotube (CNT) by Iijima [1] have captivated the scientists towards graphitic carbon nanostructures including fullerenes, graphene, nanodiamonds, nanoporous and their other derived forms. CNT and two dimensional (2-D) graphene owing to their remarkable properties among others are combined to create three dimensional (3-D) hybrid nanocarbons, which hold fascinating properties even better than they could on their own.

1.1 Graphene

Graphene is a 2-D material comprising monolayer of densely packed sp^2 hybridized carbon atoms forming six-membered rings. After 440 years of graphite invention, in 2004 graphene was explicitly prepared by peeling its single layer using sticky tape and pencil [2]. It is an elementary unit of other allotropes of carbon. Wrapped, rolled up, and stacked graphene generate zero dimensional (0-D) fullerenes, CNT, and stacked graphite [3].

Following a thorough examination of graphene's structure, scientists concluded that imperfections in the graphene sheet made it stable [4]. This demonstrates that graphene is not completely flat and has ripples (out of plane aberrations) on its surface. Mayer et al. [5] observed the ripples inside the graphene membrane.

1.2 Structure of Graphene

Shruti Sharma
Delhi Technological University

In the structure of graphene, six electrons encircling carbon atom nucleus follows electronic configuration $1s^2\ 2s^2\ 2p^2$. The outer 2s, $2p_x$, $2p_y$ orbitals contribute to sp^2 hybridization by forming three planar covalent σ bonds with neighbouring carbon atoms at an angle of 120° with respect to each other.

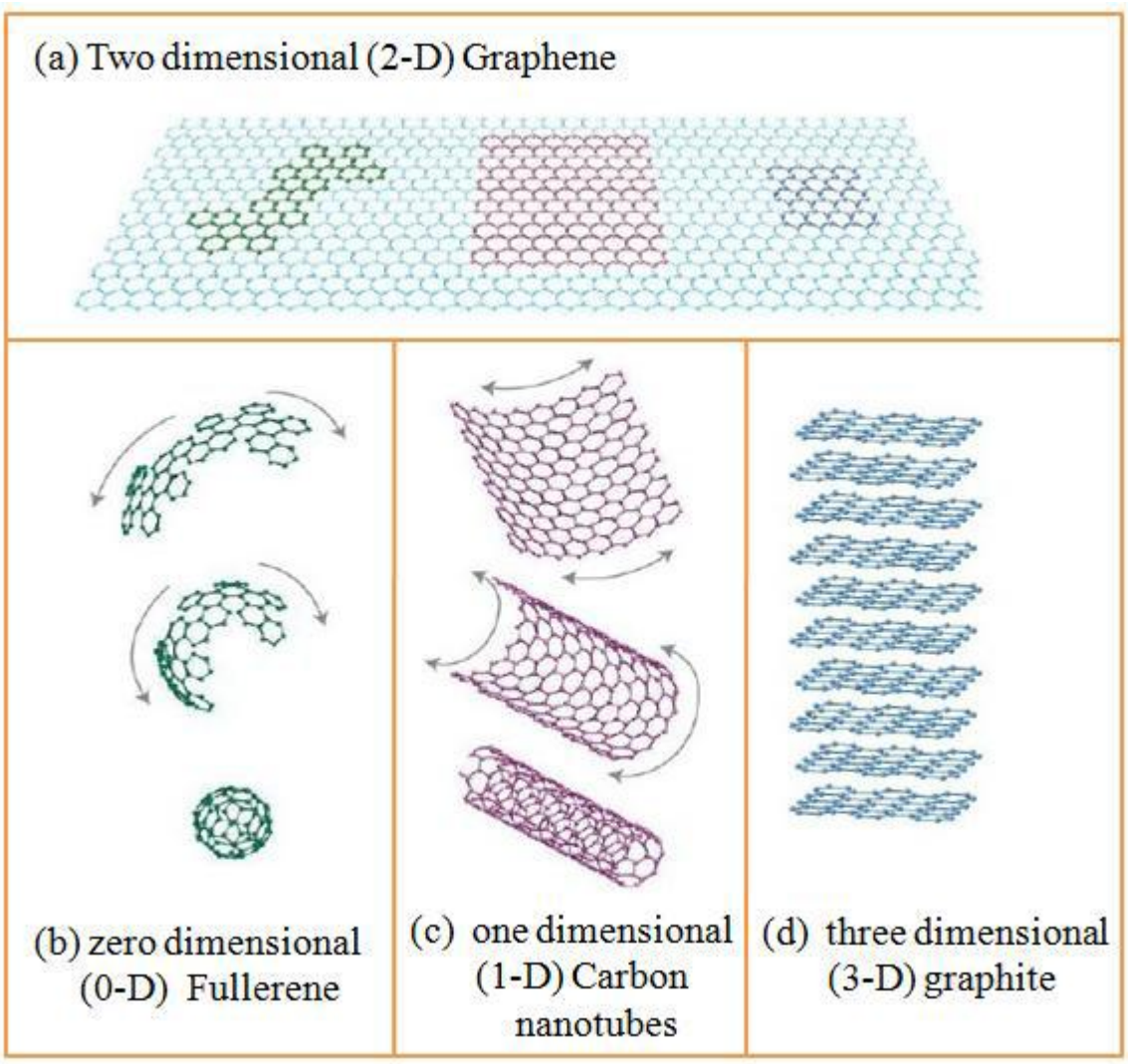

Figure 1.1 Transformation of two-dimensional graphene into different dimensional carbon nanostructures [3].

The remaining p_z orbital lies perpendicular to the three sp^2 orbitals, containing the free π electron that is responsible for unique electrical properties of graphene along with interaction between the stacked graphene sheets [6]

1.3 Properties of graphene

Graphene, ultra-thin (10^5 order thinner than human hair) possible material composed of single layer of carbon atoms in the form of hexagonal rings. Owing to the outstanding mechanical, electronic, chemical, thermal, and optical properties,

graphene gained the huge research attention in the field of physics and chemistry.

1.3.1 Mechanical Properties

Graphene is recognized as toughest 2-D material, much harder than either steel or diamond of the same dimension. With the same thickness, the strength of graphene is about 100 times the strength of steel- a $1m^2$ of graphene could withstand 4 kg of weight. In addition, considering elasticity, graphene can retain its original dimension after applied strain. Hone and coworkers measured the intrinsic strength of the monolayer graphene to be 42 N m^{-1}, which equates to an intrinsic strength of 130 GPa [7]. The stability of the sp2 bonds makes it mechanically exceptional. The parameters measuring graphene strength are listed in table 1.1.

Table 1.1 Parameters measuring graphene strength [8-9]

Parameters	Numerical value for graphene
Tensile strength	130GPa
Young's modulus	0.5 Tpa
Elastic limit	~20%
Thickness	0.35-1 nm

Owing to the impressive mechanical properties of graphene, it is employed as an individual material and as a reinforcing agent in composites [10].

1.3.2 Electronic properties:

Graphene is a semi-metal or zero - gap semiconductor with both holes and electrons as charge carriers [11]. In carbon, four electrons are available in the outermost shell for chemical bonding. In graphene, each carbon atom is bonded to three carbon atoms due to sp^2 hybridization, leaving one free electron (π electron) in the third dimension for electronic conduction. Attributing to ultrahigh mobility of $2 \times 10^5\ cm^2/Vs$, which is almost 140 times the silicon's mobility, graphene is the most conductive material so far at room temperature, with a conductivity of $10^6\ S/m$ and sheet resistance of $31\ \Omega/sq$ [12-13].

1.3.3 Chemical Properties

Graphene has a high surface –volume ratio and low mass density [14], allowing other atoms and molecules for adsorption or desorption to/from its surface. The p_z orbitals are accessible for chemical functionalization that could yield various graphene derivative. In addition, defects within the sheet increases the chemical reactivity. It is reported that single layer graphene is 100 times more chemically reactive than thicker multilayer sheets [15]. Under normal conditions graphene show inert behavior. However, it shows reactive nature when exposed to crucial reactive environment.

1.3.4 Thermal Properties

Specific heat and thermal conductivity are the parameters to determine the thermal properties of any material. Graphene's sp2 bonding between carbon atoms results in high in-plane thermal conductivity and weak van der Waals interaction among the adjacent graphene planes limits the out-of- plane heat flow. Thermal time constant (how quickly the body cools or heats) for single graphene sheet is 0.1 ns. Among any known material (diamond, graphite, graphene nano ribbons, graphene supported) freely suspended graphene has highest in-plane thermal conductivity o about 2000-4000 $Wm^{-1}K^{-1}$ at room temperature. Thermal conductivity of the pristine graphene can be reduced by introducing alterations or defects in it, making it suitable for thermoelectric applications, if the high electronic conduction of graphene can be preserved [16].

1.3.5 Optical Properties

The π bond in graphene determines its electronic and optical properties. Its 2-D electron confinement and exceptional band structure with zero band gap leads to fascinating interaction with electromagnetic radiation. Single layer thick graphene absorbs 2.3% of the incident light and negligible reflectance < 0.01%, wherein the absorption intensity is independent of incident light frequency. With each layer of graphene, the absorption increases in multiples of 2.3%. Owing to the unique optical properties, graphene has found potential application in photoluminescence and electromagnetic transport. [17-18]

1.3.6 Magnetic properties

Graphene is nonmagnetic, as all the electrons in the outermost orbit of carbon atoms are paired via σ and π bonds. Point defects such as vacancies, zigzag edges and chemical doping with magnetic impurities can bring about localized magnetic moment in graphene [19]. While maintaining its exceptional electronic properties Wang et al. to induce ferromagnetism, incorporated graphene sheet with the magnetic insulator (yttrium iron garnet) [20].

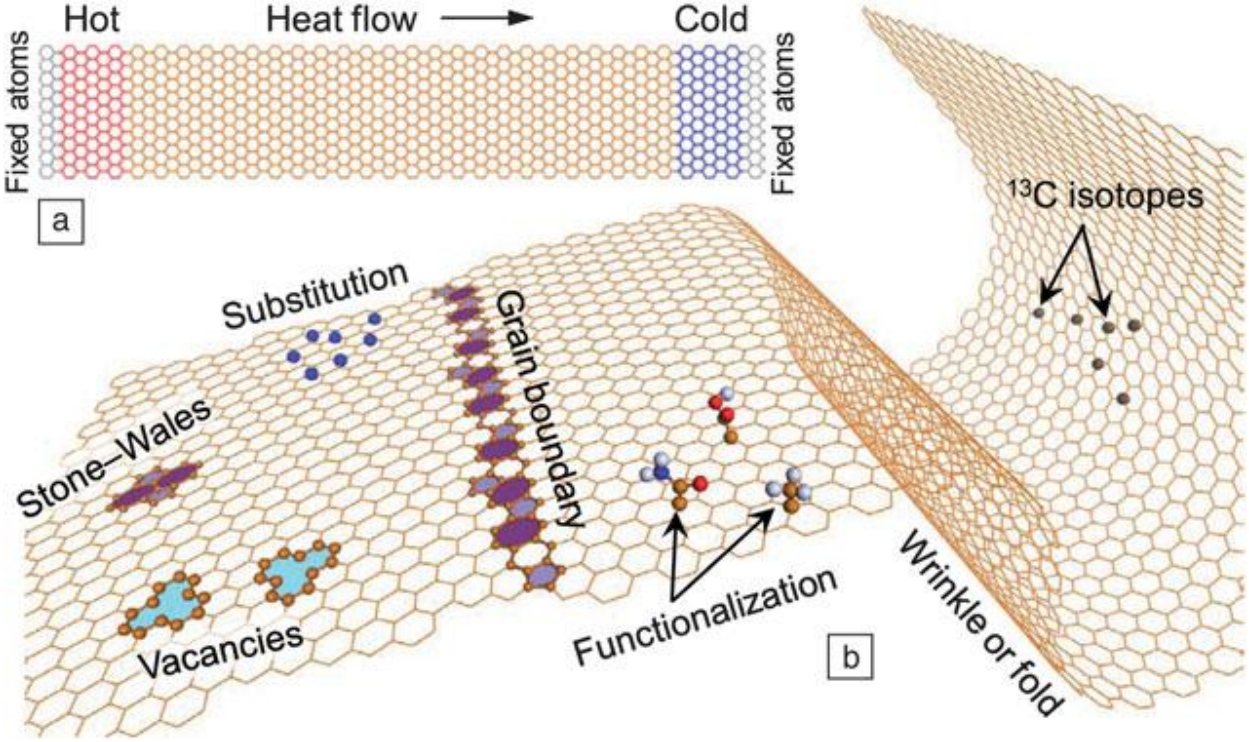

Figure 1.2 (a) Schematic of nonequilibrium molecular dynamics (NEMD) methodology for examining thermal transport in a GNR. (b) GNR showing different types of defects (vacancies, grain boundaries, Stone–Wales defects, substitutional and functionalization defects, and wrinkles or folds) that have a profound effect on tuning thermal transport in graphene [16]

1.4 Carbon Nanotubes

Carbon nanotube (CNT) can be described as elongated C_{60} molecule with rolled up hexagonal lattice in the form of cylinder. It is a single molecule of length tens of micrometer constituting millions of atoms with diameter in nano-meter range [21]. Iijima in 1991discovered Multiwalled carbon nanotubes (MWCNTs) using arc discharge evaporation method and later in 1993 he confirmed the presence of Single-walled carbon nanotubes (SWCNTs).

SWCNTs consists of single roll of graphene layer and MWCNTs are multiple roll of graphene layer with equalized spacing among the graphene cylinders and outer diameter nearly in the range 0.34 to 0.39 nm and 2 nm to 30 nm [22].

1.4.1 Structure of CNT

Based on wrapping of graphene layer in cylindrical form, SWCNTs can assume three different types of configurations such as armchair, chiral, zigzag defined by pair of indices (n,m) that comprise chiral vector, C = na_1+ma_2 (vector determining the direction of wrapping of graphene sheet), with n and m integers, a_1 and a_2 are the unit cell vectors of the graphene crystal lattice.

The diameter (d) of the CNT is represented by the relation d = $\frac{c}{\pi}$, where c is the circumference of the CNT and is given by th relation c=$|C|$=$a(n^2 + nm + m^2)^{0.5}$. The relation between length a and carbon- carbon bond length is given by $a = |a_1| = |a_2| = a_c\sqrt{3}$, where $a_c = 0.144nm$. Chiral angle (θ) the angle between zig-zag nanotube axis and chiral vector is calculated via $\theta = \tan^{-1}\{(m\sqrt{3})/(m + 2n)\}$. Hexagonal symmetry of the graphene lattice and chiral symmetry of the tubes restrict θ in the range $0^\circ \leq \theta \leq 30^\circ$. Both symmetric and asymmetric configuration (concerning to arrangement of circumferential hexagons) of the nanotube depend on the chiral angle θ. Zigzag nanotube (m=0 and θ =0°) and armchair nanotube (n=m and θ = 30°) make up symmetric configuration. Chiral nanotube (n ≠ m and $0^\circ < \theta < 30^\circ$) goes with asymmetric configuration. CNTs for which $|n - m|$ is multiple of 3 are metallic type and for semiconducting tubes $|n - m| = 3p \pm 1$ [23].

1.4.2 Electrical properties

The sp2 carbon-carbon bond gives CNTs extraordinary electrical properties. It performs as metal and semiconductor, wherein the band gap in semiconducting nanotube varies inversely with the diameter, ranging from 1.8eV to 0.18eV for small to large diameter SWCNT. Thus, CNTs have more conductivity than that copper, and some have conductivity equivalent to silicon [24]. Under ballistic conduction the lowest resistivity of SWCNT and MWCNT is measured out to be $10^{-6}\Omega$cm and $3 \times 10^{-5}\Omega$cm, manifesting CNTs better conductivity than copper at room temperature [25]. Janas et al. [26] reported an increase in electrical conductivity of CNTs by doping them with efficacious interhalogen (iodine monochloride or iodine monobromide) doping agents, due to the increase in number of holes and simultaneously preserving the highly conductive sp^2 carbon network . Its resistivity

decreases by 67% and 42% by doping iodine monochloride and iodine. Defect free individual CNT has more conductivity in comparison to CNT with various defects.

1.4.3 Thermal properties

CNTs have miraculous thermal properties. At room temperature thermal conductivity (K) of carbon nanotubes reaches≈3000-3500W/mK, exceeding diamond. Thermal conductivity in CNT is dominated via phonon conduction mechanism. As studied by Han et al. [27], thermal conductivity varies inversely

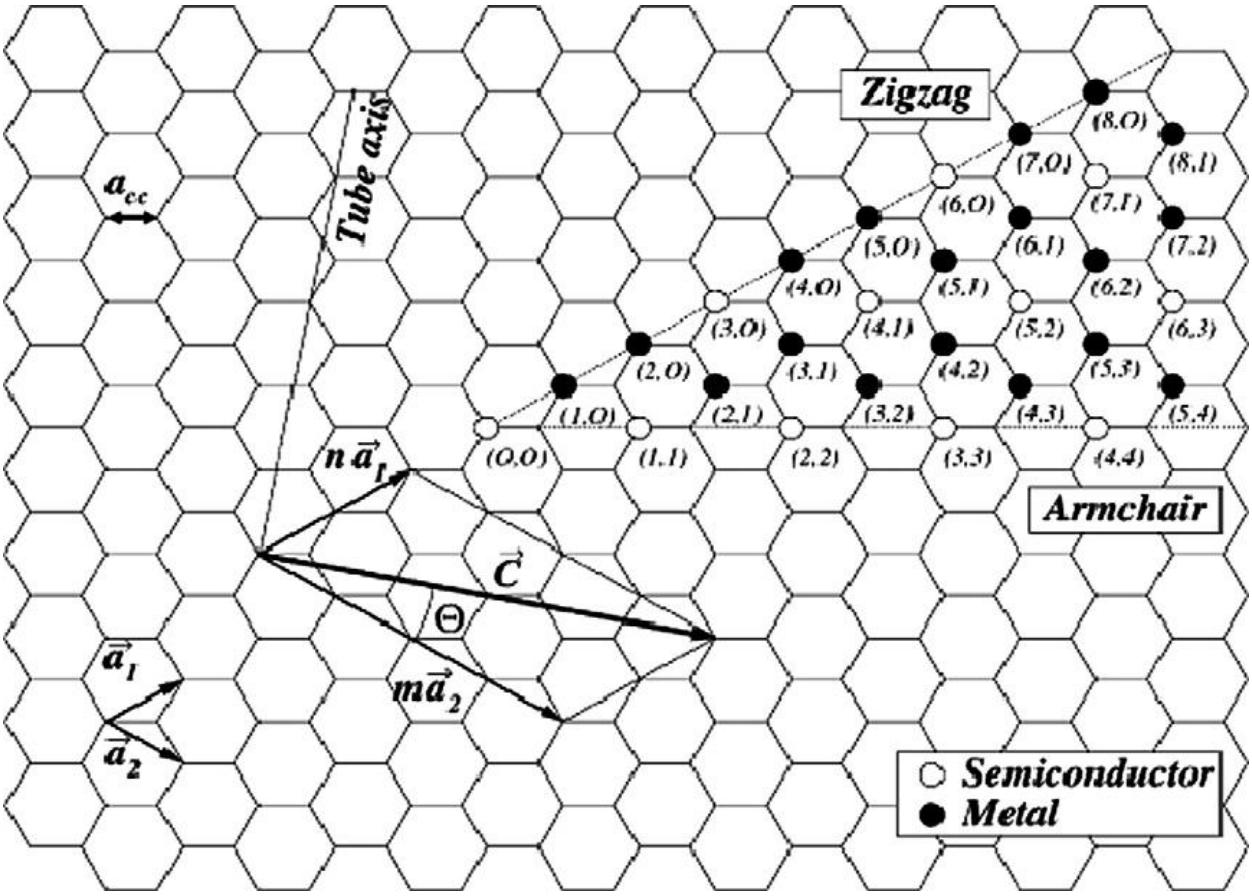

Figure 1.3 The 2D graphene sheet diagram showing a vector structure classification used to define CNT structure [23].

with the diameter of the tube, at room temperature MWCNT thermal conductivity is 500W/mK for an outer diameter of 28nm and 2069W/mK for a 10nm diameter. In addition, thermal conductivity increases with tube length and is likely to become

constant when tube length is much more than the mean free path of phonon. It decreases with increasing topological defects on the CNT as reported by Che et al. [28]. With temperature thermal conductivity first increases with peak at 320 K and then decreases owing to strong phonon-phonon umklapp scattering as observed by Kim et al.[29].

1.4.4 Mechanical Properties

CNTs are one of the tough and rigid materials yet discovered concerning tensile strength and elastic modulus. This toughness is due to sp2 covalent bonds formed between the carbon- carbon atoms. Its remarkably high Young's modulus of 1 Tpa and tensile strength approximate 60 GPa constitute them as ideal candidates for reinforcement of various materials like polymers. This shows that CNTs are more stiffer than steel with Young's modulus of about 0.2 Tpa and tensile strength about 0.38 GPa.

1.4.5 Optical properties

CNTs are both semiconducting and metallic depending on their twist, so they show interesting optical properties including excitonic effects in semiconducting carbon nanotubes, large optical nonlinearity in semiconducting species than metallic ones [30]. Bao et al. studied that in the entire visible band CNT array exhibit low reflectance and relatively high absorbance, longer tubes have higher absorbance because reflection from the bottom surface become weaker and fewer CNT array make the array less absorptive [31]. Owing to its high charge mobility as well as chemical inertness, CNTs have emerged as active materials to be incorporated in organic photovoltaics [32].

1.5 CNT- Graphene Composite

CNT – Graphene composite composes of a covalently bonded CNT and graphene. The combination of 2D graphene and 1D CNT generates a versatile 3D CNT–graphene hybrid with synergic properties. Since owing to strong van der Waals force the agglomeration of carbon materials specially graphene and CNTs is inevitable, which makes CNT-graphene hybrid superior over them by preventing agglomeration. The interconnected CNT – graphene are high surface area material with efficient electrical connections leading to high- performance supercapacitor devices [33] and enhanced mechanical strength of hybrid owes to strong π-π interaction between CNT – graphene [34].

1.5.1 Electrical Properties

The CNT- graphene hybrid/composite having the advantage of both the graphene (excellent FE stability) and the CNT (incomparable large aspect ratio) make them attractive candidates for high-performance field emitters. Deng et al. observed an enhancement in field enhancement factor (β=6244) of the hybrid in comparison to as grown CNT arrays β=4799 and an improved field emission stability [35]. The bond between CNT and graphene creates more charge transfer, upgrading the conductivity of the hybrid. Yusuf et al. reported 34.5 S/cm as the electrical conductivity of g-CNT hybrid, which is remarkably higher in comparison to CNT10 (4.76 S/cm) [36]. Because of hybrid's larger electron transfer capacity in comparison to graphene, they serve as great candidate for electrode in supercapacitors with specific capacitance of 290.4 Fg^{-1} wherein specific capacitance obtained using graphene as electrode is 175 Fg^{-1} [37].

1.5.2 Mechanical Properties

CNT- Graphene composite exhibits superior mechanical properties in comparison to CNT and graphene. This is attributed to π-π stack and covalent bond connections between CNT and graphene. Jyoti et al. studied that hardness and elastic modulus of the graphene oxide - CNT reinforced acrylonitrile-butadiene-styrene (ABS) polymer nanocomposite are 389.98±91.79 MPa and 7669.6±1179.12 MPa respectively which are considerably higher than Multiwalled CNT – ABS hardness 306.32±26.74 MPa and elastic modulus 6096.99±185.96MPa [38]. Owing to unique mechanical stability, the CNT-Graphene hybrid is employed as robust flexible electrode in energy storage devices [39].

1.5.3 Thermal Properties

Wrinkles and disconnections on the graphene layer deteriorate its thermal conduction performance. So owing to the interconnection between CNT and graphene, CNT-graphene hybrid exhibit enhanced thermal conductivity in comparison to them. Seo et al. reported exceptional critical heat flux (CHF) of graphene- CNT hybrid i.e .141.6 $^{kW}/_{m^2}$ representing it appropriate for high power density heating devices whereas CHF for graphene and CNT is 130.5 $^{kW}/_{m^2}$ and 123.0 $^{kW}/_{m^2}$ [40]. Lu et al. demonstrated the ultra-high thermal conductivity of

1388.7 W/mK for CNT- Graphene hybrid as CNT bridges the graphene layers preventing their corrugation due to strong π-π interactions consequently promoting phonon propagation [41].

1.5.4 Application of CNT –Graphene Composite

The CNT –Graphene composite are promising materials for the electric energy applications such as in batteries, cells, field emission devices.

1.5.4.1 Applications in electron emission devices

Field emission is a method for electron emission from material surface under the influence of external electric field. Owing the one-dimensional (1-D) nanomaterial geometry with high aspect ratio, sharp nanosize tip, and excellent electrical conductivity, CNT is considered a potential candidate for field emission (FE) devices. Furthermore, graphene is also a promising FE material due to atomic thin edges, unique two-dimensional shape and excellent FE stability. The CNT- graphene hybrid/composite having the advantage of both the graphene (excellent FE stability) and the CNT (incomparable large aspect ratio) make them attractive candidates for high-performance field emitters. By measuring emission current density at a turn on voltage, field emission properties of CNT-Graphene hybrid is evaluated. However, field enhancement factor characterizes field emission property of a material. Xu et al. have calculated the field enhancement factor of the Graphene – Double Walled Carbon Nanotube (DWCNT) Hybrid using Fowler-Nordheim (FN) equation; $J = A(\beta^2 E^2/\varphi)\exp(-B\varphi^{1.5}/\beta E)$, where constant A= $1.56 \times 10^{-6} AV^{-2}eV, B = 6.83 \times 10^{9} eV^{-1.5} Vm^{-1}$,β is the field enhancement factor, φ is the work function , E is the electric field. The value of the field enhancement factor is calculated from the slope of the high- field and low- field regions of the FN plot using the following equation $\beta = -(B\varphi^{1.5})/slope$. β for pure DWCNT is 10800, and increases to 27300 with increase of graphene ratio from 0 to 20% [42].

1.5.4.2 Applications in Fuel Cells

CNT – Graphene hybrid are used as carbonaceous support for platinum catalyst in Fuel cells. Hybrid supported platinum catalyst exhibits higher catalyst activity as compared to carbon black and CNT supported, as graphitic edges of hybrid boosts the reaction kinetics on Pt catalyst which is resisted by CNT side walls. High charge density and fast electron transfer of the graphitic edges ease the charge transfer

process on hybrid supported Pt catalyst. In addition its high crystallinity offers enhanced electrochemical stability compared to carbon black and CNT supported catalyst stability [43].

1.5.4.3 Application in Biosensors

Owing to 3D network, CNT-Graphene hybrid have large active surface area, high conductivity and fast electron transfer which makes it an efficient electrode in biosensors in comparison to reduced graphene oxide and CNT alone. They show good electrocatalytic activity toward the determination of biomolecules via excellent analytical parameters such as high sensitivity (137.9 mAM^{-1}), low detection limit (1 μM), wide sensor working range (10μM^{-1}mM) [44].

1.5.4.4 Application in rechargeable batteries

CNT –Graphene hybrid is used as potential candidate for anode materials in Li ion batteries. Graphene sheet boost faster ion diffusion on the surface, whereas the resistance faced by ions in moving from on sheet to the other is reduced by the high electrical conductivity of CNT as it bridges the gap among graphene sheets. Large interfacial area provided by hybrid between electrode and electrolyte improve the electrochemical performance in comparison to implementation via pristine graphene [45].

1.5.4.5 Application in gas sensors

The gas sensing mechanism is described as the adsorption and desorption of gaseous molecules on the surface, accompanying changes in the conducting properties. Taking into consideration the synergetic effect of CNT and graphene, CNT graphene hybrid is integrated in gas sensing devices wherein graphene provides mechanical flexible substrate withstanding extreme bending and CNT contributes in gas sensing which is larger and rapid than graphene [46].

1.5.5 Synthesis techniques of CNT – Graphene Hybrid

1.5.5.1 Layer-by-Layer (LBL) assembly

Patel et al. [47] reported LBL ultrasonic spray approach for hybridization of CNT and graphene. Coating of carbon nanomaterials of varying sizes and architectures is done on heated titanium substrate to activate in situ crosslink formation where

benzoyl peroxide is utilized as a free radical initiator to create crosslinks among the nanoparticles. Hong et al. [48] reported LBL hybridization via electrostatic interaction between positively and negatively charged CNT and graphene oxide sheets. CNTs maintain electrical contact with the graphene sheets providing electrical conductivity to hybrid as well as mechanical plasticity.

1.5.5.2 Dispersion Blending

Hummers method is employed to prepare Graphene oxide (GO) enhancing it with oxygen containing functional groups and making it water-soluble. CNT get agglomerates when suspended in water, therefore require surfactants. However, owing to π-π interaction between CNT and GO and its prominent dispersibility in water provide effective dispersion route omitting the use of surfactants [49].

1.5.5.3 Liquid Phase methods

This method include conventional techniques such as electrochemical, solution chemistry and hydrothermal methods. With regard to hydrothermal method, MWCNT with oxygen functional group on the surface and aqueously dispersed GO are mixed, then transferred and kept in autoclave for 12 hour at160℃. Finally, the hybrid mixture is washed and dried or 10 hour at 70℃ [50]. Owing to high defect density and weak interconnections obtained in final product, this method is not suitable for industrial production.

1.5.5.4 Thermal Chemical Vapour Deposition (TCVD)

TCVD is a key method for the synthesis of CNT and graphene. It is also employed for synthesizing CNT-Graphene hybrid. It is long established due to its low cost, high productivity, easy controllability, scalability. It is a gas phase heating process to activate the thermal decomposition of the precursor gases, generating radicals, ions and neutrals that diffuses over the catalyst surface to initiate the hybrid growth. The catalyst film deposited over the substrate owing to its high surface temperature (750℃ – 1200℃) get fragmented into nanoparticles. Commonly used catalyst in CVD for hybrid growth are Ni, Co, Fe. The following steps are involved in the growth of hybrid through TCVD [51-52].

1. To avoid the oxidation process, all gases inside the chamber are removed, and carbon precursors are then escorted into the TCVD chamber with inert gases like Ar, He.

2. Generated carbon species decompose into active carbon which then adsorb and diffuse on and into the catalyst.
3. Due to saturation of the catalyst nanoparticle, carbon atom diffuse out of the catalyst bulk and form graphene islands which coalescence to form graphene layer.
4. Vertical aligned MWCNT array start nucleating under continuous graphene layers, as carbon not bound in graphitic layers (free carbon) reach the catalyst surface.
5. Hydrogen atoms desorb from the hybrid surface and removed from the chamber as hydrogen molecules via carrier gases.

1.5.5.5 Plasma Enhanced Chemical Vapour Deposition (PECVD)

PECVD is a CVD process in which chemical reactions takes place after formation of plasma of reactive gases. In PECVD process, electron impact processes stimulate the gaseous reactants in the plasma and consequently, generating profusion of ions, radicals and neutral species. Electric ionization assisted energetic reactions at low temperature in plasma supersedes high temperature CVD technique. In plasma, energetic electrons dissociate the source gas molecules directing the generation of the highly energetic ions, and afterwards reactions between these highly energetic ions and gaseous sources begins to continue. Vertical hybrid growth is a convoluted process as gas phase and surface reactions involved in growth are biased by the plasma source and plasma operational parameters, eventually affecting the morphology and structure of as-grown vertical hybrid. Moreover, this method offers the advantage of low-temperature processing and higher growth selectivity. Gas pressure is kept low and source power is kept high to maintain the plasma inside the chamber. In the PECVD growth process, proper knowledge of the source of plasma excitation is essentially important. Few of the plasma source are, microwave (MW) plasma, radiofrequency (RF) plasma, direct current (DC) plasma, and combinations of them are used to ignite the plasma. The plasma sources with various sources gases and operating conditions are listed in Table 1.2.

1.5.5.5.1 DC- PECVD

Synthesis of graphite like nanostructure via DC-PECVD is reported by Obraztsov et al. [53]. Vertical hybrid growth employing DC- PECVD has been realized with two geometrical setups: parallel plate and pin to plate. In parallel plate DC glow discharge setup, between planar cathode and anode a dc voltage is applied. Space between the electrodes is filled with low-pressure gas for breakdown to eventuate.

Usually substrate is placed at cathode or it directly serves as cathode. The sheath electric field accelerates the ions towards the substrate and resulting electric force is responsible for alignment of the hybrid in vertical direction. In pin to plate DC glow discharge, asymmetric electrodes i.e. tungsten tip and a planar substrate prompts non-uniform plasma. Conductive substrate requirement is the main disadvantage of this technique. Y et al. have successfully synthesized branched carbon nanotubes using DC-PECVD.

1.5.5.5.2 RF-PECVD

Radio Frequency (RF) typically 13.56 MHz creates the plasma. RF-PECVD technique results in effective ionization of gas molecules, as electron density generated is higher in comparison to former DC- PECVD setup. The system work in three modes depending on coupling between the energy from RF generator and the plasma source: evanescent electromagnetic (H) mode, the propagating wave (W) mode, and the electrostatic (E) mode [54].

In H mode, Inductively Coupled Plasma (ICP), inductive coil antenna connected to RF generators are the plasma source. The inductive coils can be cylindrical or planar. Upon passing time varying electric field through coil antenna, time varying magnetic field is generated around the coil, which in turn induces electric current inside the chamber, leading to ionization of gases, hence production of high-density plasma.

In W mode, a propagating static magnetic field is introduced to a plasma excited by ICP with cylindrical circuit element. Resulting in the generation of plasma of larger volume and high energy density.

In E mode Capacitively Coupled Plasma (CCP), circular electrode is connected to RF voltage source and the other electrode is grounded, separating both the electrodes by 5 cm distance. Owing to comparable low electron energy and density, it cannot be used as independent plasma source. Gautier et al. [55] synthesized graphenated MWCNT via RF-PECVD technique.

1.5.5.5.3 MW-PECVD

MW-PECVD technique operates in electromagnetic radiation of frequency 2.54 GHz to dissociate source gas molecules via high-density energetic electrons. The MW source is coupled with vacuum heating chamber via transverse rectangular

cavity guide or using an external antenna, producing the electric field effect inside the chamber [56]. Plasma is created at high MW power and low pressure. Deng t al. [35] have studied the synthesis of graphene flake CNT composite employing MW-PECVD under varying plasma power (400W-800W). It is concluded that owing to rise in etching of C with increasing plasma power, the size and density of graphene flakes decreases and CNT array disappears at 800W.

Table 1.2 Overview of operating parameters used in the different PECVD systems

Source of plasma excitation	Gaseous sources	Operating pressure (Pa)	Substrate temperature (℃)	Flow rate (sccm)	Gas ratio	Ref.	
Microwave (MW)	CH_4/Ar	17.33	450-500	-	1:8	[57]	
(MW)	CH_4/N_2	5.32×10^3	1250	-	-	[58]	
(MW)	CH_4/N_2	5.32×10^3	>1000	-	-	[59]	
(MW)	$C_2H_2/N_2/Ar$	1.33×10^4	650-1050	200	0.5% of C_2H_2	[60]	
(MW)	$CH_4/N_2/Ar$	1.33×10^4	650-1050	200	4% of C_2H_2	[60]	
(MW)	CH_4/H_2	133	650-700	50	1:4	[61]	
(MW)	CH_4/H_2	220	550	-	1:20	[62]	
(MW)	CO/H_2	250	700	50	23:2	[63]	
(MW)	CH_4/H_2	5.32×10^3	700	200	1:8	[64]	
(MW)	$CH_4/H_2/Ar$	1.33×10^4	650	44	1:1:20	[65]	
(MW)	C_2H_2/NH_3	1.33×10^3	-	-	>1:1	[66]	
Inductively coupled plasma (ICP)	CH_4	12	630-830	10	-	[67]	
(ICP)	CH_4/Ar	0.3	400	30.4	16.4:14	[68]	
(ICP)	CH_4/H_2	12	630-830	10	>1:9	[67]	
(ICP)	CH_4/H_2	2.66-53.2	600-950	-	>1:19	[69]	
(ICP)	CH_4/H_2	13.33	700	10	2:3	[70]	
(ICP)	C_2H_2/H_2	4-5.33	550-600	5	4:1	[70]	
CCP+ICP	CH_4/H_2, CH_4/H_2, CHF_3/H_2, C_2F_6/H_2,	13.3	500	45	1:2	[71]	
Direct current (DC) glow	CH_4/H_2	1×10^4	1000	-	1:9	[72]	
DC glow	CH_4/H_2	9975	1000	-	8:92	[73]	
DC glow	CH_4/H_2	2.66×10^4	900-1000	50	3.8% of CH_4	[74]	
DC glow	$CH_4/H_2/Ar$	1.3	550-800	87	1:1.25:5	[75]	
DC glow	$CH_4/H_2O/Ar$	1.05×10^5	700	1500	10% of CH_4 with 40%	[76]	

						relative humidity		

1.6 Plasma and Formation of Plasma sheath

Plasma is generally called "the fourth of matter", in company with solid, liquid, gas. Just as a liquid will boil, changing into a gas when energy is added, heating a gas will form a plasma – a soup of positively charged particles (ions) and negatively charged particles (electrons). When the gas is heated to very high temperature (10,000°K or above), the constituting atoms, molecules gain immense high thermal energy and collide with each other , ripping away the electrons, consequently forming ions, electrons, neutrals and radicals species. The resultant ions, electrons, neutrals, and radicals are said to form the plasma or ionized gas. For every ionized gas to be referred to as plasma, quasineutrality and collective behaviour need to be satisfied [77]. According to quasineutrality condition, ion number density and electron number density are at equilibrium in plasma of length more than the Debye length (λ_D) i.e.,$l \gg \lambda_D$. The Debye length is a measure of how far into the plasma the potential of probe or electrode is realized and is expressed as $\lambda_D = \{\varepsilon_0 k_B T_e / n_e e^2\}^{\frac{1}{2}}$.

In plasma-aided growth of hybrid, the PECVD chamber is split into three regions: bulk plasma, plasma sheath, substrate surface. In bulk plasma quasineutrality condition is maintained comprising high density of electrons and positively charged species. Due to high thermal velocity of electrons $\left\{T_e/m_e\right\}^{0.5}$ than ions $\left\{T_i/m_i\right\}^{0.5}$ (because, $m_e \ll m_i$ and $T_e \gg T_i$) , electrons head faster towards the substrate generating negative potential on its surface, scooting bulk plasma with positively charged species hence net positive potential in bulk. Consequently setting up a strong electric field in region between bulk plasma and substrate surface, which accelerates the ions towards the substrate, reflecting back the electrons in bulk. This region of charge separation between bulk plasma and substrate surface is plasma sheath. To induce a strong electric field in plasma sheath region, a negative potential is also applied to the substrate surface.

1.7 Nucleation and growth of CNT- Graphene Hybrid

Initially, a catalyst thin film is deposited over the substrate surface, which after plasma treatment process (physical sputtering) or etching, transforms or breaks into catalyst nanoparticles. These catalyst nanoparticles act as nucleation seeds for the hybrid growth. The transition metal, iron (Fe), cobalt (Co) and nickel (Ni) are employed as catalyst thin film materials for hybrid synthesis. Plasma pretreatment of thin catalyst film allows better reaction between catalyst nanoparticles and C species. The hydrocarbon species adsorb and break on catalyst nanoparticle surface to generate C species and atomic radicals via various surface processes like thermal dissociation, ion – induced dissociation, adsorbed layer interaction [78] to initiate the CNT growth. The generated C species via surface and bulk diffusion regenerate into graphitic cylinder, which simultaneously get vertically aligned under the influence of plasma sheath electric field and other intermediate forces. After CNTs are formed, and with increase of reaction time, the energetic ions under the influence of sheath electric field continuously bombard the CNT surface, splitting C-C bonds, thereby creating cracks and dangling bonds (local defects). These defects act as nucleation sites for the growth of vertical graphene (VG) sheet. Carbon clusters accumulated at the defected sites diffuse and agglomerate to form graphene islands which further diffuse and agglomerate to form VG sheet normal to surface of CNT under the effect of sheath electric field and other inbuilt forces.

1.8 Analysis of plasma process parameters on the CNT-Graphene hybrid growth

Plasma process parameters: Plasma power, pressure, bias, precursor gases, substrate temperature, substrate involved, type of catalyst and catalyst thickness all influence the morphology of the carbon nanostructure along with growth of CNT –graphene hybrid. Below mentioned are the few studies on these parameters and their impact on the nanostructure morphology and CNT-Graphene hybrid growth.

Deng et al. [35] investigated that with C concentration the growth rate and density of graphene flakes on CNT increases and their distribution expand from tip to deep CNT forest. Moreover, with the increase of input plasma power graphene flakes size , density and amount of amorphous carbon on CNT surface decreases and with further increase in power (600 W) no graphene flakes are obtained and at 800 W CNT disappears. These morphological changes are attributed to plasma power related hydrogen etching on carbon. Field emission performance is significantly controlled by graphene flakes distribution, as CNT with densely distributed flakes show poor field emission property in comparison to CNT's with sparsely distributed graphene flakes on its surface.

Gorodetskiy et al. [79] performed hydrogen plasma modification on CNT array. Owing to enhanced plasma etching of the CNT array with increase of plasma treatment time, the average thickness of the CNT array decreases from 1760 μm to 1470 μm. With increase of plasma power from 1500 W to 3000 W the iron nanoparticles isolates out of the CNT channels owing to enhanced etching and form agglomerates or sinter into micron-sized iron balls under high power. Moreover with treatment of CNTs at 600 W amorphous carbon etches away with the formation of exfoliated graphene flakes at CNT surface and no iron nanoparticles were observed near the CNT tip.

Garg et al. [80] have studied the effect of increasing CH_4 partial pressure in PECVD chamber on the growth of single to few layer graphene flakes on Si nanowire mesh template. It is observed that size and density of the flakes increases with CH_4 partial pressure varying from 8.3mTorrr to 25mTorr. This is attributed to a decrease in H/C ratio in the gas feed. In addition the obtained hybrid material exhibits low resistance and exceptional conductivity owing to increase in density of single to few layer graphene flakes with CH_4 partial pressure.

Thapa et al. [81] simulated the electric field distribution for a single vertically aligned carbon nanotube (VACNT), an array of VACNTs and bundled CNTs with different number of CNT. The local electric field at the tip of VACNT (455V/μm) was found to be extreme in comparison to the field distribution (188 V/μm) at the tip of emitters in VACNT array. This is attributed to the screening effect from the neighbouring CNTs leading to weak penetration of equipotential lines between the VACNT emitters. The local electric field at the tip of emitters in bundled CNTs (9 CNTs) is found to be 355 V/μm, this remarkable amelioration in the local electric field is attributed to increased inter-bundle distance (0.9 μm) lowering the screening effect. Consequently, bundled CNT emitters can deliver better field emission performance as compared to that from dense CNTs emitters.

Qi et al. [82] studied the effect of Co catalyst and catalyst film thickness being crucial for the growth states and morphology of the vertically oriented few layer graphene (V-FLG). Slow growth rate and lower density of V-FLG is realized on substrates without catalysts compared to dense V-FLG obtained on catalyst film coated substrate under the same experimental conditions. As the thickness increases to 14 nm, CNT coated with densely packed FLG morphology is obtained. Growth of FLG on graphene is defect mediated. Furthermore, at catalyst thickness of 200nm only FLG morphology is obtained with no CNTs.

1.9 Objective and organization of thesis

Following the literature and studies appertain to growth of CNT- Graphene hybrid in plasma and field emission from them, the present thesis direct towards modelling and analyzing the growth and field emission properties of CNT –Graphene hybrid. The outcome of plasma control parameters such as total gas pressure , plasma power ,substrate temperature on the hybrid growth and its field emission properties is scrutinized in present thesis along with effect of H_2 gas flow rate, catalyst film thickness on the hybrid growth. Furthermore, CNT- Planar Graphene Layer (PGL) hybrid is modeled and explored under varying conditions. The entire work in present thesis is divided into five chapters.

Chapter 2 incorporates modelling of Vertical nanocone –Graphene hybrid via PECVD technique in C2H2/NH3 environment. The growth of hybrid is analyzed by altering the plasma control parameters viz. total gas pressure, plasma power. The parameters effect the ion and neutral density in plasma sheath, consequently altering the sputtering yield and etching phenomenon. Consequently the obtained dimensions of hybrid corresponding to preferable plasma power is employed to compute its field enhancement factor to be used as efficient field emission source.

Chapter 3 accounts for modelling the growth of CNT array with precipitation of planar graphene layers (PGL) on its top (CNT-PGL hybrid) in PECVD chamber in C_2H_2/NH_3 plasma. Varying neutral density in bulk plasma, ion and neutral flux to the catalyst film surface owing to different C2H2 gas flow rate, varying catalyst film thickness, substrate temperature, and cooling rate, all engineer the geometry of the CNT-PGL hybrid. Thus obtaining the optimized conditions which are suitable for the growth of CNT-PGL hybrid to be used as efficient field emission source in field emission devices. In addition the field enhancement factor of CNT array and CNT –PGL hybrid are compared to redeem the refined field emission properties.

Chapter 4: This chapter features two different plasma environments. In case 1, C_xH_y/H_2 plasma is used to numerically analyze the effect of H2 gas under varying plasma power on the growth of CNT with graphitic leaves over it. It is observed that with increase of plasma power the growth rate of CNT along with graphene decreases. In case 2, CH_4/Ar plasma is considered. The growth of CNT adorned with graphene foliates; under varying Co catalyst film thickness is investigated. It is found that morphology of the carbon nanomaterial varies with the catalyst film

thickness. The analyses are performed by solving the first-order simultaneous differential equations using experimentally determined initial conditions and plasma glow discharge parameters. Efficient field emission devices can then be designed by employing CNT-G hybrid obtained at optimized plasma power and catalyst film thickness.

Chapter 5: The final chapter includes the thesis' conclusion and future study scope. It discusses future work that can be performed to explore plasma-assisted growth of CNT-G hybrid more extensively and effectively in order to make its production more accessible and improve its applicability in numerous industries.

References

[1] S. Iijima (1991), Nature **354**, 56. https://doi.org/10.1038/354056a0

[2] Novoselov KS, Geim AK, Morozov SV, Jiang D, Zhang Y, Dubonos SV, Grigorieva IV, Firsov AA (2004), Science **306**, 666–669. https://doi.org/10.1126/science.1102896

[3] Rao CNR, Biswas K, Subrahmanyam KS, Govindaraj A (2009), J. Mater. Chem **19**, 2457 https://doi.org/10.1039/b815239j

[4] Warner JH, Fan Y, Robertson AW, He K, Yoon E, Lee GD, (2013), Nano Letters **13**, 4937. https://doi.org/10.1021/nl402902q

[5] Meyer JC, Geim AK, Katsnelson MI, Novoselov KS, Booth TJ, Roth S, (2007), Nature **446**, 60. https://doi.org/10.1038/nature05545

[6] Zhen, Z, Zhu H, (2018), Graphene **2018**, 1-12. https://doi.org/10.1016/B978-0-12-812651-6.00001-X

[7] Lee C, Wei XD, Kysar JW, Hone J, (2008), Science **321**, 385-388. https://doi.org/10.1126/science.1157996

[8] Celasco E, Chaika AN, Stauber, T, Zhang M, Ozkan C, Ozkan U, Palys, B, Harun SW (2019), Handbook of Graphene, https://doi.org/10.1002/9781119468455

[9] Dash S, Patnaik A, (2008), Microw Opt Techn Let 60, 1183-1187, https://doi.org/10.1002/mop.31127

[10] Papageorgiou DG, Kinloch IA, Young RJ, 2017, Prog Mater Sci, **90** 75–127. https://doi.org/10.1016/j.pmatsci.2017.07.004

[11] Radadiya TM, 2015, A Properties of Graphene, EJMS, **2**, 6-18

[12] KS Kim, Zhao Y, Jang H, Lee SY, Kim JM, Kim KS, Ahn JH, Kim P, Choi JY, Hong BH, 2009, Nature **457**,706-710, https://doi.org/10.1038/nature07719

[13] Bolotin KI, Sikes KJ, Jiang Z, Klima M, Fudenberg G, Hone J, Kim P, Stormer HL,et al., 2008, Solid State Commun. **146**, 351-355, http://dx.doi.org/10.1016/j.ssc.2008.02.024

[14] Xu Z, (2018), Graphene, 73–102, http://dox.doi.og/10.1016/B978-0-12-812651-6.00004-5

[15] Gabrielsen P, Stanford University, Thinnest graphene sheets react strongly with hydrogen atoms; thicker sheets are relatively unaffected **http://phys.org/news/2013-02-thinnest-graphene-sheets-react-strongly.html**

[16] Pop E, Varshney V, Roy AK, (2012), MRS Bulletin 37, 1273-1281, https://doi.org/10.1557/mrs.2012.203

[17] Kavitha MK, Jaiswal M, (2016), Graphene: A review of optical properties and photonic applications AJP 25, 809-831

[18] Wang J, Ma F, Liang W, Wang R, Sun M. (2017), Nanophotonics, **6**, 943-976. https://doi.org/10.1515/nanoph-2017-0015

[19] Tang N, Tang T, Pan H, Sun Y, Chen J, Du Y, (2020), Magnetic properties of graphene Spintronic 2D Materials, 137–161 https://doi.org/10.1016/B978-0-08-102154-5.00005-9

[20] Wang Z, Tang C, Sachs R, Barlas Y, Shi J, (2015), Phys Rev Lett **114**, 016603, https://doi.org/10.1103/PhysRevLett.114.016603

[21] Saifuddin N, Raziah AZ, Junizah AR, (2013), J Chem, 676815, 18 pages, 2013. https://doi.org/10.1155/2013/676815

[22] Rouf SA, Usman Z, Masood HT, Majeed, AM, Sarwar M, & Abbas W (2021). Synthesis and Purification of Carbon Nanotubes. Carbon Nanotubes - Redefining the World of Electronics, IntechOpen, http://doi.org/10.5772/intechopen.98221

[23] Aqel A, El-Nour KMMA, Ammar RAA Al- Warthan A, (2012), Arabian Journal of Chemistry 5, 1-23. https://doi.org/10.1016/j.arabjc.2010.08.022

[24] Li QW, Li Y, Zhang XF, Chikkannanavar SB, Zhao YH, Dangelewicz AM, Zheng LX, Doorn SK, Jia QX, Peterson DE, Arendt PN, Zhu YT (2007), Adv Mater, **19** 3358–3363 https://doi.org/10.1002/adma.200602966

[25] Janas D Milowska KZ, Bristowe PD, Koziol, KKK. (2017), Nanoscale, **9**, 3212–3221. https://doi.org/10.1039/C7NR00224F

[26] Han Z, Fina A, (2011), Prog Polym Sci 36 914–944. https://doi.org/10.1016/j.progpolymsci.2010.11.004

[27] Che J, Çagin T, Goddard WA (2000), Nanotechnology, **11**, 65 – 69. https://doi.org/10.1088/0957-4484/11/2/305

[28] Kim P, Shi L, Majumdar A, McEuen PL (2001), PRL, 87, 215502, https://doi.org/10.1103/PhysRevLett.87.215502

[29] Excitons in carbon nanotubes: Linear and nonlinear optical properties – Optical properties of carbon nanotubes http://homes.nano.aau.dk/tgp/nanotube%20research.pdf last visited 28.06.2024

[30] Bao H, Ruan X, Fisher TS (2010), Optics Express, **18**, 6347-6359, https://doi.org/10.1364/OE.18.006347

[31] Aurisicchio C, Marega R, Corvaglia V, Mohanraj J, Delamare R, Vlad DA, Kusko C, Dutu CA, Minoia A, Deshayes G, Coulembier O, Melinte S, Dubois P, Lazzaroni R, Armaroli N, Bonifazi D (2012) Adv Funct Mater 22: 3209- 3222. https://doi.org/10.1002/adfm.201102632

[32] Zhu Y, Li L, Zhang C, Casillas G, Sun Z, Yan Z, Ruan G, Peng Z, Raji ARO, Kittrell C, Hauge RH, Tour JM, (2012), Nat Commun **3**, 1225. https://doi.org/10.1038/ncomms2234

[33] Fan W, Zhang L, Liu T, (2016), Graphene-Carbon Nanotube Hybrids for Energy and Environmental Applications. SpringerBriefs in Molecular Science, Springer, Singapore. 21–51. http://doi.org/10.1007/978-981-10-2803-8_2

[34] Deng JH, Cheng GA, Zheng RT, Yu B, Li GZ, Hou XG, Zhao ML, Li DJ, (2014), Carbon 67, 525-533. https://doi.org/10.1016/j.carbon.2013.10.025

[35] Yusuf Y, Shafie S, Ismail I, Ahmad F, Hamidon MN, Pandey Sudhir PS, Wei L (2023) Pertanika Journal of Science & Technology, 31, https://doi.org/10.47836/pjst.31.3.12

[36] Du W, Ahmed Z, Wang Q, Yu C, Feng Z, Li G, Zhang M, Zhou C, Senegor R, Yang YC (2019) 2D Materials, 6, http://doi.org/10.1088/2053-1583/ab41d3

[37] Jeevan J, Arya AK, Chockalingam S, Yadav SK.; Subhedar KM.; Dhakate SR, Singh BP (2020), J Polym Res, 27, 282, http://doi.org/10.1007/s10965-020-02252-9

[38] Qin S, Liu Y, Jiang H, Xu Y, Shi Y, Zhang R, Wang F, (2019), Sci China Inf Sci 62, 220403, https://doi.org/10.1007/s11432-019-2676-x

[39] Seo H, Yun HD, Kwon SY, Bang IC , In Cheol, (2016) Nano Letters, 16, 932-938 https://doi.org/10.1021/acs.nanolett.5b03832

[40] Lu H, Zhang J, Luo J, Gong W, Li C, Li Q, Zhang K, Hu M, Yao Y, (2017), Compos Part A- Appl S, 102, 1-8 https://doi.org/10.1016/j.compositesa.2017.07.021

[41] Xu J, Feng T, Chen Y, Sun Z, (2013), J Nanomater 2013, 536302, https://doi.org/10.1155/2013/536302

[42] Pham KC, McPhail DS, Mattevi C, Wee ATS, & Chua DHC (2016), J Electrochem Soc, 163, F255–F263, http://doi.org/10.1149/2.0891603jes

[43] Mani V, Chen SM, Lou BS, (2013), Int J Electrochem Sci, **8**, 11641 – 11660, https://doi.org/10.1016/S1452-3981(23)13212-3

[44] Vinayan, BP, Nagar R, Raman V, Rajalakshmi N, Dhathathreyan KS, Ramaprabhu S (2012), J Mater Chem, **22**, 9949–9956, http://doi.org/10.1039/C2JM16294F

[45] Jeong HY, Lee DS, Choi HK; Lee DH, Kim JE, Lee JY, Lee WJ, Kim SO, Choi SY (2010), **96,** 213105, http://doi.org/10.1063/1.3432446

[46] Patel SC.; Alam O, Zhang D, Grover K; Qin YX, Sitharaman B, (2017), J Mater Res, **32**, 370–382, http://doi.org/10.1557/jmr.2016.472

[47] Hong TK, Lee DW, Choi HJ., Shin HS, & Kim BS, (2010) ACS Nano, **4**, 3861-3868, https://doi.org/10.1021/nn100897g

[48] Qiu L, Yang X, Dr. Gou X, Dr. Yang W, Prof. Ma ZF, Prof. Wallace GG, Dr. Li D (2010), Chem Eur J, 16, 10653–10658, https://doi.org/10.1002/chem.201001771

---

[49] Rajesh D, Mahendiran C, Suresh C, Pandurangan A, Maiyalagan T, (2019) Int J Hydrogen Energy 44, 4962-4973 https://doi.org/10.1016/j.ijhydene.2019.01.025

[50] Liu H, Liu Y, (2017), Phys Sci Rev, **2**, 20160107, https://doi.org/10.1515/psr-2016-0107

[51] Matsuoka Y, Clark IT, Yoshimura M, 2011, J Vac Sci and Technol B **29**, 061801 https://doi.org/10.1116/1.3644494

[52] Obraztsov AN, Volkov AP, Nagovitsyn KS, Nishimura K, Morisawa K, Nakano Y, Hiraki A, (2002) J Phys D: Appl Phys **35**, 357, https://doi.org/10.1088/0022-3727/35/4/311

[53] Bo Z, Yang Y, Chen J, Yu K, Yan J, Cen K, (2013), Nanoscale **5**, 5180-5204, https://doi.org/10.1039/C3NR33449J

[54] Gautier LA, Borgne VL, Khakani MAE, (2016) Carbon, 98, 259–266 https://doi.org/10.1016/j.carbon.2015.11.006

[55] Santhosh NM, Filipič G; Tatarova E, Baranov O, Kondo H, Sekine M, Hori M, Ostrikov K; Cvelbar, U, (2018), Micromachines, 9, 565, https://doi.org/doi:10.3390/mi9110565

[56] Wang ZP, Shoji M, Ogata H, (2011), Appl Surf Sci, **257**, 9082, https://doi.org/10.1016/j.apsusc.2011.05.104

[57] Soin N, Roy SS, Lim TH, McLaughlin JAD, (2011), Mater Chem Phys **129**, 1051-1057, https://doi.org/10.1016/j.matchemphys.2011.05.063

[58] Shang NG, Papakonstantinou P, McMullan M, Chu M, Stamboulis A, Potenza A, Dhesi SS, Marchetto H, (2008), Adv Funct Mater **18**, 3506-3514, https://doi.org/10.1002/adfm.200800951

[59] K. Teii K, S. Shimada S, M. Nakashima M and A. T. H. Chuang ATH, (2009), J Appl Phys **106**, 084303, https://doi.org/10.1063/1.3238276

[60] Wu YH, Qiao PW, Chong TC, Shen ZX, (2002), Adv Mater **114**, 64, https://doi.org/10.1002/1521-4095(20020104)14:1%3C64::AID-ADMA64%3E3.0.CO;2-G

[61] Y. Zhang, J. Du, S. Tang, P. Liu, S. Deng, J. Chen and N. Xu, (2012), Nanotechnology **23**, 015202, https://doi.org/10.1088/0957-4484/23/1/015202

[62] T. Mori, M. Hiramatsu, K. Yamakawa, K. Takeda and M. Hori, (2008), Diamond Relat. Mater.**17**, 1513, https://doi.org/10.1016/j.diamond.2008.01.070

[63] A. Malesevic, R. Vitchev, K. Schouteden, A. Volodin, L. Zhang, G. Van Tendeloo, A. Vanhulsel and C. Van Haesendonck, Nanotechnology **19**, 305604 (2008). https://doi.org/10.1088/0957-4484/19/30/305604

[64] L. Y. Zeng, D. Lei, W. B. Wang, J. Q. Liang, Z. Q. Wang, N. Yao and B. L. Zhang, (2008), Appl. Surf. Sci. **254**, 1700, https://doi.org/10.1016/j.apsusc.2007.07.131

[65] A. T. H. Chuang, B. O. Boskovic and J. Robertson, (2006), Diamond Relat. Mater. **15**, 1103, https://doi.org/10.1016/j.diamond.2005.11.004

[66] J. J. Wang, M. Y. Zhu, R. A. Outlaw, X. Zhao, D. M. Manos, and B. C. Holloway, (2004), Carbon **42**, 2867, https://doi.org/10.1016/j.carbon.2004.06.035

[67] M. Hiramatsu, K. Shiji, H. Amano and M. Hori, (2004), Appl. Phys. Lett. **84**, 4708, https://doi.org/10.1063/1.1762702

[68] M. Zhu, J. Wang, B. C. Holloway, RA. Outlaw, X. Zhao, K. Hou, V. Shutthanandan, and D. M. Manos, (2007), Carbon **45**, 2229-2234, https://doi.org/10.1016/j.carbon.2007.06.017

[69] M. Y. Zhu, R. A. Outlaw, M. Bagge-Hansen, H. J. Chen, and D. M. Manos, (2011), Carbon **49,** 2526-2531, https://doi.org/10.1016/j.carbon.2011.02.024

[70] K. Shiji, M. Hiramatsu, A. Enomoto, M. Nakamura, H. Amano, and M. Hori, (2005), Diamond Relat. Mater. **14**, 831-834, https://doi.org/10.1016/j.diamond.2004.10.021

[71] A. N. Obraztsov, A. A. Zolotukhin, A. O. Ustinov, A. P. Volkov, Y. Svirko and K. Jefimovs, (2003), Diamond Relat. Mater. **12**, 917-920, https://doi.org/10.1016/S0925-9635(02)00338-2

[72] N. Jiang, H. X. Wang, H. Zhang, H. Sasaoka, and K. Nishimura, (2010), J. Mater. Chem. **20**, 5070-5073, https://doi.org/10.1039/C0JM00446D

[73] V. A. Krivchenko, V. V. Dvorkin, N. N. Dzbanovsky, M. A. Timofeyev, A. S. Stepanov, A. T. Rakhimov, N. V. Suetin, O. Y. Vilkov, and L. V. Yashina, (2012), Carbon **50**, 1477-1487, https://doi.org/10.1016/j.carbon.2011.11.018

[74] S. Kurita, A. Yoshimura, H. Kawamoto, T. Uchida, K. Kojima, M. Tachibana, P. Molina-Morales, and H. Nakai, (2005), J. Appl. Phys. **97**, 104320, https://doi.org/10.1063/1.1900297

[75] Z. Bo, K. H. Yu, G. H. Lu, P. X. Wang, S. Mao and J. H. Chen, (2011), Carbon **49**, 1849-1858, https://doi.org/10.1016/j.carbon.2011.01.007

[76] J. A. Bittencourt, *Fundamentals of Plasma Physics* (Springer-Verlag, New York 2004)

[77] Denyenko I, Ostrikov K, Yu MY, Azarenkov NA, (2007), J Appl Phys, 102, 074308, https://doi.org/10.1063/1.2786058

[78] Gorodetskiy DV, Gusel'nikov, AV, Kurenya, AG, Smirnov DA, Bulusheva, LG, Okotrub, AV, (2020), *Materials* ***13***, 4420, https://doi.org/10.3390/ma13194420

[79] Garg R, Rastogi SK, Lamparski M, Barrera SC de la, Pace GT, Nuhfer NT, Hunt BM, Meunier V, Karni TC (2017), *ACS Nano* 11,6301-6311, https://doi.org/10.1021/acsnano.7b02612

[80] Thapa A, Jungjohann KL, Wang X, Li W, (2020), J Mater Sci **55**, 2101–2117 https://doi.org/10.1007/s10853-019-04156-6

[81] J. L. Qi JL, F. Zhang F, X. Wang X, L. X. Zhang LX, J. Cao J, J. C. Feng JC, *(2014), RSC Adv 4* , 44434-44441 http://doi.org/10.1039/C4RA08109A

Chapter 2

Effect of Plasma Control Parameters on the Growth of Nitrogen‑Doped Nanocone‑Vertical Graphene Hybrid: Theoretical Investigations

2.1 Brief Outline

In the present chapter, a phenomenological model describing the growth of nitrogen-doped nanocone-vertical graphene hybrid (N-NCN-VG) is developed. The model contains the plasma sheath equations to compute the conditions needed for hybrid growth. Surface deposition kinetics and gas-phase processes of the species responsible for catalyst-assisted growth of hybrid are investigated to study the dependence of growth characteristics on the plasma parameters (total gas pressure, plasma power). Defect mediated growth of graphene over nanocone is examined. Henceforth field enhancement factor of the hybrid is probed at different input plasma power to analyse its utility in field emission devices.

2.2 Introduction

In material engineering, Plasma Enhanced Chemical Vapor Deposition (PECVD) is a well-established technique for growing nanostructures in which, the source gas is ionized via electrical energy to produce plasma comprising energetic electrons, positive, negative charged ions, neutrals, and radicals. The strength of the electric field formed within the plasma sheath (area of uncompensated charges) effectively controls the flux of energy and ionized species on the catalyst surface. Plasma control parameters influence sheath dynamics, which in turn affect the electric field strength.

Intensive efforts have been made over the last few decades for designing electron field emitters owing to its promising application in X-ray generators, flat panel display, field emission (FE) guns, etc. [1–6] using nanocarbon allotrope because of its low voltage requirement for the extraction of electrons from its surface. The

unique properties of carbon nanotubes (CNTs) and graphene have allowed these nanocarbon allotropes suitable for use as cold cathode emitters.
The electron field emission (FE) occurs mainly from the tip of CNT while its side remains less sensitive to FE and is less stable towards FE whereas for FE from graphene, the sharp edges of the graphene should be vertical to the substrate. Furthermore, except for the FE stability, the graphene FE properties are low in comparison to CNT. Considering both CNT and graphene, efforts have been made to design an improved and stable field emitter [7–9] which is a hybrid of CNT and graphene (Carbon Micronymphaea**)**, as a 3-D field emitter. This hybrid structure consists of graphene branches from the tip and walls of the CNTs.

Graphene, CNT, CNT-Graphene Hybrid grown using PECVD technique have found a wide range of applications such as in the fabrication of electron field emitters [12, 13], transparent conductors [14], electrodes for the lithium-ion battery [15, 16], supercapacitors [17,18], coating of target material for ion acceleration [19], biomolecule sensors[20]. In space electric propulsion systems, multiwall CNTs are promising techniques to enhance channel wear resistance [21], as field emitter operating without or reduced gas supply installed on a hall effect thruster [4, 6].

Nitrogen doping of these structures lowers the work function, enhances the number of defects, active sites for oxygen reduction reactions, electrical conductivity, specific capacitance, and lowers resistance to charge transfer thus making them efficient electron field emitters, oxygen electrocatalyst for rechargeable Zn-Air batteries, electrochemical sensors, supercapacitors, visible-light-driven photocatalyst for organic dye degradation [22–26].

Studies shows (i) Regulating the growth time, concentration of C, microwave power, growth temperature, length of the composite structure can be effectively controlled, which in turn influence its field emission characteristics [27, 28]. (ii) Growth of graphene sheet occurs from the defects (split C–C bonds) on CNT via high-energy bombardment of ions in plasma and lengthening by epitaxial mechanism [8]. (iii) Growth of vertical graphene (VG) sheet over CNT via defect formation by varying PECVD process parameters, which influence growth of VG sheet through mathematical modeling [29].

Motivated by the above mentioned works, author have tried to model and numerically analyzed the growth of graphene over nanocone surface and linked chemical sputtering/etching mechanism with the growth of N-NCN-VG Hybrid by varying the PECVD process control parameters i.e., total gas pressure, input plasma

power, and growth time. Varying ion number density, etchant number density, carbon surface concentration are the key factors affecting growth of nanocone, defects, and VG Sheet over nanocone surface. In this model, the VG sheet nucleates over the defect generated on the nanocone surface.

2.3 Model

In this section, the growth kinetics of the N-NCN-VG hybrid is modeled via the PECVD route accompanying by key presumptions with equations to detail its growth and nucleation. In the present work chemical sputtering/etching assisted growth of N-NCN-VG Hybrid is modeled wherein, plasma made of electrons, ion plus neutral of C_2H_2, ion plus neutral of H2, ion plus neutral of NH3 has been considered and are elaborated in Table 2.1 which are key reactants in plasma chemistry of the C_2H_2/NH_3 gas combination [30]. Figure 2.1 shows the schematic of N-NCN-VG Hybrid growth on the Nickel (Ni) catalyst over Silicon (Si) substrate. Several stages are involved in the growth: creation of ultra-small metal catalyst nanoparticle as a beginning step; followed by its saturation with carbon species; and ultimately, the nanocone growth covering saturated nanoparticle. The incoming carbon species are responsible for the growth of carbon nanocone, while hydrogen ions and nitrogenous ions which build up the electric field near the nano-hillock surface take part in the role of etching of carbon nanocone [31]. So, there exist both deposition-etching during the growth of carbon nanocone. Initially, saturation of catalyst nanoparticles takes place by the adsorption, diffusion, and sticking of hydrocarbon species. Once, the saturation of catalyst nanoparticle is reached, nucleation of nano-hillock on its top takes place by additional carbon atoms. Here we have assumed that, along with the nucleation of nano-hillock at the center of catalyst nanoparticle, it also grows radially until the catalyst nanoparticle is fully covered [32]. So a nano-hillock of increased height and base radius with a small slope angle is obtained, which leads to weaker chemical sputtering/etching yield, consequently, carbon species deposition takes over during the preliminary growth stage of carbon nanocone [33]. With increasing deposition of carbon species, slope angle of nano-hillock increases, and chemical sputtering/etching becomes more effective and the rate of deposition decreases. When deposition of carbon reaches equilibrium with the etching of carbon so stable nanocone will be formed [33]. The presence of hydrocarbon, hydrogen, and nitrogenous ion in plasma lead to formation of defects on nanocone surface. Under applied bias and electrostatic field, the energetic ions (energy above the threshold energy needed for bond breaking) continuously bombard the nanocone plane to split several C–C bonds (bond energy 17–20 eV) [34], thereby creating cracks and dangling bonds (local defects) that are

well-known nucleation sites for two dimensional VG sheet growth on nanocone surface[27, 35]. Then VG sheet proceeds the way as discussed in previous studies [36–38]. Later these defects capture hydrocarbon species and form carbon monomers after several
processes to attain stability. Carbon monomers then diffuse and aggregate to make graphitic carbon clusters [37, 38]. As time elapses, the as formed carbon clusters diffuse and aggregate to form graphene nuclei promoting the formation of graphene islands which in turn diffuse and align to produce larger islands or flat graphene sheet [37–39]. Alignment of graphene layers takes place normally to nanocone surface under the effect of internal tensile force and inbuilt electric field (induced

Table 2.1 Neutrals and ions considered in model

Neutrals			**Ions**		
Type a	Type b	Type c	Type a	Type b	Type c
C_2H_2, CH_4, CH_3	H, H_2	NH_3,N_2, NH_4, HCN	$C_2H_2^+$, CH_4^+, CH_3^+	H^+, H_2^+	NH_3^+,N_2^+, NH_4^+, HCN^+

between bulk plasma and the negatively biased substrate surface as a result of charge separation region known as plasma sheath) along with regular dissociation and diffusion of hydrocarbon and carbon species, respectively, yielding graphene sheet growth [38]. For the growth of the graphene sheet, a nanocone template of base radius r and height h has been considered in the plasma constituting the ionized gas mixture of C_2H_2/NH_3. It is known that a typical PECVD, is described by the formation of plasma sheath. Within the plasma sheath, the medium shall be regarded as two interpenetrating fluids constituting neutral molecules and ions, respectively [40] where the microscopic plasma sheath electrostatic force (from space charge separation) accelerates the ions heading to the surface [41]. Considering the induced sheath electrostatic field to be along the z-axis i.e., in the vertically downward direction. Presently in the plasma sheath model the ion velocities, ion energies, the number density of ions, and neutral species in the plasma is found by coupling the equation of continuity and momentum balance equation to the Poisson's equation which relates potential distribution in the plasma sheath and number densities of charged species [42, 43].

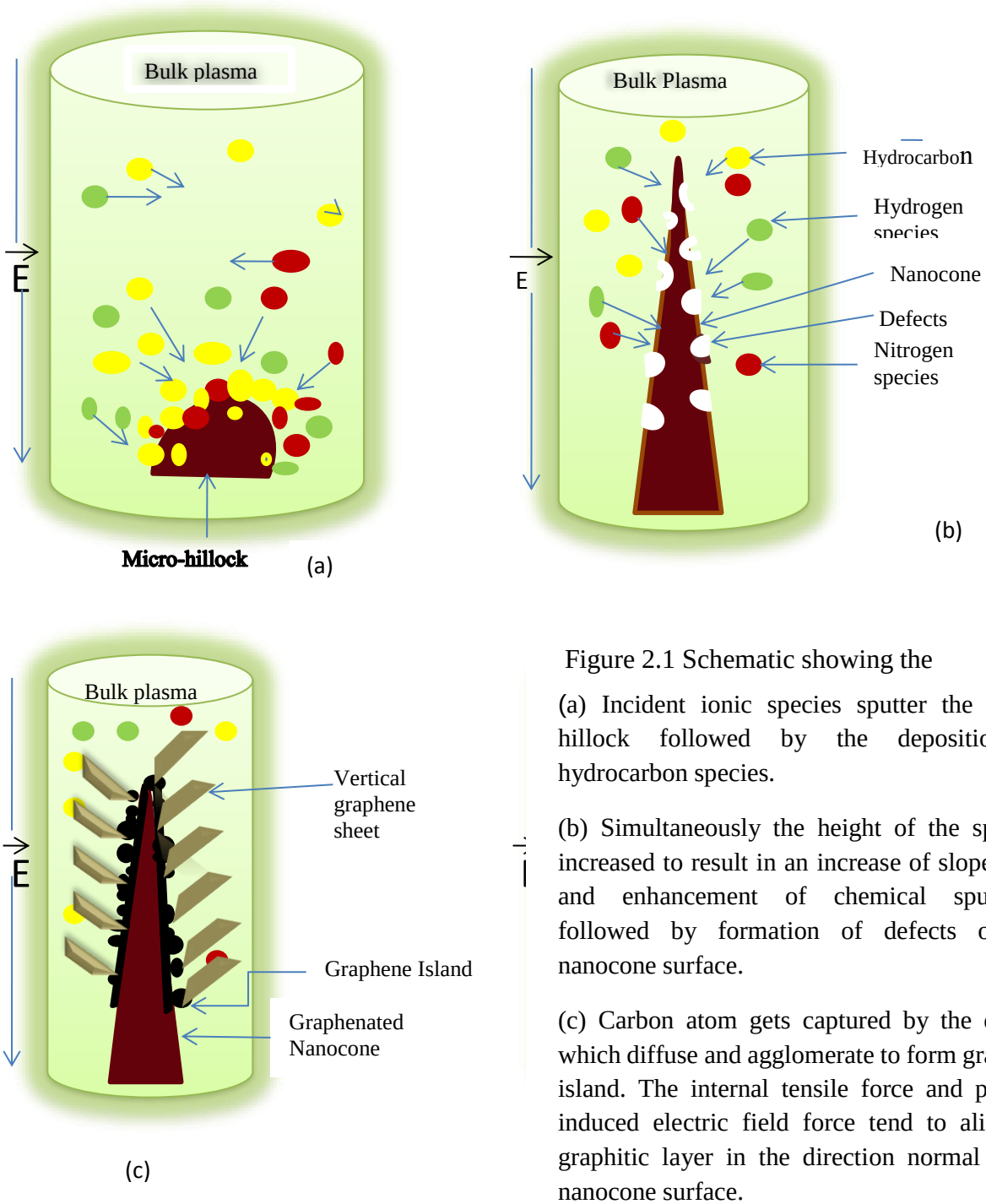

Figure 2.1 Schematic showing the

(a) Incident ionic species sputter the micro-hillock followed by the deposition of hydrocarbon species.

(b) Simultaneously the height of the spike is increased to result in an increase of slope angle and enhancement of chemical sputtering followed by formation of defects on the nanocone surface.

(c) Carbon atom gets captured by the defects which diffuse and agglomerate to form graphene island. The internal tensile force and plasma-induced electric field force tend to align the graphitic layer in the direction normal to the nanocone surface.

$$\frac{\partial\left(n_{ik}\vartheta_{ik}\right)}{\partial z}=\upsilon n_{ik} \tag{1}$$

$$\frac{\partial\left(n_{e}\vartheta_{e}\right)}{\partial z}=\upsilon n_{e} \tag{2}$$

$$n_{ik}\vartheta_{ik}\frac{\partial\vartheta_{ik}}{\partial z}=\frac{-en_{ik}}{M_{ik}}\frac{d\zeta}{dz}-n_{ik}\eta_{ik}\vartheta_{ik}-\frac{T_{ik}}{M_{ik}}\frac{dn_{ik}}{dz} \tag{3}$$

$$en_{e}\frac{d\zeta}{dz}=T_{e}\frac{dn_{e}}{dz}+M_{e}n_{e}\eta_{e}\vartheta_{e} \tag{4}$$

$$\frac{d^{2}\zeta}{dz^{2}}=-4\pi e\left(n_{e}-\sum_{k}\gamma_{ik}n_{ik}\right) \tag{5}$$

where M_{ik}; n_{ik}; T_{ik}; and ϑ_{ik} are the masses, number densities, temperature, and fluid velocities of the positively charged species, respectively [k corresponds to the a,b,c type of positively charged ions (see Table 1). M_e; n_e; T_e; *and* ϑ_e are the mass, number densities, temperature, and velocities of electrons, respectively.

Eqs. (1) and (2) are the continuity equations and Eqs. (3) and (4) are momentum balance equations for ions and electrons, respectively, and take into account ionization of neutrals by electrons with ionization frequency $\upsilon=\mu_{ik}\gamma_{ik}N$ where μ_{ik} is the ionization potential, $\gamma_{ik}=\frac{n_{ik}}{n_e}$ or $\frac{p_k}{p}$,where $p=NT_i$ and p_k are the total gas pressure of k^{th} gas and $N=\sum_k\gamma_k n_k$ is the total neutral species number density, n_k is the number density of k^{th} neutral. $\eta_\beta=\sigma_\beta NU_\beta$ is the collision frequency accounting the collision of ions and electrons with the neutrals , β refer to electrons and k ions, σ_β is the cross-section of the collision, U_β is the mean speed of the charged species β, ionization rate $\left(\upsilon\alpha n_k\exp\left(\frac{-E_{ik}}{T_e}\right)\right)$ with E_{ik} as first ionization potential energy of the k^{th} neutral. The plasma sheath Eqs. (1) - (4) along with Poisson's Eq. (5) are solved by applying boundary conditions as follows

$$\zeta=0,\frac{d\zeta}{dz}=-\frac{T_e}{e\lambda},\vartheta_e=0,\vartheta_{ik}=\vartheta_{iko},\vartheta_{iko}=\sqrt{\frac{T_e}{M_{ik}}}\quad \textit{where}\ \lambda=\frac{T_n}{\sigma_\beta p}$$ is the ion mean free path.

Presumptions considered for simplified modelling [44–46]

(a) Maxwellian distribution of electrons and ions is considered.

(b) Ion – surface interaction is assumed coulomb interaction.
(c) For the sheath to perform its function and repel electrons, the potential must be monotonically decreasing with increase in z. This will occur if $n_i(z) > n_e(z)$ for all z in the sheath.
(d) Plasma-surface interaction heats the nanocone surface, thus gaining the constant temperature Ts and is assumed uniform along nanocone.
(e) The collisions of the neutrals, ions with nanocone surface are assumed elastic.

2.3.1 Chemical Sputtering/Etching

2.3.1.1 Low Ion Energy Sputtering

The incoming hydrogen, nitrogenous, hydrocarbon ions project and transfer their momentum to the atoms on the growing N-NCN –VG hybrid. It takes place above the threshold energy of incident ions. As a result, physically sputtered carbon atoms originate predominantly from the growing hybrid, thereby removing amorphous carbon. The threshold is specified as minimum incident energy needed to split a C–C bond which for physical sputtering of amorphous carbon by $NH3^+$ and H^+ ions has been calculated to about 31.08 eV, and 22.44 eV for carbon surface binding energy of E_B(≈ 4.5 eV) [47].

For the sputtering of low energy ions, the threshold energy is given as [47, 48].

$$E_{thr} = \begin{Bmatrix} \dfrac{E_B}{\Upsilon(1-\Upsilon)}, (M_{ik} \le M_c) \\ \dfrac{6.7E_B}{\Upsilon}, (M_{ik} > M_c) \\ \Upsilon = \dfrac{4M_{ik}M_c}{(M_{ik}+M_c)^2} \end{Bmatrix}$$

where M_{ik} and M_c are the incident ion mass which can be hydrogen, nitrogenous, hydrocarbon ion and mass of target, respectively.

2.3.1.2 Ion Assisted Etching

Incident hydrogen, nitrogenous ions generate split bonds in the cascaded collision which are immediately stabilized by the rich atomic hydrogen and nitrogen flux. Repeated bond (sp3-C) splitting events along with stabilization by H and N generate

stable C–H and C–N bonds on the surface, which then get thermally desorbs from the surface, thereby removing amorphous carbon via the formation of volatile hydrocarbons, HCN, CN, C_2N_2 [49, 50]. Below are the reactions (A) & (B) showing ion-assisted etching, where the ion (I^+) can be hydrogen, nitrogenous.

$$C_{(ads)}\,H_{(plasma)} \xrightarrow{K_I I^+} CH_{(plasma)} \quad (A)$$

$$C_{(ads)}\,N_{(plasma)} \xrightarrow{K_I I^+} CN_{(plasma)} \quad (B)$$

where K_I is the rate coefficient for ions incident over surface.
Carbon species flux (Γ_C) leaving the surface is expressed by equation (C)

$$\Gamma_C = Y_I K_I n_{ik} \upsilon_o \theta_C + \frac{J_a \sigma_{ads} J_b}{\omega} + S_C \sigma_{ads} J_b + K_d \upsilon_o \theta_{CH} \quad (C)$$

where the first, second, third term on the right side of equation (C) denotes the flux of carbon atom and carbon-bearing species leaving the N-NCN-VG Hybrid surface due to ion assisted sputtering and fourth terms flux of carbon-bearing species leaving the N-NCN-VG Hybrid surface due to thermal desorption of CH species. $\boldsymbol{Y_I}$ is the chemical sputtering/etching yield based on ion energy as $\boldsymbol{Y_I \propto \sqrt{E_i} - \sqrt{E_{thr}}}$ [51], where $\boldsymbol{E_i}$ *i*s the ion energy in eV and $\boldsymbol{E_{thr}}$ is the threshold energy in eV. $K_I = \sqrt{\frac{eT_e}{M_i}} \Big/ \upsilon_O$ denotes the rate coefficient for ions incident on the surface. $\boldsymbol{\theta_C, \theta_{CH}}$ is the fraction of surface sites covered with C atom, CH species. $\boldsymbol{K_d = K_0 exp\left(\frac{-E_{dh}}{K_B T_S}\right)}$ is the desorption rate constant. $\boldsymbol{K_0}$ is the number of attempted escapes per second from the adsorption well, hence $\mathbf{K_0} = \frac{\omega}{\boldsymbol{2\pi}} . E_{dh}\left(\approx 1.8eV\right)$ is the hydrocarbon desorption energy. $Y_I = \frac{1}{\pi^2}\left(\frac{M_c M_{ik}}{\left(M_c + M_{ik}\right)^2}\right)\frac{E_i}{E_B}\left(\cos\theta\right)^{-f}$ f is constant for certain $\boldsymbol{M_c/M_i}$ in this ion energy range [52s]. $\ominus$ is angle of incidence of ions on growing N-NCN-VG hybrid, k_B is the Boltzmann constant.

2.3.2 Growth of Nitrogen‑Doped Nanocone

The growth of nitrogen-doped nanocone, shown in terms of volumetric change (base radius r, tip radius r1 and height h) with time, with the number density of carbon and hydrogen developed over the catalyst nanoparticle.
Due to plasma-induced stress and/or localized electrostatic field, the nanocone growth takes place in the vertical direction. Nanocone growth process traced in Eq. (6) includes surface diffusion and incorporation of carbon monomer, along with surface diffusion of carbon cluster with the various energy barriers. The fourth term is the etching term which decreases the growth rate of nanocone. The final two terms add up to the sticking of neutrals of type 1 and 3, respectively over nanocone surface [53, 54].

$$\frac{1}{3}\pi\frac{d\left(\frac{r^3-r_1^3}{r-r_1}\right)h}{dt}=\left[\left(\frac{D_1}{\omega}\exp\left(\frac{-E_{SDc}}{k_BT_s}\right)+\frac{D_2}{\omega}\exp\left(\frac{-E_{SDcl}}{k_BT_s}\right)\right)\times S_C\times j_{ia}\times V\right]- \left[\left(+A_k\exp\left(\frac{-\delta E_{INc}}{k_BT_s}\right)\omega r\right)\right] \left[\pi rh\times S_H\times j_{ib}\times V\right]+\left[\left(\chi_a j_a+\chi_c j_c\right)\times V\right] \quad (6)$$

where $V = M_{nacn}/\rho_{nacn}$, $M_{nacn}(\approx 12g)$, and ρ_{hacn} are the mass and density of the nanocone, D_1 and D_2 are surface diffusion coefficients, A_k is the carbon monomer incorporation speed into nanocone, $E_{INc} \approx (0.4$ eV) is the energy barrier for carbon monomer to diffuse along the nanocone-catalyst interface, respectively. Activation energy for surface diffusion of carbon monomer and of carbon clusters are $E_{SDc} \approx$ 0.3 eV, $E_{SDcl} \approx 0.48$ eV along the nanocone- catalyst interface. ($\chi_a = \chi_c$) ≈ 1 are the sticking coefficient of neutral atom of type a and c [39, 54, 55]. *jia, jib* are the ion collection current of type a and b over nanocone surface,j_a, j_c are the neutral collection current of type a and c over nanocone surface.

2.3.3 Defects Formation on Nanocone Surface

Time variation of energy balance at the nanocone surface in C_2H_2/NH_3 plasma is described by Eq. (7). The R.H.S of Eq. (7) describes the power transferred to the nanocone surface, due to incidence of plasma species i.e., positive charged ions, neutrals, and electrons (first term), due to neutrals generation at nanocone surface

(second term), due to hydrogen assisted etching of nanocone surface (third term), due to sputtering by incident ions (fourth term) give rise to defect on nanocone surface, due to surface diffusion along with the incorporation of created carbon species over nanocone surface (fifth term). Time variation of linear defect density on nanocone surface is shown by L.H.S. of Eq. (7)

$$P = M_{nacn} C_c T_s \frac{1}{Nd}\frac{\partial Nd}{\partial t} = \left[\sum_{k}^{a,b,c}\left[\left[\left(j_{ik}^{c_{cur}} + j_{ik}^{c_{tip}}\right)\in_{ij}^{c}\right] + \left[\left(j_{k}^{c_{cur}} + j_{k}^{c_{tip}}\right)\in_{k}^{c}\right]\right] + \left(j_{e}^{c_{cur}} + j_{e}^{c_{tip}}\right)\in_{e}^{c}\right] +$$
$$\left[\frac{3}{2}k_B T_s \sum_{k}^{a,b,c}\left(1-\chi_{ik}\right)\left(j_{ik}^{c_{cur}} + j_{ik}^{c_{tip}}\right)\right] + \left[\left(\upsilon_o \sigma_{ads} J_b E_B\right) A_c\right] +$$
$$\left[\left(\sum_{k}^{a,b,c} J_{ik} Y_s\left(E_i\right)\left(1-\theta_t\right) A_c\right)\right] + \left[S_C \omega \exp\left(\frac{-E_{SDc}}{k_B T}\right) A_c E_{INc}\right] \qquad (7)$$

where $M_{nacn}, C_c,$ and $A_c(= \pi r^2 + \pi r h)$ are the mass, specific heat, and area of nanocone. Nd is the linear (micron length) defect density produced on nanocone. $J_k = \left(\frac{n_k u_{thk}}{4}\right)$ and $J_{ik} = \left(n_{ik}\left(\frac{k_B T_e}{M_{ik}}\right)^{0.5}\right)$ denoting impinging flux composing neutrals and positive charged ions of type k, respectively [56]. $\in_{ik}^{c} = \left[\left(\left(\frac{2 - Z\Psi\beta}{1 - Z\Psi\beta}\right) - Z\Psi\beta\right) k_B T\beta\right]$ denotes the average energy accumulated over nanocone surface owing to β species, β signifies electrons, neutrals, and ions of type k, where $\Psi_\beta = \left(\frac{E_B}{k_B T_\beta}\right)$ and E_B is the energy barrier at the nanocone surface[45].

$j_{ik}^{c_{tip}} = \left[\pi r_1^2 \left(\frac{8 k_B T_{ik}}{\pi M_{ik}}\right)^{0.5} n_{ik}(x)\left(1 - Z\chi_V\right)\exp\left(\frac{-eU_V}{k_B T_s}\right)\right]$ denotes ion collection current due to positively charged species at the nanocone tip.

$j_{ik}^{c_{cur}} = \left[n_{ik}(x) r_1 h \left(\frac{2\pi k_B T_{ik}}{M_{ik}} \right)^{0.5} \left(2 \left(\frac{eV_V}{\pi k_B T_{ik}} \right)^{0.5} + \exp\left(\frac{eV_V}{k_B T_{ik}} \right) erfc \left(\frac{eV_V}{k_B T_{ik}} \right)^{0.5} \right) \exp\left(\frac{-eU_V}{k_B T_s} \right) \right]$ is the ion collection current over curved surface of nanocone due to positively charged species. The charge number over the nanocone surface is denoted by *Z*. $n_{ik}(x) = n_{iko} \left(1 - \frac{2e\varphi(x)}{M_{ik} \vartheta_{iko}} \right)$ is the positive ion density in plasma sheath as a function of structure coordinate. u_{thk} is thermal velocity of type k neutral, respectively. ϑ_{iko} is velocity of positive ion, $\varphi(x) = \varphi_o \exp\left(\frac{-|x|}{\lambda_d} \right)$ denoting static potential inside the plasma sheath, φ_o is the negative potential at the substrate surface. λ_d denotes debye length. $\chi_V = eV_{ctip}(z), V_{ctip}(z) = \left(\frac{e}{4\pi\varepsilon_o r_1} \right)$ is the potential at the tip of nanocone**.** $M_{ik}, T_{ik,} V_V$ are the mass, temperature of positive ion of type k, potential at curved surface of nanocone[57]**.**

$$V_V = \sigma \frac{\left(3\sqrt{h^2 - 2hz + 2z^2} + (-2h + 4z) \log\left[\frac{-2h + 4z + 2\sqrt{2}\sqrt{h^2 - 2hz + 2z^2}}{\sqrt{2}} \right] \right)}{4\sqrt{2}\varepsilon_o}$$

$j_e^{c_{tip}} = \left[n_e(x) \pi r_1^2 \sqrt{\left(\frac{8k_B T_e}{\pi m_e} \right)} \exp\left[\frac{Z\chi_V}{k_B T_e} + \frac{eU_V}{k_B T_s} \right] \right]$ **and**

$j_e^{c_{cur}} = \left[n_e(x) r_1 h \sqrt{\left(\frac{2\pi k_B T_e}{m_e} \right)} \exp\left[\frac{eV_V}{k_B T_e} + \frac{eU_V}{k_B T_s} \right] \right]$ denotes the collection current due to electrons over the tip and lateral surface of the nanocone. We will herein call these collections as OML collections. For OML theory to apply $r << \lambda_d$, where r is the base radius of nanocone and λ_d is the Debye length [58–60]

$n_e(x) = n_{eo} \exp\left(\frac{|e|\varphi(x)}{k_B T_e} \right)$ is the electron density inside the plasma sheath in response to structure coordinate. $j_k^{c_{tip}} = n_k(x) r_1^2 \left(\frac{8\pi k_B T_k}{M_k} \right)^{0.5}$ and $j_k^{c_{cur}} = n_k(x) \pi r_1 h \left(\frac{2\pi k_B T_k}{M_k} \right)^{0.5}$ are the neutral collection current over tip and lateral surface of nanocone.

Shruti Sharma
Delhi Technological University

$\upsilon_o \approx \left(10^{15} cm^{-2}\right), \sigma_{ads} \approx \left(10^{-16} cm^2\right)$ is the area density of adsorption sites, reaction cross-section with atomic hydrogen[41]. $Y_s(E_i)$ is the sputtering yield function of ion energy[61]. θ_t is the total surface coverage. Using mass conservation, area of the resulting defect is estimated to be $Rd^2 = \left(\frac{r_1^2 + r_1 h}{hNd}\right)$, where *Rd* is the defect radius.

2.3.4 Rate of Growth of Hydrogen Radical and Carbon Species over Nanocone Surface

Interaction between neutrals and ions of type a, b, c with nanocone surface serves formation of hydrogen radical and carbon species over nanocone surface through surface process that are described by Eqs. (8) and (9)

$$\dot{S_H} = \sum_b J_b\left(1-\theta_t\right) + \sum_a n_{sa}\omega \exp\left(\frac{-\delta E_{td}}{k_B T_s}\right) + \sum_{ia}\left(\sum_a \frac{n_{sa} Y_d}{\upsilon_o}\right) J_{ia} + \sum_{ia} J_{ia} - \sum_b n_{sb}\omega \exp\left(\frac{-\delta E_{ah}}{k_B T_s}\right)$$
$$- \sum_b n_{sb}\sigma_{ads} J_b - \sum_{ib}\left(\sum_b n_{sb}\sigma_{ads}\right) J_{ib} + \sum_{ic}\left(\sum_c \frac{n_{sc} Y_d}{\upsilon_o}\right) J_{ic} - \sum_{ic} J_{ic} \qquad (8)$$

$$\dot{S_C} = \sum_a J_a\left(1-\theta_t\right) + \sum_a n_{sa}\omega \exp\left(\frac{-\delta E_{td}}{k_B T_s}\right) + \sum_{ia}\left(\sum_a \frac{n_{sa} Y_d}{\upsilon_o}\right) J_{ia} + \sum_{ia} J_{ia} + \sum_{ib}\left(\sum_{ia} \frac{J_{ia}\sigma_{ads}}{\omega}\right) J_{ib}$$
$$- S_C \omega \exp\left(\frac{-Eevp}{k_B T_S}\right) - \Gamma_C \qquad (9)$$

where $\dot{S_H}$ *and* $\dot{S_C}$ are the instantaneous surface concentrations of hydrogen radical and carbon species generated on the nanocone surface, $\delta E_{td}\left(=2.1eV\right)$ hydrocarbons thermal dissociation energy, $\delta E_{ah}\left(=1.8eV\right)$ hydrogen species adsorption energy, $E_{evp}\left(=1.8eV\right)$ carbon evaporation energy, $n_{sk}\left(=\theta_k \upsilon_o\right)$ is surface concentration of

neutral species of type k. θ_k is the surface coverage by species of type k, $\omega\left(\approx 10^{13}\,Hz\right)$ is thermal vibration frequency, $Y_d\left(\approx 2.49\times10^{-2}+3.29\times10^{-2}\times E_i\right)$ is stitching probability[43,61] respectively. The surface processes are explained in Table 2.

2.3.5 Growth of Graphene Island

When energetic ions strike the surface of nanocone, defects are produced on the nanocone surface. This ion irradiation produced defects on nanocone surface are energetically unstable. Later these defects capture hydrocarbon species and form carbon monomers after several processes to attain stability. Carbon monomers afterward diffuse and accumulate to make carbon clusters. As time elapses the as formed carbon clusters along with diffusion, accumulate to make graphene nuclei which upon further diffusion and accumulation form graphene island that in turn diffuse and stitch together to produce larger islands [37, 39].

The below-shown Eq. (1) traces graphene island (radius r_{gIs}) growth relating to rate of change of area (nm^2/s) of graphene island

$$\frac{d\left(\pi {r_{gIs}}^2\right)}{dt}=\left[\begin{array}{l} S_C\left[D_1\exp\left(\frac{-\left(E_{SDc}+E_{INc}\right)}{k_BT_s}\right)+D_2\exp\left(-\frac{-\left(E_{SDcl}+E_{INcl}\right)}{k_BT_s}\right)+D_3\exp\left(-\frac{-\left(E_{SDis}\right)}{k_BT_s}\right)\right] \\ \times\left[\left(\frac{Ad}{2\pi r_{gIs}}\right)\times\left(\frac{2\pi Rd\times j_{ia}^{g}}{\omega}\right)\right]+\left(\begin{array}{l}\chi_a\pi r_{gIs}^2\times j_a^g+\\ \chi_c\pi r_{gIs}^2\times j_c^g\end{array}\right) \end{array}\right] \tag{10}$$

where D_1, D_2, D_3 are the surface diffusion coefficients, j_{ia}^{g} , j_a^g and $\mathrm{j_c^g}$ symbolize ion, neutral collection current of type a and neutral collection current of type c at the growing graphene island respectively. $E_{SDc}\approx 0.1\mathrm{eV}, E_{SDcl}\approx 0.82\mathrm{eV}, E_{INc}\approx 0.42\mathrm{eV}, E_{INcl}\approx 0.42\mathrm{eV}, E_{SDis}\approx 2.6\mathrm{eV}$ are the energies of activation for surface diffusion of carbon monomers and carbon clusters, activation energy barriers for incorporation of carbon monomer and carbon clusters, and activation energy barriers for surface diffusion of graphene island[1,3]. $(Ad=\pi Rd^2)$ is the area of defect at nanocone surface. In the equation, the first term accounts for surface diffusion and

incorporation of carbon monomers into the defective sites at nanocone surface. Second term accounts for surface diffusion and incorporation of carbon clusters. The third term accounts for surface diffusion of graphene islands, followed by the fourth term, for accumulation of neutral atoms of type a and c on the graphene island.

Table 2.2 Explanation of surface process expressions used in Eq. (8) and (9)

Expressions	Explanation and reaction involved
$\sum_b J_b\left(1-\theta_t\right)$	Hydrogen Adsorption on nanocone surface $H_{(plasma)} \rightarrow H_{(ads)}$ $H_{2(plasma)} \rightarrow H_{2(ads)}$
$\sum_a n_{sa}\omega\exp\left(\frac{-\delta E_{td}}{k_B T_s}\right)$	Thermal dissociation of adsorbed hydrocarbons $C_2H_{2(ads)} \rightarrow 2C_{(ads)} + 2H_{(ads)}$ $CH_{(ads)} \rightarrow C_{(ads)} + H_{(ads)}$
$\sum_{ia}\left(\sum_a \frac{n_{sa}Y_d}{\upsilon_o}\right)J_{ia}$	Ion-induced dissociation of adsorbed hydrocarbons $C_2H_2^+ + C_2H_{2(ads)} \rightarrow 2C_{(ads)} + H_{2(plasma)} + C_2H_2^+$ $CH^+ + CH_{(ads)} \rightarrow C_{(ads)} + H_{(ads)} + CH^+$ $C_2H_2^+ + CH_{(ads)} \rightarrow C_{(ads)} + H_{(ads)} + C_2H_2^+$ $CH^+ + C_2H_{2(ads)} \rightarrow 2C_{(ads)} + H_{2(plasma)} + CH^+$
$\sum_{ia} J_{ia}$	Hydrocarbons ion decomposition $C_2H_2^+ \rightarrow 2C_{(ads)} + H_{2(plasma)}$ $CH^+ \rightarrow C_{(ads)} + H_{(ads)}$
$\sum_b n_{sb}\omega\exp\left(\frac{-\delta E_{ah}}{k_B T_s}\right)$	Hydrogen desorption $H_{(ads)} \rightarrow H_{(des)}$
$\sum_b n_{sb}\sigma_{ads}J_b$	Adsorbed hydrogen species loss due to interaction with incoming hydrogen atoms from plasma.
$\sum_{ib}\left(\sum_b n_{sb}\sigma_{ads}\right)J_{ib}$	Adsorbed hydrogen species loss due to interaction with incoming hydrogen ions from plasma.
$\sum_{ic}\left(\sum_c \frac{n_{sc}Y_d}{\upsilon_o}\right)J_{ic}$	Ion induced dissociation of adsorbed ammonia $NH_3^+ + NH_{(ads)} \rightarrow N_{(ads)} + H_{(ads)} + NH_3^+$ $NH_2^+ + NH_{2(ads)} \rightarrow N_{(ads)} + 2H_{(ads)} + NH_2^+$
$\sum_{ic} J_{ic}$	Loss of hydrogen due to Ammonia ion decomposition $NH_2^+ \rightarrow N_{(ads)} + H_{2(plasma)}$ $NH_4^+ \rightarrow N_{(ads)} + 2H_{2(plasma)}$
$\sum_a J_a(1-\theta_t)$	Adsorption of hydrocarbon on nanocone surface $C_2H_{2(plasma)} \rightarrow C_2H_{2(ads)}$ $CH_{(plasma)} \rightarrow CH_{(ads)}$
$S_c\omega\exp\left(\frac{-Eevp}{k_B T_S}\right)$	Evaporation of Carbon $C_{(ads)} \rightarrow C_{(ev)}$
$\sum_{ib}\left(\sum_{ia}\frac{J_{ia}\sigma_{ads}}{\omega}\right)J_{ib}$	Carbon generation on N-NCN under hydrocarbon and hydrogen ions interaction $CH^+_{(plasma)} + H^+_{(plasma)} \rightarrow C_{(ads)} + H_{2(plasma)}$

2.3.6 Growth of Nitrogen doped Vertical Graphene (N-VG) Sheet over nanocone

The as-formed defects act as nucleation sites for N-VG sheets. At initial, flat graphene grow around the defects which afterward switches to upward growth on nanocone under local electric field and tensile stress (arise due to difference in the structure and expansion coefficient of N-VG sheet and amorphous nanocone [37]). The growth rate Eqs. (11) and (12) of N-VG sheet is expressed below.

$$l_{gr}\ \frac{d\left(h_{gr}\times t_{gr}\right)}{dt} = \left[\begin{bmatrix} S_C\omega\exp\left(\frac{-E_{SDc}}{k_BT_S}\right)\times\pi r_{gIs}^2 \end{bmatrix}+ \begin{bmatrix} \frac{S_C}{\omega}A_k\exp\left(\frac{-E_{INc}}{k_BT_S}\right)\times 2\pi r_{gIs}\times j_{ia}^{gr} \end{bmatrix}+ \begin{bmatrix} \chi_a j_a^{gr}+\chi_c j_c^{gr} \end{bmatrix}\right]\times\frac{M_{gr}}{\rho_{gr}} \qquad (11)$$

$$\left[h_{gr}(t)+l_{gr}\right]\frac{dt_{gr}}{dt} = \left[\begin{bmatrix} S_H\times h_{gr}(t)\times j_{ib}^{gr}\times\frac{1}{n_{ib}} \end{bmatrix}+ \begin{bmatrix} \chi_a\pi r_{gIs}^2 j_a^{gr}+\chi_c\pi r_{gIs}^2 j_c^{gr} \end{bmatrix}\right] \qquad (12)$$

where l_{gr}, h_{gr}, t_{gr} are the length, height, thickness of the N-VG sheet.$\left(M_{gr}\approx 12g\right)$, ρ_{gr} are the mass, density of the N-VG sheet. j_{ia}^{gr}, j_a^{gr}, j_c^{gr} are the ion collection current of type a, neutral collection current of type a, type c over N-VG sheet surface. The first and second term on RHS of Eq.(2) shows the surface diffusion and incorporation of carbon atoms at the surface and peripherals of growing N-VG sheet attributing to growth of N-VG sheet. Also, the ion collection current at the surface of the growing sheet adds to the growth of the N-VG sheet. The last two terms represents the sticking of the neutral atom of type a and c at the N-VG sheet. Finally decrease in thickness of the growing N-VG sheet is accounted in Eq. (3) where the first term represents the etching of terminal carbon present at the edges of the N-VG sheet due to interaction with hydrogen atoms from the plasma. The sticking coming from neutrals of type a and c is denoted by the final two terms respectively, over the surface of the growing N-VG sheet.

2.3.7 Charging of N-NCN-VG Hybrid:

Charging of N-NCN-VG Hybrid takes place due to accretion of positive ions and electrons on N-NCN-VG Hybrid surface.

$$Z^{\bullet} = \sum_{k}^{a,b,c} j_{ik}^{c_{tip}} + \sum_{k}^{a,b,c} j_{ik}^{c_{cur}} + \sum_{k}^{a,b,c} j_{ik}^{gr} - \gamma_e \left(j_e^{c_{tip}} + j_e^{c_{cur}} + j_e^{gr} \right) \tag{13}$$

Z is the charge number over N-NCN-VG Hybrid

.

$$j_{ik}^{gr} = n_{ik}(x)\left(l_{gr}t_{gr} + t_{gr}h_{gr} + h_{gr}l_{gr}\right)\left(\frac{k_B T_{ik}}{2\pi^2 m_{ik}}\right)^{0.5} \times \left(\begin{array}{l} \frac{2}{\sqrt{\pi}}\left(\frac{eV_V}{k_B T_{ik}}\right) \\ +\exp\left(\frac{eV_V}{k_B T_{ik}}\right) erfc\left(\frac{eV_V}{k_B T_{ik}}\right) \end{array}\right) \times \exp\left(\frac{-eU_V}{k_B T_s}\right)$$

$j_e^{gr} = n_e(x)\left(l_{gr}t_{gr} + t_{gr}h_{gr} + h_{gr}l_{gr}\right)\left(\frac{k_B T_e}{2\pi^2 m_e}\right)^{0.5}\left(\exp\left(\frac{eV_V}{k_B T_e} + \frac{eU_V}{k_B T_s}\right)\right)$ denotes the ion and electron collection current at the VG surface**.** $\gamma_e(=1)$ is sticking coefficient of electron. In Eq.(10), the first, second, and third term on the right-hand side describes the charge developed on nanocone tip, nanocone curved surface, and VG surface owing to positive charged ions accretion of type a, b and c. The last term indicating the reduction in charge due to electron accretion at the nanotip, nanocone curved surface, and VG sheet.

2.3.8 Number density equalization of electrons in plasma

Equation (14) represents number density equalization of electrons in plasma

$$n_e^{\bullet} = \sum_{k}^{a,b,c} \delta_k n_k - \sum_{k}^{a,b,c} \alpha_k n_e n_{ik} - \chi_e n_{hyb} \left(j_e^{c_{tip}} + j_e^{c_{cur}} + j_e^{gr} \right) \tag{14}$$

where δ_k *and* $\alpha_k \left(= \alpha_{ko} \left(\frac{300}{T_e} \right)^k \right) cm^3 \sec^{-1}$ are the ionization coefficient of constituting neutral atoms through external means and coefficient of recombination of electron

and positively charged ions with $k = -1.2$ being a constant. n_e and T_e are the electron number density in plasma and electron temperature, respectively.
The first-term on RHS of Eq. (11) embodies per unit time gain in electron density through neutral atom (type a, b, c) ionization. Second, along with the third term represents electron -ion recombinational loss in electron density per unit time along with loss because of electron collection current over N-NCN-VG Hybrid surface.

2.3.9 Number Density Equalization of Plasma Species

Equation (12a)-(12c) represents the number density equalization of positively charged ions, in plasma

$$\dot{n}_{ia} = \delta_a n_a - \alpha_a n_e n_{ia} - n_{hyb}\left(j_{ia}^{c\,tip} + j_{ia}^{c\,cur} + j_{ia}^{gr} \right) - J_{adia} + J_{desia} + \frac{P}{E_{disa} V} + \sum_i k_{ia} n_a n_{ic} \tag{15a}$$

$$\dot{n}_{ib} = \delta_b n_b - \alpha_b n_e n_{ib} - n_{hyb}\left(j_{ib}^{c\,tip} + j_{ib}^{c\,cur} + j_{ib}^{c\,gr} \right) - J_{adib} + J_{desib} + J_{th} + \frac{P}{E_{disb} V} + \sum_i k_{ib} n_b n_{ic} \tag{15b}$$

$$\dot{n}_{ic} = \delta_c n_c - \alpha_c n_e n_{ic} - n_{hyb}\left(j_{ic}^{c\,tip} + j_{ic}^{c\,cur} + j_{ic}^{c\,gr} \right) - J_{adic} + J_{desic} + \frac{P}{E_{disc} V} + \sum_i k_{ia} n_a n_{ic} + \sum_i k_{ib} n_b n_{ic} \tag{15c}$$

$$\dot{n}_a = \alpha_a n_e n_{ia} - \delta_a n_a + n_{hyb}(1 - \chi_{ia})\left(j_{ia}^{c\,tip} + j_{ia}^{c\,cur} + j_{ia}^{gr} \right) - n_{hyb}(\chi_a)\left(j_{ia}^{c\,tip} + j_{ia}^{c\,cur} + j_{ia}^{gr} \right) - \sum_i k_{ia} n_a n_{ic} \tag{16a}$$

$$n_b^{\bullet} = \alpha_b n_e n_{ib} - \delta_b n_b + n_{hyb}\left(1-\chi_{ib}\right)\left(j_{ib}^{c\,tip} + j_{ib}^{c\,cur} + j_{ib}^{gr} \right) - n_{hyb}\left(\chi_b\right)\left(j_{ib}^{c\,tip} + j_{ib}^{c\,cur} + j_{ib}^{gr} \right) - \sum_i k_{ib} n_b n_{ic} \qquad (16b)$$

$$n_c^{\bullet} = \alpha_c n_e n_{ic} - \delta_c n_c + n_{hyb}\left(1-\chi_{ic}\right) - n_{hyb}\left(\chi_c\right)\left(j_{ic}^{c\,tip} + j_{ic}^{c\,cur} + j_{ic}^{gr} \right) - \sum_i k_{ib} n_b n_{ic} - \sum_i k_{ia} n_a n_{ic} \qquad (16c)$$

$$n_b^{\bullet} = \alpha_b n_e n_{ib} - \delta_b n_b + n_{hyb}\left(1-\chi_{ib}\right)\left(j_{ib}^{c\,tip} + j_{ib}^{c\,cur} + j_{ib}^{gr} \right) - n_{hyb}\left(\chi_b\right)\left(j_{ib}^{c\,tip} + j_{ib}^{c\,cur} + j_{ib}^{gr} \right) - \sum_i k_{ib} n_b n_{ic} \qquad (16b)$$

$$n_c^{\bullet} = \alpha_c n_e n_{ic} - \delta_c n_c + n_{hyb}\left(1-\chi_{ic}\right) - n_{hyb}\left(\chi_c\right)\left(j_{ic}^{c\,tip} + j_{ic}^{c\,cur} + j_{ic}^{gr} \right) - \sum_i k_{ib} n_b n_{ic} - \sum_i k_{ia} n_a n_{ic} \qquad (16c)$$

where $J_{adik} = \frac{P_k}{\left(2\pi M_{ik} k_B T_{ik}\right)^{0.5}} \times \frac{n_{ik}}{J_{ik}}$ is the adsorption flux on the N-NCN-VG surface. P_k denotes adsorbing species partial pressure. $J_{desik} = J_{ik}\omega \exp\left(-\frac{E_{ads}}{k_B T_{ik}}\right)$ is the desorption flux(type k) from the N-NCN-VG surface. E_{ads} denotes adsorption energy. J_{th} denotes type b ions flux due to thermal dehydrogenation[56]. E_{disk} is the dissociation energy of neutrals of type k , $k_{ia} = 1.4\times10^{-9}\ cm^3/s$, $k_{ib} = 7.8\times10^{-9}\exp\left(-14.8/T_n\right)/T_n^{0.39}\ cm^3/s$ are the ion –neural reaction rate coefficient [62,63]. n_{hyb} is the N-NCN-VG number density.

The first term within the right-hand side of Eqs. (12a)-(12c) denotes the neutral atom ionization assisted gain in positive ion density per unit time, second, third, and fourth term denotes the decrease in positive ion density per unit time due to electron-ion recombination, ion collection current at the N-NCN-VG Hybrid surface and adsorption of ion at the surface of N-NCN-VG Hybrid. The fifth term denotes positive ion density gain per unit time through ions desorption out of the surface of N-NCN-VG Hybrid. The term J_{th} describes the number density increase of hydrogen ion in plasma due to thermal assisted dehydrogenation. The term $\frac{P}{E_{disk}V}$ describes the rise in positive ion density owing to applied power-assisted dissociation. E_{disk} is the dissociation energy of type k neutral. The last term of the equation (12a)-(12c) represents ion density gain with ion–neutral reaction.

Eqs. (13a) - (13c) represent neutral atom number density equalization in plasma, χ_{ik} (≈ 1) denote coefficients of sticking of ion of type k.

The first term on RHS of Equation (13a)-(13c) represents the gain in neutral atom density per unit time through recombination of electron-ion, the second term represents ionization assisted decrease in neutral atom density, third and fourth term represents ion neutralization assisted, neutral atom density gain per unit time over N-NCN-VG Hybrid and loss in ion density per time through neutral atoms (type a, b, c) accretion on the N-NCN-VG Hybrid surface. The last term represents neutral atom density decrease through ion–neutral reactions.

2.4 Results and Discussion

An analytical model used in the present paper, explains the plasma sheath variations and growth of N-NCN-VG Hybrid (specifically the effect of plasma control parameters: total gas pressure and plasma power) including the effect on field emission characteristics of the hybrid. The analytical equations conferred above are worked out in parallel via MATHEMATICA SOFTWARE to study the effect of total gas pressure and input plasma power upon plasma constituents with properties that consequently regulate the dimensions of the N-NCN-VG, respectively. Appropriate boundary conditions, used to solve analytical equations namely, at t=0 are number density of electron n_{eo} (=10^{10}cm^{-3}), electron temperature T_{eo} (=2eV), ion temperature T_{io} (=0.16eV), neutral temperature T_{no} (=0.15eV). Substrate potential U_v= -300V, Substrate temperature T_s= (650 ^{o}C) Neutral atom mass type a $M_a = \left[(12\times x)+(1\times y)\ a.m.u.\ for\ C_xH_y\right]$, Ion mass type a $M_{ia} = \left[(12\times x)+(1\times y)\, a.m.u.\ for\ C_xH_y^+\right]$,

Shruti Sharma
Delhi Technological University

Neutral atom mass type b $M_b = \left[(1\times x)\, a.m.u.\ for\ H_x\right]$, Ion mass type b $M_{ib} = \left[(1\times x)\, a.m.u.\ for\ H_x^+\right]$, Neutral atom mass type c $M_c = \left[(14\times x)+(1\times y)\, a.m.u.\ for\ N_xH_y\right]$, Ion mass type c $M_{ic} = \left[(14\times x)+(1\times y)\, a.m.u.\ for\ N_xH_y^+\right]$ and volume of chamber $V_c = 1.05\times10^4 cm^3$. Initial ion number density of NH_3^+=10^7cm^{-3}, NH_4^+=10^{10}cm^{-3}, H_2^+=10^8cm^{-3}.Neutral atom density of type k η_{k0}=5x10^{12}cm^{-3}, where k= a, c. Initial neutral density of H=10^{13}cm^{-3},HCN=10^{11}cm^{-3}.Density of catalyst nickel$\left(\rho_{ct}\right) = 8.96 gcm^{-3}$, mass of catalyst nickel$\left(M_{cat}\right) = 58.96 a.m.u.$,diameter of catalyst nickel$\left(D^{\circ}\right) = 60 nm.$First effect of change of total gas pressure $\left(P_o\right)$upon growth of N-NCN-VG hybrid (e.g. height and radius of the nanocone, thickness, and height of the graphene sheet protruding from nanocone) due to variation in ion energy, electron temperature, and plasma composition with varying total gas pressure at fixed plasma power has been presented.

Figure 2.2 (a) showing ion energy in eV variations with increasing total gas pressure. As gas pressure increases, electron mean free path [30] and sheath width decreases [64], resulting in increased collisions among electrons, neutrals, and ions, thus making them speedily lose their energy.

Figure 2.2 (b) showing an increase in chemical sputtering/etching yield YI with increasing energy of bombarding hydrogen ions at normal angle of incidence on the growing N-NCN-VG Hybrid, following study conducted by Roth et al. [65]. Chemical sputtering/etching, affect the growth rate of Hybrid, as etching is proportional to the (i) flux of incoming hydrogen and nitrogen-based ions [66], (ii) the amount of C–C bond breaking occurrence for every ion (iii) the passivation probability of broken bond by atomic hydrogen and nitrogen.

Following this, Figure 2.3 a–c, shows decreasing etchant ion (NH_3^+, H_2^+,NH_4^+) number density with increasing gas pressure due to increase in collisional recombination reactions, following the study conducted by Mao et al. [30]. Along with it, relative hydrogen etchant density also decreases with increase of total gas pressure, [cf. Figure 3d], which can be explained from the fact that ionization, excitation, dissociation of constituent species i.e.,H_2, NH_3, C_2H_2 due to electron impact decreases due to decrease in electron temperature and electron number

density with increasing gas pressure [67], following study conducted by Mao et al. [30]. Following this, Figure 2.3 a–c, shows decreasing etchant ion (NH_3^+, H_2^+,NH_4^+) number density with increasing gas pressure due to increase in collisional recombination reactions, following the study conducted by Mao et al. [30]. Along with it, relative hydrogen etchant density also decreases with increase of total gas pressure, [cf. Figure 3d], which can be explained from the fact that ionization, excitation, dissociation of constituent species i.e.,H_2, NH_3, C_2H_2 due to electron impact decreases due to decrease in electron temperature and electron number density with increasing gas pressure [67], following study conducted by Mao et al. [30].

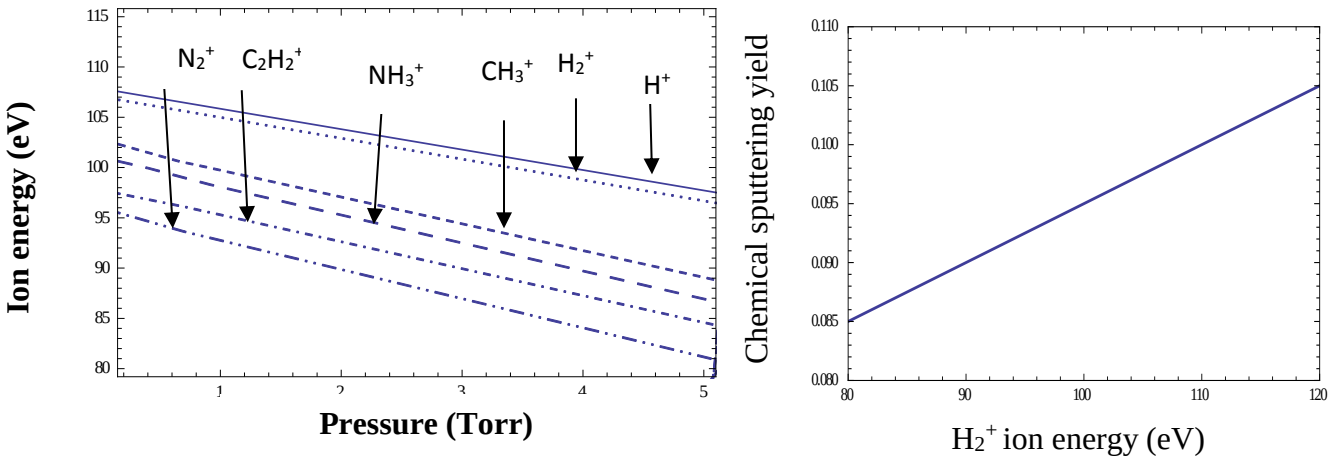

Figure 2.2 **a** Ion energy (eV) variation with total gas pressure (Torr) at 300 W, **b** Variation of chemical sputtering yield with H_2^+ ion energy (eV)

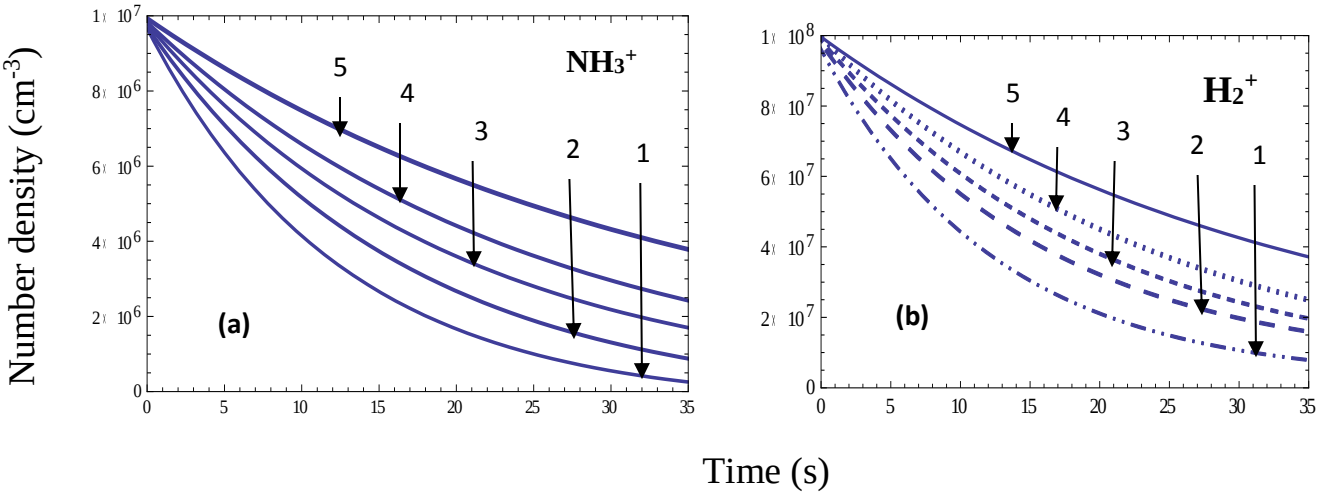

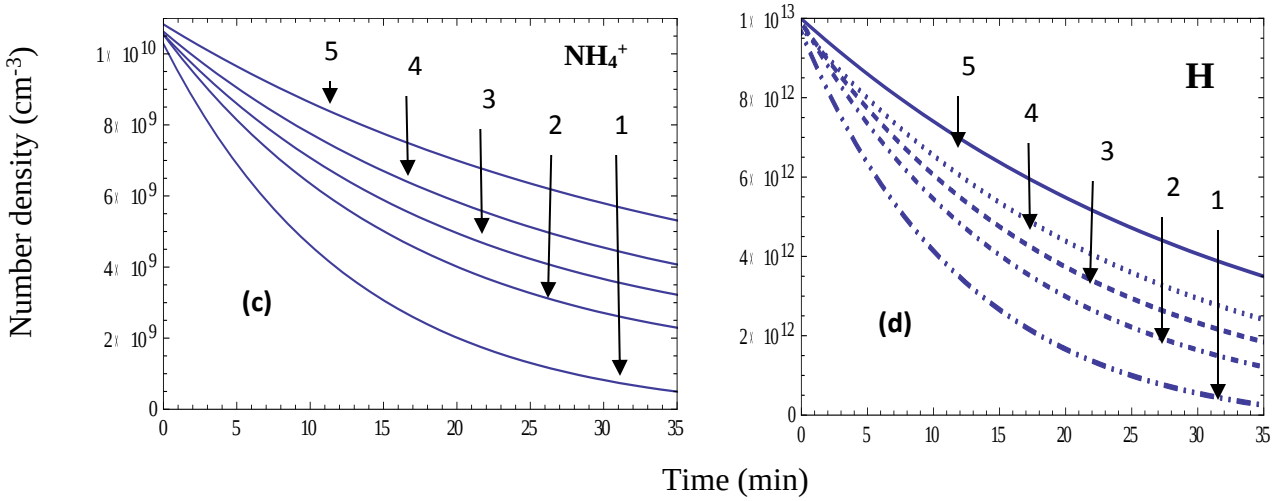

Figure 2.3 Time variation of number density of ions **a** NH_3^+, **b** H_2^+, **c** NH_4^+ and **d** Time variation of number density of H atoms for different total gas pressure, (1 = 5 Torr), (2 = 1.2 Torr), (3 = 950mTorr), (4 = 700mTorr), (5 = 200 mTorr)

Figure 2.4c shows surface concentration of carbon (S_C) increase with total gas pressure, ascribed to (1) reduced interaction of adsorbed hydrocarbon species on nanocone surface with etchant species from sheath. (2) Less nitrogen ion mediated reaction with hydrocarbon species takes place in plasma due to decreasing nitrogenous ion concentration, thus increasing the availability of carbon dimer (C_2) and carbon atoms for growth. (3) As C_2H_2 is the main growth precursor [68], so decreasing electron impact reaction with increasing pressure makes sufficient availability of C_2H_2. Consequently, growth rate of nanocone increases with increasing gas pressure [cf. Figure 4a], in compliance with studies of Parinov et al. [69], Chhowalla et al. [70], Ganjipour et al. [71]. Also extremely reactive H induced stabilization at relatively low pressure (250mTorr) limits the formation of sp_2 (highly crystalline structure) structure, thus slowing down nanocone growth at relatively low pressure.

Ion-induced dissociation of adsorbed hydrocarbons and ion decomposition reaction on growing nanocone decreases with an increase of plasma pressure [41] so limiting the carbon available for growth thereby preventing the formation of amorphous carbon.

In case of low pressure etching is more, resulting in nanocone of smaller tip radius [cf. Figure 2.4b] following study conducted by Parinov et al. [69], Kato et al. [72] Increasing the time of exposure of carbon nanocone under plasma environment gives rise to defect formation on the nanocone surface. Figure 2.4d illustrating the linear density of defects evolving with time over nanocone surface with varying total gas

pressure. Defect generation on nanocone surface is relatively low at 200 mTorr, which further increases with gas pressure. This can be explained by the fact that

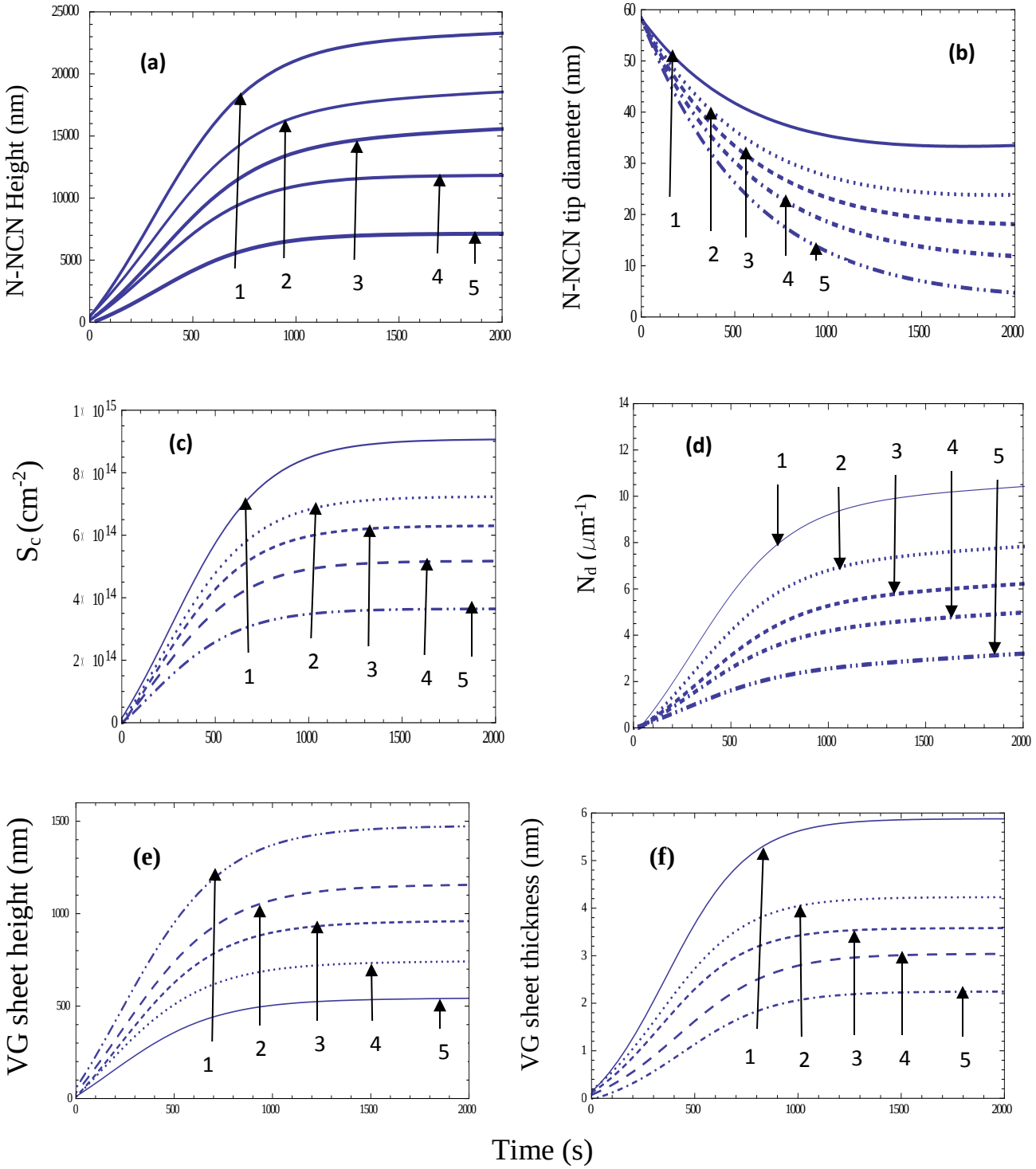

Figure 2.4 Time variation of **a** N-NCN height **b** N-NCN tip diameter **c** carbon surface concentration (Sc), **d** linear density of defects (Nd), **e** VG sheet height and **f** VG sheet thickness for different total gas pressure. (1 = 5 Torr), (2 = 1.2 Torr), (3 = 950mTorr), (4 = 700mTorr) (5 = 200mTorr)

nanoparticle [73]. At low-pressure etchant number density is high, so the number of carbon on the nanocone surface is low, whereas at high-pressure sufficient number of carbon are away from the catalyst nanoparticle surface which are available for the formation of defective structure. Also, the number of defects is proportional to the height of the nanocone [74], at low-pressure nanocone of small height is obtained, so number of defect on nanocone surface is low at relatively low pressure. An increase in the number of defects with gas pressure is following the study conducted by Garg et al. [75] where defect on edge of graphene increases with an increase in CH_4 gas pressure.

As discussed previously, nucleation of graphene sheet over nanocone surface is defect directed. Comparatively low pressure (200 mTorr) results in a drop in cluster formation on decreased defect sites due to the availability of fewer carbon atoms. These clusters further diffuse and agglomerate to form a small graphene island. As a consequence VG sheet number density decreases with a decrease in total gas pressure following the study conducted by Garg et al. [75]. Moreover, low availability of carbon Sc and relatively more of etchant number density in reactive plasma at relatively low gas pressure, results in decrease in VG sheet growth rate as shown in Figure 2.4e, following study conducted by Wei et al. [76]. Moreover, reasonably high etchant number density at relatively low pressure leads to the formation of VG sheet of comparatively less thickness as shown in Figure 2.4f, following study conducted by Hao et al. [77], Wang et al. [78] Figure 2.5a showing ion energy in eV variation with growth time at different input plasma power at fixed total gas pressure. An increase in plasma power at constant total gas pressure leads to an increase in plasma region volume accompanied by an increased electric field in plasma; as a consequence number density of electron, electron temperature, ion temperature, ionization of gases in the plasma increases. Figure 2.6a shows reduced surface concentration of carbon (Sc) with increasing plasma power. This is attributed to (1) increase in dissociation of neutrals C2H2, NH3 in plasma with increasing power makes less carbon available for growth, because it is mainly drawn from C2H2 reaction at nickel catalyst surface, [cf. Figure 2.5b], showing the time evolution of dissociation of C2H2 at different plasma power, in accordance to Bell et al. [68]. (2) CH4 production in the plasma increase with increase in power [79] and as C2H2 dissociates more readily on catalyst surface as compared to CH4, so Sc available for growth decreases [28].

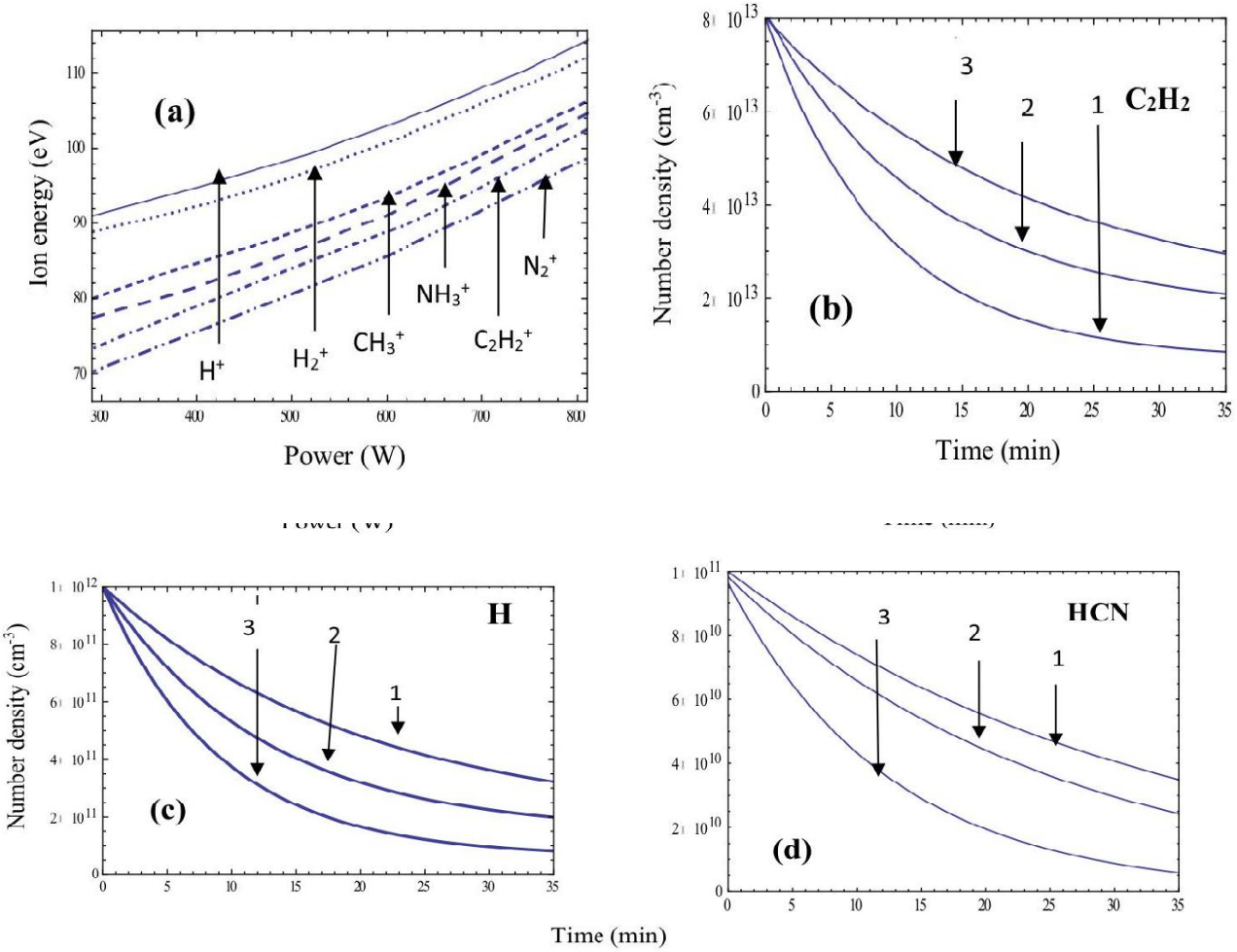

Figure 2.5 (**a)** Variation of Ion energy (eV) with Input Power (W) at 5 Torr and Time variation of number density of (**b)** C2H2 (**c)** H (**d)** HCN for different input power, (1 = 700 W), (2 = 500 W), (3 = 300 W) at 5 Torr

Shruti Sharma
Delhi Technological University

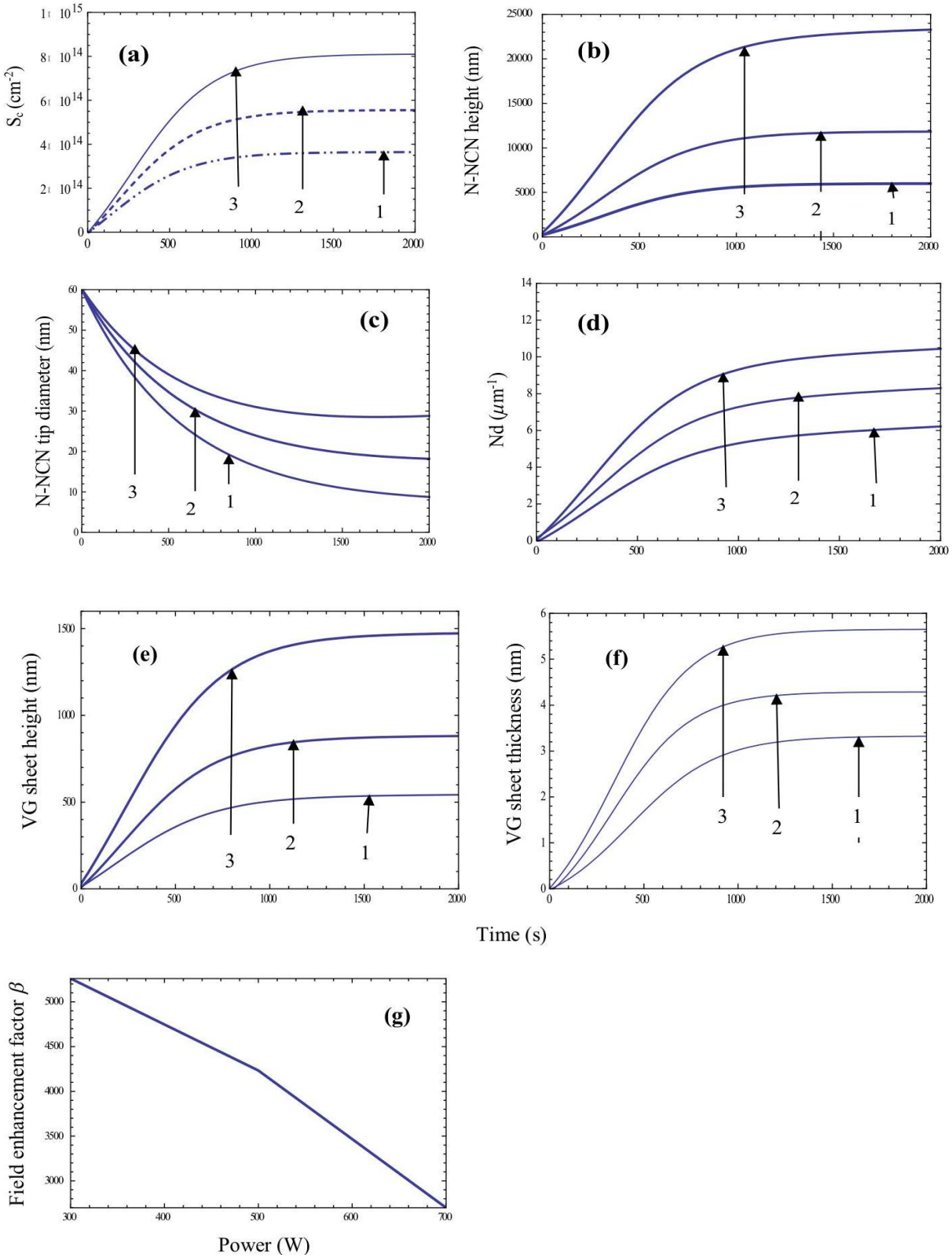

Figure 2.6 Time variation of (a) carbon surface concentration (Sc), (b) N-NCN height, (c) N-NCN tip diameter, (d)linear density of defects (Nd), (e) VG sheet height, (f) VG sheet thickness, for different input power (1 = 700 W), (2= 500 W), (3 = 300 W) at 5 Torr and (g) Field Enhancement factor β of N-NCN Hybrid at different input power at 5 Torr

Consequently the growth rate (length) of nanocone, [cf. Figure 2.6b] drops with increasing plasma power. Decrease in Sc and decreased growth rate of nanocone with plasma power are following a study conducted by Deng et al. [28]. Moreover, increasing plasma power favors hydrogen etchant [28] production [cf. Figure 2.5(c)] due to increased NH3 and C2H2 dissociation, which also contributes to decline in growth rate of nanocone with plasma power. Further, as power increases the high energy etchants (H, H2+, NH3+, HCN+) etches radius of nanotip so nanocone of smaller tip radius will be formed with increasing plasma power [cf. Fig. 6c] following the study of Merkulov et al. [80]. Figure 2.6d shows time varying, decreasing linear defect density over nanocone with increasing plasma power. This can be explained by availability of carbon (Sc) on the nanocone surface. As power increases from 300 to 700 W, Sc over nanocone surface decreases as discussed above, hence decreasing the defective structure along the nanocone surface [73]. Also, the number of defects is proportional to the length of the nanocone [74]. Relatively low Sc at nanocone surface at high plasma power leads to generation of small graphitic cluster at decreased defective sites. So we infer the formation of small size graphene island with decreased number density due to diffusion and agglomeration of these clusters. Hence, we outline that VG sheet number density decreases with increasing plasma power. In addition, (i) increase in active hydrogen concentration, with power, leads formation of volatile hydrocarbon species upon interaction with carbon on VG surface. (ii) Increase in HCN number density within plasma with plasma power, restrains carbon supply for VG sheet growth, owing to C–N triple bond strength 748 kJ mol−1 and H–CCH bond strength 556 kJ mol−1 [63]. This makes C2H2 to decompose preferably on nanocone surface than HCN, [cf. Figure 2.5d] showing time-varying HCN number density in plasma with increasing plasma power [79]. Consequently, growth rate of VG sheet decreases with increasing plasma power [cf. Figure 2.6e]. Moreover, highly energetic etchants at high power etches the sidewalls of the growing VG sheets, so thickness of VG sheet decreases with increase of plasma power [cf. Figure 2.6f]. The decrease in growth rate and thickness of VG sheet with increase in plasma power complies with Deng et al. [28] and Nang et al [81]. As discussed above with increasing power, the height of the nanocone and VG sheet decreases along with tip radius of the nanocone and thickness of the VG sheet. The finding of the above work is employed to find the field enhancement factor of the N-NCN-VG hybrid with varying plasma power (300–700 W).The field enhancement factor of nanocone $\beta_{NCN} \approx \left(\frac{h}{r_1}\right)$, $\beta_{VG} \approx \left(\frac{h_{gr}}{t_{gr}}\right)$, respectively. Therefore, field enhancement of the N-NCN-VG hybrid may be calculated as $\beta_{hybid} = \beta_{NCN}\beta_{VG}$ [82]. But in that case, the order of field enhancement factor of hybrid is about two orders more than the experimental values

of βhybrid. So in the present work βhybrid is estimated as a ratio of $(h + h_{gr})$ to t_{gr}. Figure 2.6g manifests that the field enhancement factor of N-NCN-VG hybrid decreases with increasing plasma power. Though thinner, nanocone and VG sheet are obtained at relatively high power, but nanocone and VG sheet (forming N-NCN-VG hybrid) obtained at relatively low power are much higher as compared to high power. Thus, obtaining N-NCNVG hybrid of increased field enhancement factor at relative low plasma power [cf. Figure 2.6g]. Increase in β with decrease in plasma power comply with experimental works of Deng et al. [28].

2.5 Conclusion

Theoretical model, comprising plasma sheath kinetics and surface processes is manoeuvred, to study the growth characteristics (height, tip diameter of nanocone, thickness, and height of VG sheet) of the N-NCN-VG hybrid by varying the plasma control parameters i.e., total gas pressure and input plasma power. Effect of ion energy, etchant number density, carbon surface concentration has been investigated concerning plasma control parameters. It is observed that N-NCN and VG sheet growth rate increases with an increase of total gas pressure and decreases with an increase of plasma power. The findings of varying plasma power on growth rate of N-NCN-VG hybrid are employed to calculate the field enhancement factor. It turns out that the field enhancement factor decreases with an increase of plasma power. This theoretical result complies with the experimental observation of Deng et al. [28]. The present study result can be widened to be realized as efficient field emitter devices.

References

1. Cole MT, Parmee RJ, Milne WI (2016) Nanotechnology **27**, 8. http://doi.org/10.1088/0957-4484/27/8/082501
2. Li X, Zhou J, Wu Q, Liu M, Zhou R, Chen Z (2019) J Vac Sci Technol B **37**,051203. https://doi.org/10.1116/1.5099697
3. Liang X, Xia J, Dong G, Tian B, Peng I (2016) Top Curr Chem **374,** 80. https://doi.org/10.1007/s41061-016-0083-6
4. Levchenko I, Xu S, Teel G, Mariotti D, Walker MLR, Keidar M (2018) Nat Commun **9**, 879. https://doi.org/10.1038/s41467-017-02269-7
5. Zhang J, Wang C, Zhou C (2012) ACS Nano **6**, 8. https://doi.org/10.1021/nn3026172
6. Singh LA, Walker MLR, Sanborn GP, Turano SP, Ready WJ, "Operation of spindt-type, carbon nanotube cold cathodes in a Hall effect thruster environment," paper presented at the 33rd International Electric Propulsion Conference, Washington D.C., USA, 6- 10 October 2013, Paper IEPC-2013–348
7. Deng JH, Liu RN, Zhang Y, Zhu WX, Han AL, Cheng GA (2017) J Alloys Compd **723**, 75–83. https://doi.org/10.1016/j.jallcom.2017.06.280
8. Liu J, Zeng B, Wang X, Wang W, Shi H (2013) Appl Phys Lett **103**, 053105. https://doi.org/10.1063/1.4816751
9. Qi JL, Zhang F, Zhang LX, Cao J, Feng JC (2014) Mater Res Express **1**, 025601. http://doi.org/10.1088/2053-1591/1/2/025601
10. Levchenko I, Xu S, Baranov O, Bazaka O, Ivanova EP, Bazaka K (2021) Molecules **26**, 4091, https://doi.org/10.3390/molecules26134091
11. Bazaka K, Levchenko I, Lim JWM, Baranov O, Corbella C, Xu S, Keidar M (2019) J Phys D Appl Phys **52**, 18. http://doi.org/ 10.1088/1361-6463/ab03b3
12. Gong J, Yang H, Yang P (2015) Compos B Eng **75**, 250–255. https://doi.org/10.1016/j.compositesb.2015.01.035
13. Koh ATT, Chen T, Pan L, Sun Z, Chua DHC (2013) J Appl Phys **113**, 174909. https://doi.org/10.1063/1.4804238
14. Li C, Li Z, Zhu H, Wang K, Wei J, Li X, Sun P, Zhang H, Wu D (2010) J Phys Chem C **114**, 33. https://doi.org/10.1021/jp1041487

15. Park SK, Choi K, Lee SH, Oh IK, Park S, Park HS (2017) Carbon **116**, 500–509. https://doi.org/10.1016/j.carbon.2017.02.024
16. Ye M, Hu C, Lv L, Qu L (2016) J Power Sources **305**, 106–114. https://doi.org/10.1016/j.jpowsour.2015.11.098
17. Xu T, Yang D, Fan Z, Li X, Liu Y, Guo C, Zhang M, Yu ZZ (2019) Electrochim Acta **152**, 134–143, https://doi.org/10.1016/j.carbon.2019.06.005
18. Park H, Ambade RB, Noh SH, Eom W, Koh KH, Ambade SB, Lee WJ, Kim SH, Han TH (2019) ACS Appl Mater Interfaces 11, 9011–9022. https://doi.org/10.1021/acsami.8b17908
19. Torrisi L, Rosinski M, Terwinska D, Tchorz P, Cutroneo M, Torrisi A (2020) Contrib Plasma Phys **60**, 1–15. https://doi.org/10.1002/ctpp.201900187
20. Zhu Z (2017) Nanomicro Lett 9, 25. https://doi.org/10.1007/s40820-017-0128-6
21. Yap YK, Menda J, Vanga LK, Kayastha V, Wang J, King LB, Dimovski S, Gogotsi Y (2004) MRS Online Proc Libr **821**, 147–151. https://doi.org/10.1557/PROC-821-P3.7
22. Kaushik V, Shukla AK, Vankar VD (2014) Appl Phys A Mater Sci Process 117, 2197–2205. https://doi.org/10.1007/s00339-014-8646-2
23. Xu Y, Deng P, Chen G, Chen J, Yan Y, Qi K, Liu H, Xia BY (2019) Adv Funct Mater **30**, 1906081. https://doi.org/10.1002/adfm.201906081
24. Jeong H, Nguyen DM, Lee MS, Kim HG, Ko SC, Kwac LK (2018) Mater Sci Eng C 90, 38– 45. https://doi.org/10.1016/j.msec.2018.04.039
25. Dasgupta K, Khosravifar M, Sawant S, Adusei PK, Kanakaraj SN, Kasik J, Shanov V (2020) C-J Carbon Res **6**, 40. https://doi.org/10.3390/c6020040
26. Kotal M, Sharma A, Jakhar S, Mishra V, Roy S, Sahoo SC, Sharma HK, Mehta SK (2020) Cryst Growth Des **20**, 4627–4639. https://doi.org/10.1021/acs.cgd.0c00430
27. Gautier LA, Borgne VL, Khakani MAE (2016) Carbon **98**, 259–266. https://doi.org/10.1016/j.carbon.2015.11.006
28. Deng JH, Cheng GA, Zheng RT, Yu B, Li GZ, Hou XG, Zhao ML, Li DJ (2014) Carbon 67, 525–533. https://doi.org/10.1016/j.carbon.2013.10.025
29. Gupta N, Sharma SC (2018) Phys Plasmas **25**, 073509. https://doi.org/10.1063/1.5030559
30. Mao M, Bogaerts A (2010) J Phys D Appl Phys **43**, 20. https://doi.org/10.1088/0022-3727/43/20/205201

31. Wang BB, Xu XZ, Zhang B (2007) Appl Surf Sci 253, 6951–6956. https://doi.org/10.1016/j.apsusc.2007.02.011
32. Levchenko I, Ostrikov K, Long JD, Xu S (2007) Appl Phys Lett **91**, 113115. https://doi.org/10.1063/1.2784932
33. Wang BB, Ostrikov K (2009) J Appl Phys **105**, 083303. https://doi.org/10.1063/1.3112025
34. Suzuki S (2011) In: Marulanda JM (ed) Low-Energy Irradiation Damage in Single-Walled Carbon Nanotubes, IntechOpen. https:// www. intechopen.com/chapters/16851
35. Zeng L, Lei D, Wang W, Liang J, Wang Z, Yao N, Zhang B (2008) Appl Surf Sci **254**, 1700–1704. https://doi.org/10.1016/j.apsusc.2007.07.131
36. Bo Z, Mao S, Han ZJ, Cen K, Chen J, Ostrikov K (2015) Chem Soc Rev **44**, 2108–2121. https://doi.org/10.1039/C4CS00352G
37. Wang BB, Zhu K, Ostrikov K, Shao RW, Zheng K (2016) J Appl Phys **119**, 024302. https://doi.org/10.1063/1.4939645
38. Wang BB, Zheng K, Cheng QJ, Ostrikov K (2015) Appl Surf Sci **325**, 251–257. https://doi.org/10.1016/j.apsusc.2014.11.072
39. Mehdipour H, Ostrikov K (2012) ACS Nano **6**, 11. https://doi.org/10.1021/nn3041446
40. Economou DJ, Evans DR, Alkire RC (1988) J Electrochem Soc 135, 756–763. https://doi.org/ 10.1149/1.2095737
41. Mehdipour H, Ostrikov K, Rider AE (2010) Nanotechnology **21**, 45. http://doi.org/10.1088/0957-4484/21/45/455605
42. Mehdipour H, Ostrikov K, Rider AE, Han Z (2011) Plasma Processes Polym **8**, 386–400. https://doi.org/10.1002/ppap.201000150
43. Marvi Z, Xu S, Foroutan G, Ostrikov K (2015) Phys Plasmas **22**, 013504. https://doi.org/10.1063/1.4905522
44. Srivastava SK, Shukla AK, Vankar VD, Kumar V (2005) Thin Solid Films **492**, 124–130. https://doi.org/10.1016/j.tsf.2005.07.283
45. Sodha MS, Misra S, Misra SK, Srivastava S (2010) J Appl Phys 107, 103307. https://doi.org/10.1063/1.3410676
46. Ostrikov K, Xu S, Plasma-Aided Nanofabrication From Plasma Sources to Nanoassembly, Wiley Publishers Since 1807, https://download.e-bookshelf.de/download/0000/6030/70/L- G-0000603070-0002364804. pdf

47. Dang C, Wang BB (2006) Thin Solid Films **514**, 76–80. https://doi.org/10.1016/j.tsf.2006.02.036
48. Bohdansky J, Roth J, Bay HL (1980) J Appl Phys **51**, 2861–2865. https://doi.org/10.1063/1.327954
49. .Hopf C, Jacob W (2005) J Nucl Mater **342**, 141–147. https://doi.org/10.1016/j.jnucmat.2005.04.003
50. Schluter M, Hopf C, Jacob W (2008) New J Phys **10**, 053037. https://doi.org/10.1088/1367-2630/10/5/053037
51. Chang JP, Arnold JC, Zau GCH, Shin HS, Sawin HH (1997) J Vac Sci Technol A **15**, 1853–1863. https://doi.org/10.1116/1.580652
52. Sigmund P (1969) Phys Rev **184**, 383–416. https://doi.org/10.1103/PhysRev.184.383
53. Gupta N, Gupta N, Sharma SC (2018) Phys Plasmas **25**, 043504. https://doi.org/10.1063/1.5020561
54. Gupta R, Sharma SC (2018) Contrib Plasma Phys **59**, 72–85. https://doi.org/10.1002/ctpp.201700138
55. Li J (2014) Thesis theoretical investigations of catalytic methane cracking and carbon nanotube growth. UWSpace. http:// hdl. handle. net/ 10012/ 8629. https:// uwspace. uwaterloo.ca/ bitstream/ handle/10012/ 8629/N_ Li_ Jingde. pdf? sequence= 1& isAllowed=y
56. Sharma SC, Gupta N (2015) Phys Plasmas **22**, 123517. https://doi.org/10.1063/1.4938506
57. Tewari A, Sharma SC (2015) Phys Plasmas **22**, 023505. https://doi.org/10.1063/1.4906876
58. Smith HMM, Langmuir I (1926) Phys Rev **28**, 36–45. https://doi.org/10.1103/PhysRev.28.36
59. Sodha MS, Kinetics of Complex Plasmas, Springer Series on Atomic, Optical, and Plasma Physic**81** http://77.151. 93. 113/ doc47/ LIVRES% 20Recopies/ Physiques% 20Ato mic% 2C% 20Optical% 2C%20and% 20Plasma/ Sodha% 20M.S.% 20-% 20Kinetics% 20of% 20Complex% 20Plasmas% 20-% 202014. pdf
60. Kennedy RV, Allen JE (2003) J Plasma Phys **69**, 485–506. https://doi.org/10.1017/S0022377803002265
61. Mantzaris NV, Gogolides E, Boudouvis AG, Rhallabi A, Turban G (1996) J Appl Phys **79**, 3718–3729. https://doi.org/10.1063/1.361205
62. See http:// www. udfa. net/ for database of neutral-ion reactions rate coefficients.

63. Hash DB, Bell MS, Teo KBK, Cruden BA, Milne WI, Meyyappan M (2005) Nanotechnology **16**, 925–930. https://doi.org/10.1088/0957-4484/16/6/050
64. Wang P, Lu J, Zhou O (2008) Nanotechnology **19**, 185605. https://doi.org/10.1088/0957-4484/19/18/185605
65. Roth J, Bohdansky J, Poschenrieder W, Sinha MK (1976) J Nucl Mater **63**, 222–229. https://doi.org/10.1016/0022-3115(76)90330-5
66. Luo Z, Lim S, You Y, Miao J, Gong H, Zhang J, Wang S, Lin J, Shen Z (2008) Nanotechnology **19**, 255607. https://doi.org/10.1088/0957-4484/19/25/255607
67. Mao M, Bogaerts A (2011) J Phys Conference Series **275**, 012021. https://doi.org/10.1088/1742-6596/275/1/012021
68. Bell MS, Teo KBK, Lacerda RG, Milne WI, Hash DB, Meyyappan M (2006) Pure Appl Chem **78**, 6. https://doi.org/10.1351/pac200678061117
69. Parinov IA (2015) Piezoelectrics and Nanomaterials: Fundamentals Developments and Applications. Nova Science Publishers, New York, pp 1–283
70. Chhowalla M, Teo KBK, Ducati C, Rupesinghe NL, Amaratunga GAJ (2001) J Appl Phys **90**, 5308–5317. https://doi.org/10.1063/1.1410322
71. Ganjipour B, Mohrajerzadeh S, Hesamzadeh H, Khodadadi A (2005) A Fuller Nanotube Carbon Nanostruct **13**, 365–373. https://doi.org/10.1081/FST-200039354
72. Kato T, Hatakeyama R (2010) J Nanotechnol **2010**, 256906. https://doi.org/10.1155/2010/256906
73. Ismail I, Mamat MS, Adnan NL, Yunusa Z, Hasan IH (2019) J Nanomaterials **2019**, 5717180. https://doi.org/10.1155/2019/5717180
74. Ferrari AC, Basko DM (2013) Nat Nanotechnol **8**, 235–246. https://doi.org/10.1038/nnano.2013.46
75. Garg R, Rastogi SK, Lamparski M, Barrera SC, Pace GT, Nuhfer NT, Hunt BM, Meunier V, Karni TC (2017) ACS Nano **11**, 6301–6311. https://doi.org/10.1021/acsnano.7b02612
76. Wei HW, Leou LC, Wei MT, Lin YY, Tsai CH (2005) J Appl Phys **98**, 044313. https://doi.org/10.1063/1.1993776
77. Hao J, Xu T, Liu W (2005) J Non-Crystalline Solids **351**, 3671–3676. https://doi.org/10.1016/j.jnoncrysol.2005.10.013

78. Wang Y, Li L, Cheng Q, He C (2015) J Lumin **161**, 7–13. https://doi.org/10.1016/j.jlumin.2014.12.052
79. Teo KBK, Hash DB, Lacerda RG, Rupesinghe NL, Bell MS, Dalal SH, Bose D, Govindan TR, Cruden BA, Chhowalla M, Amaratunga GAJ, Meyyappan M, Milne WI (2004) Nano Lett **4**, 921–926. https://doi.org/10.1021/nl049629g
80. Merkulov VI, Hensely DK, Melechko AV, Guillorn MA, Lowndes DH, Simpson ML (2002) J Phys Chem B **106**, 10570–10577. https://doi.org/10.1021/jp025647f
81. Nang LV, Kim ET (2012) J Electrochem Soc **159**, K93–K96. https://doi.org/10.1149/2.082204jes
82. Lv S, Li Z, Liao J, Wang G, Li M, Miao W (2015) Sci Rep **5**, 15035. https://doi.org/10.1038/srep15035

Chapter 3

Analytical modeling of nucleation and growth of graphene layers on CNT array and its application in field emission of electrons

3.1 Brief Outline

Carbon Nanotube (CNT) arrays and graphene have undergone several investigations to achieve efficient field emission (FE) owing to CNT's remarkable large aspect ratio and graphene's exceptional FE stability. However, when dense CNT arrays and planar graphene layers were used as field emitters, their field enhancement factor reduced dramatically. Therefore, in this paper, we numerically analyze the growth of a dense CNT array with planar graphene layers (PGLs) on top, resulting in a CNT-PGL hybrid and the associated field enhancement factor. The growth of the CNT array is investigated using Plasma Enhanced Chemical Vapor Deposition (PECVD) chamber in C_2H_2/NH_3 environment with variable C_2H_2 flow, Ni catalyst film thickness, and substrate temperature followed by PGL precipitation on its top at an optimized cooling rate and Ni film thickness. The analytical model developed accounts for the number density of ions and neutrals, various surface elementary processes on catalyst film, CNT array growth, and PGLs precipitation. According to our investigation, the average growth rate of CNTs increases and then decreases with increasing C_2H_2 flow rate and catalyst film thickness. CNTs grow at a faster rate when the substrate temperature increases. Furthermore, as the chamber temperature is lowered from 750°C to 250°C in N_2 environment and Ni film thickness grows, the number of the graphene layers increases. The field enhancement factors for the CNT array and hybrid are then calculated based on the optimal parameter values. The average height of the nanotubes, their spacing from one another, and the penetration of the electric field due to graphene coverage are considered while computing the field enhancement factor. It has been found that adding planar graphene layers to densely packed CNTs can raise its field enhancement factor. The results obtained match the current experimental observations quite well.

3.2 Introduction

Carbon nanomaterials having hexagonally arranged sp^2 hybridized carbon atoms are actively used in various application domains. They are divided into three categories based on their dimensional shape: one-dimensional (1-D) i.e. carbon nanotube (CNT), two-dimensional (2-D) i.e. graphene and three-dimensional (3-D) i.e. CNT-graphene hybrid. Carbon nanomaterials have the following set of properties: high electrical and thermal conductivity [1, 2, 3], improved surface area, high aspect ratio, field emission stability, flexibility, and low voltage requirement for electron extraction from its surface [4]. They are employed as electron field emitters [5,6] in X-ray generators [7], flat panel displays [8], microwave amplifiers [9], in electrodes for lithium-ion batteries for enhancing electron and Li-ion transport [10,11], in supercapacitors [12,13], in biosensors where CNT's are functionalized with biomolecules [14]. Moreover, they are used as field emitters mounted on hall effect thrusters and in space electric propulsion systems to increase channel wear resistance [15, 16, 17].

CNT- Graphene hybrid shows exemplary field emission (FE) owing to the adorable properties of both CNT and graphene, i.e., high aspect ratio, field emission stability and sharp edges of graphene [4, 18, 19].

PECVD (Plasma Enhanced Chemical Vapor Deposition) is the most widespread and versatile method for fabricating carbon nanostructures. In PECVD, the electrostatic force from the applied electric field causes ionization, generating electrons and ions that participate in various reactions (excitation, dissociation), forming radicals. Because of this, the technique can be operated at low temperatures without damaging the substrate and forming vertically aligned carbon nanostructures [20]. The nucleation of the carbon nanostructure in PECVD is controlled by the plasma species (ions, electrons, and neutral atoms) generated, catalyst film thickness, precursor gas flow rate, and plasma control parameters (gas pressure, applied plasma power, bias) [21, 22, 23, 24].

Choi et al. [25] reported that catalyst nanoparticles are formed by plasma pretreatment of the catalyst surface prior to hybrid growth in an optimum growth environment within a PECVD chamber. Extensive studies have shown that the graphene layer number, diameter, and crystallinity of CNT are determined by

catalyst film thickness and nanoparticle size [26, 27, 28]. It is also scrutinized that CNT array morphology can be directed by properly fixing the growth time, substrate temperature, and gas ratio [29, 30].

Chhowalla et al. [30] and Bell et al. [31] studied the effects of the C_2H_2/NH_3 feedstock flow ratio on CNT array growth. It was validated that when the concentration of C_2H_2 is high (>50%), pyramidal structures rather than vertical nanotubes emerge. Choi et al. [25] and Yu et al. [26] demonstrated the effects of cooling rate on the yield of graphene from Ni nanoparticles and flat Ni substrate, and proposed an optimal cooling rate for C precipitation. Shurman et al. [27] simulated the formation of CVD graphene on a thin Ni film at various growth parameters such as growth time, temperature, and Ni film thickness.

Felicitous designing of the CNT array and controlling its dimensions make it worthy as a field emitter in FE devices. Bonard et al. [32] investigated the effects of geometric configurations (density, height, radius, and distance between CNTs) on the FE properties of CNTs, and found that high-density CNT films are not a prerequisite for optimal field emission. Thapa et al. [29] investigated that single CNTs or less crowded CNT bundles provide better field emission than crowded CNT bundles. In comparison to pure CNT and graphene films, Kaur et al. [33] and Hong et al. [34] observed increased field emission from reduced graphene oxide (rGo) deposited CNT films over Ni foams as well as a decrease in turn on electric field and threshold electric field for graphene embedded CNTs.

Motivated by the aforementioned studies, the author has tried to model and numerically analyze the growth of the CNT-Planar graphene layer (PGL) hybrid. The author determined the optimal dimensions of the hybrid for enhanced field emission by analyzing the favorable C_2H_2 flow rate, Ni film thickness, substrate temperature, and cooling rate.

3.3 Model

This section works out the kinetics of plasma species and the growth of the CNT-PGL hybrid in C_2H_2/NH_3 plasma using fundamental assumptions and equations. Using the DC-PECVD process, a hybrid of PGLs and CNT arrays is designed over a Silicon (Si) substrate, covered with Ni film as a catalyst. Table 3.1 lists basic

reactants such as ions and neutrals of C_2H_2, NH_3, and H_2 that comprise C_2H_2/NH_3 plasma [35].

Table 3.1 Neutrals and ions taken into consideration [35, 36, 37, 38]

Neutrals			Ions		
Type j	Type k	Type l	Type j	Type k	Type l
C_2H_2, CH_4, CH_3, C_2H_3,C_3H_4, C_4H_2	H, H_2, H_3	NH_3, N_2, NH_4, HCN,	$C_2H_2^+$, CH_4^+, CH_3^+,$C_2H_3^+$, $C_4H_2^+$	H^+,H_2^+, H_3^+	NH_3^+, NH_4^+, HCN^+, CN^+

In the PECVD technique, when a negatively biased substrate surface with a catalyst film is exposed to a reactive plasma, an electric field arises between the bulk plasma and the substrate surface because of charge separation. The charge separation region is known as the plasma sheath. It is composed of both neutral molecules and positive ions. The electrostatic force arising from the plasma sheath accelerates ions toward the catalyst film surface, i.e., in the vertically downward direction (z-axis) [39], while neutrals undergo Brownian motion across the sheath. The plasma sheath equations (equations (1)-(5)) describe the plasma sheath. The parameters needed for hybrid growth namely the number density and speed of ions, as well as the number density of electrons within the plasma sheath are computed using the following continuity (equations (1) and (2)), momentum balance equations (equations (3) and (4)) for ions and electrons in plasma sheath respectively.

$$\frac{1}{n_{it}}\frac{\partial\left(n_{it}v_{it}\right)}{\partial z}=\tau, \tag{1}$$

$$\frac{1}{n}\frac{\partial\left(nv_{e}\right)}{\partial z}=\tau, \tag{2}$$

$$m_{it}v_{it}\frac{\partial v_{ik}}{\partial z}=-e\frac{\partial\phi}{\partial z}-m_{it}\iota_{it}v_{it}-\frac{T_{it}}{n_{it}}\frac{\partial n_{it}}{\partial z}, \tag{3}$$

$$m_{e}\iota_{e}v_{e}=e\frac{\partial\phi}{\partial z}-\frac{T_{e}}{n}\frac{\partial n}{\partial z}, \tag{4}$$

$$\frac{d^2\phi}{dz^2}=4\pi e\left(\sum_t \beta_{it}n_{it}-n\right), \tag{5}$$

Poisson's equation (equation (5)), determines the potential distribution within the plasma sheath [40, 41]. Table 3.2 provides the interpretation of each symbol used in equations (1) - (5).

Table 3.2 Symbols with their meanings used in equations (1)- (5)

Symbol	Meaning
m_{it},	Mass of positive ion (t corresponds to type j, k, l)
n_{it},	Number density of positive ions (t corresponds to type j, k, l)
T_{it},	Temperature of positive ions (t corresponds to type j, k, l)
ν_{it}	Velocity of positive ions (t corresponds to type j, k, l)
m_e,	Mass of electron
N	Number density of electrons
T_e	Temperature of electrons
ν_e	Velocity of electrons
τ	Ionization frequency of neutrals by electrons
$\iota_\eta = \left(\sigma_\eta N_u S_\eta\right)$	Collision frequency computing ions and electrons collisions with the neutrals
η	Refer to electrons and t (type j, k, l) ions
σ_η	Collision cross-section
s_η	Average speed of electrons and positive ions
N_u	Total neutral species number density.
$\boldsymbol{\beta_{it} = n_{it}/n}$	t^{th} ions to electrons number density ratio
ϕ	Electric sheath potential

Ultimately, the sheath equations are resolved by applying the following boundary conditions at plasma sheath interface i.e. at z = 0:

$$\phi = 0, \frac{d\phi}{dz} = -\frac{T_e}{e\lambda}, \nu_e = 0, \nu_{it} = \nu_{ito},$$

where $\nu_{ito} = \sqrt{\frac{T_e}{m_{it}}}$ is the ion –acoustic speed, $\lambda = \frac{T_i}{\sigma_\eta p_o}$ is the mean free path of ion, p_0 is total gas pressure, respectively [40].

Figure 3.1 illustrates the CNT-PGL hybrid's inculpated growth processes in a plasma environment. Initially under applied plasma power, during pre-etching of the Ni-catalyst film, the dissociation of NH_3 produces energetic electrons, hydrogen and ammonia ions, and neutrals. These plasma species strike at the Ni film due to an induced electric field (E) between the negatively biased substrate and bulk plasma to form Ni catalyst nanoparticles. These nanoparticles serve as nucleation sites for CNT array growth in the C_2H_2/NH_3 plasma environment [42]. The incoming fluxes of positive and neutral ions from the plasma are exposed to the catalyst nanoparticles, which aid in the formation of CNTs. Carbon and hydrogen species in the plasma dissociate and adsorb, across the catalyst surface through surface reactions. Adsorbed carbon atoms diffuse over the catalyst nanoparticle's surface and in bulk up to a diffusion length $\Lambda \approx \sqrt{(D_a t')}$ where t' is the diffusion time. Eventually, carbon atoms in the catalyst bulk begin to precipitate beneath the catalyst surface to direct the tip growth –mode (i.e. lift up of catalyst from the substrate surface) of the CNTs in the CNT array [43], in conjunction with etching by adsorbed hydrogen atoms and incoming nitrogen flux. The electrostatic force present in the plasma sheath causes CNTs to grow vertically [44]. While the array grows, the overall gas pressure is kept at 7 Torr.

After the CNT array growth, C_2H_2/NH_3 flow is terminated, plasma is turned off and the chamber is cooled to 250° C under N_2 flow with total gas pressure 22 Torr. The cooling rate is assumed linear [25]. Three cooling rates are taken into consideration

n: 5°C/s, 15°C/s, and 25°C/s. During the cooling period, carbon atoms begin to precipitate out of Ni nanoparticles with a driving force (F) due to the supersaturation of diluted carbon. These carbon atoms form tiny nuclei that expand and meet with one another leading to graphene growth. These graphene nuclei unite to form a planar graphene sheet by bridging the gaps across the Ni nanoparticles located at the tip of CNTs [25, 45, 46, 47]. As a result, a hybrid of CNT and PGL is formed.

3.3.1 Presumptions considered for simplified modelling [21, 48, 49]

(a) Maxwellian distribution of electrons and ions is considered.
(b) Ion – surface interaction is assumed to be coulomb interaction.
(c) For the sheath to perform its function and repel electrons, the potential must be monotonically decreasing with increase in z. This will occur if $n_{it}(z) > n(z)$ for all z in the sheath.

(d) Catalyst nanoparticle and substrate temperature is considered to be the same

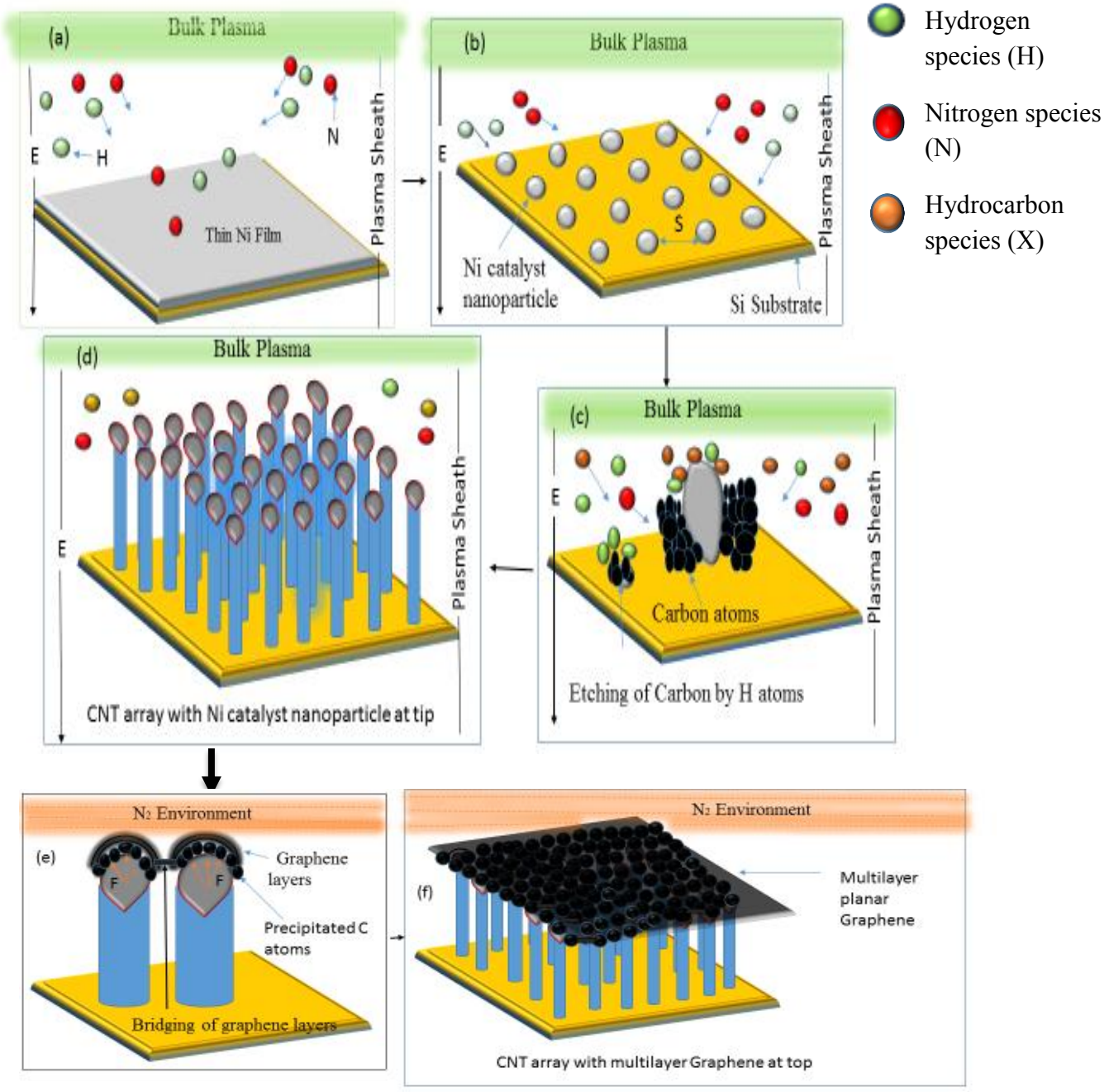

Figure 3.1. Schematic showing the (a) Pre-etching of the thin Ni film by incident plasma species in NH_3 plasma. (b) Cloven of Ni film into nanoparticles in NH_3 plasma. (c) Etching of carbon on Ni catalyst nanoparticle along with dissociation and adsorption of hydrocarbon and hydrogen species on catalyst nanoparticle surface in C_2H_2/NH_3 plasma. (d) Growth of CNT array via tip growth mode. (e) Precipitation of carbon atoms with driving force (F) to form graphene layers on Ni nanoparticle surface and bridging among graphene layers in N_2 environment. (f) CNT array with multilayer planar graphene at top.

3.3.2 Precipitation of carbon

Carbon atoms diffuse into Ni forming Ni-C bonds owing to its high solubility in Ni. When the chamber is cooled to a reasonably lower temperature, graphene formation occurs from diluted carbon in the Ni nanoparticles [50, 51]. When the carbon concentration in Ni reaches saturation during cooling, a Ni-C supersaturated solid solution is formed. Consequently, due to the difference in saturation while cooling, a driving force (F) comes into play, diffusing out carbon atoms from Ni bulk to surface and leading to carbon precipitation, following Arrhenius law. According to Arrhenius law, the dependence of carbon out-diffusion from Ni bulk on temperature is given by

$$D_a = D_o \exp\left(\frac{-U_{voc}}{k_B T_s}\right), \tag{6}$$

where, D_a is bulk diffusion coefficient, $D_o = \frac{D_{Ni} f}{2\pi}$, U_{voc} $(= 1.74\ eV)$ activation energy for diffusion of carbon atoms in Ni bulk [27,46], T_s is the catalyst surface temperature , f is thermal vibration frequency $(\approx 10^{13} Hz)$.

Let carbon concentration in Ni bulk along z direction, perpendicular to the surface be $C_{bulk}(z, t)$ where t is time. According to Fick's Law of diffusion, the rate of change of concentration at a point within Ni bulk due to diffusion is given by

$$\frac{\partial C_{bulk}}{\partial t} = D_a \nabla^2 C_{bulk}, \tag{7}$$

where, t represents time and $C_{bulk}(z,t)$ is estimated by

$$\frac{C_{bulk}(z,t) - C_o}{C_1 - C_o} = erf\left(\frac{z}{2\sqrt{D_a t}}\right), \tag{8}$$

The following boundary conditions are used to compute the $C_{bulk}(z, t)$.

$C_{bulk}(z, t)$ $(z>0, t=0) = C_1$ (Initial bulk concentration in Ni catalyst nanoparticle),

$C_{bulk}(z, t)$ $(z = 0, t) = C_o$ (bulk concentration adjacent to the Ni catalyst nanoparticle surface).

The number of planar graphene layers (N_{pg}) obtained at time t is then approximated to

$$N_{pg} \approx \left(\frac{\frac{D_a\left(C_1 - C_0\right)}{\sqrt{\pi D_a t}} \frac{V_{Ni}\rho_{Ni}}{M_{Ni}}}{N_a} \right), \tag{9}$$

where, N_a denotes surface concentration of atoms in one graphene layer ($\approx 3.8\times 10^{19} \frac{atoms}{m^2}$). [27, 45, 52, 53], V_{Ni}, ρ_{Ni} (=8.96 $g\ cm^{-3}$), and M_{Ni} (=58.69 amu) are the volume, density and mass of Ni catalyst nanoparticle.

3.3.3 Catalyst nanoparticles formation

During the pre-etching, owing to energy transfer (i.e. input power (P)) by plasma species, the catalyst film gets heated up and segregated. This is the result of multiple energy fluxes contributing viz power transfer due to: striking of plasma species, recombination reactions, chemical etching, incident ion sputtering, and energy loss to surroundings. Therefore the time-varying energy balance equation on Ni film in NH_3 plasma is,

$$P = \frac{\rho_{Ni} C_s T_s}{6} \frac{\partial \pi D_{Ni}^3}{\partial t} = \left[\sum_{t}^{k,l} \left[\xi_{it}\varepsilon_{it} + \xi_t \varepsilon_t + \xi_e \varepsilon_e \right] \right] + \left[\frac{3}{2} k_B T_s \sum_{t}^{k,l} \left(1 - \gamma_{it}\right)\xi_{it} \right] + \left[\left(\upsilon_o \sigma_{ads} F_k U \right) A \right] + \left[\left(\sum_{t}^{k,l} F_{it} Y_I\left(U_i\right)\left(1-\theta\right)A \right) \right] - \left[\sigma A \left(\eta_s T_s^4 - \eta_{surr} T_{surr}^4 \right) \right], \tag{10}$$

where, ξ_{it}, ξ_e, ξ_t denotes the collection current at the surface of Ni catalyst film due to positively charged ions of type t (k, l), electrons, and neutrals of type t (k, l) and are defined as,

$$\xi_{it} = \left[n_{it}(z) A \left(\frac{k_B T_{it}}{2\pi^2 m_{it}} \right)^{0.5} \left(\sqrt{\frac{4}{\pi}} \left(\frac{eV_c}{\pi k_B T_{it}} \right)^{0.5} + \exp\left(\frac{eV_c}{k_B T_{it}} \right) erfc\left(\frac{eV_c}{k_B T_{it}} \right)^{0.5} \right) \exp\left(\frac{-eU_c}{k_B T_s} \right) \right], \tag{10a}$$

$$\xi_e = n(z)A\left(\frac{k_B T_e}{2\pi^2 m_e}\right)^{0.5} \exp\left[\frac{eU_c}{k_B T_s}+\frac{eV_C}{k_B T_e}\right], \quad (10b)$$

$$\xi_t = n_t(z)A\left(\frac{k_B T_t}{2\pi^2 m_t}\right)^{0.5}, \quad (10c)$$

Description of other terms used in equations (10)-(10c) is given in table 3.3

Table 3.3 Description of terms in equations (10)-(10c).

Terms	Description
$n_{it}(z) = n_{it0}\left(1-\frac{2e\Phi(z)}{m_{it}v_{ito}^2}\right)$	Spatial dependence of ions within plasma sheath.
$n(z) = n\exp\left(\frac{\lvert e\rvert\Phi(z)}{k_B T_e}\right)$	Spatial dependence of electrons within plasma sheath.
$\Phi(z) = \Phi_0 \exp\left(\frac{-\lvert z\rvert}{\lambda}\right)$	Positional dependent potential within plasma sheath
$F_t = \left(\frac{n_t v_{thst}}{4}\right)$	Flux of impinging neutrals on the catalyst surface [54].
$F_{it} = \left(n_{it}\left(\frac{k_B T_{it}}{m_{it}}\right)^{0.5}\right)$	Flux of impinging ions on the catalyst surface [54].
$\varepsilon_\varsigma = \left(\left(\frac{2-qH_\varsigma}{1-qH_\varsigma}\right)-qH_\varsigma\right)k_B T_\varsigma$	Average energy collected at the surface of Ni catalyst film via ς (ions, neutrals of type t and electrons), $H_\varsigma = \left(\frac{U_B}{k_B T_s}\right)$, U_B is the energy barrier at the catalyst film surface [55].

The left-hand side of equation (10) accounts for the power transfer to Ni film and formation of Ni nanoparticle of diameter (D_{Ni}) with time.

The first term on the right-hand side in equation (10) represents the energy accumulated by striking ions, neutrals, and electrons over the surface. The second

term represents energy transfer via neutral formation on the surface. Energy transfer from chemical etching and incident ion sputtering is represented by the third and fourth terms. The last term accounts for energy loss from the surface to the surroundings.

Table 3.4 provides the interpretation of each symbol used in equations (10)- 10(c).

Table 3.4 Symbols with their meanings used in equations (10)-10(c)

Symbol	**Meaning**
C_s $(= 0.104\ cal\ g^{-1}\ ℃^{-1})$	Specific heat of Ni catalyst film
A	Area of Ni catalyst film
$\gamma_{it} (\approx 1)$	Sticking coefficient of positive ions of type t (j, k, l)
σ_{ads} $(= 6.8 \times 10^{-16}\ cm^2)$	Cross-section for reaction with atomic hydrogen
$\nu_o (\approx 10^{15} cm^{-2})$	Number of adsorption sites per unit area
η_{surr} $(= 1)$ and η_s $(= 0.12)$	Environment emissivity and Ni catalyst film emissivity
σ $(5.67 \times 10^{-5}\ ergs\ cm^{-2} s^{-1} K^{-4})$	Stefan's constant
$Y_I(U_i)$	Sputtering yield, dependent on ion energy [56]
V_C	Potential at surface of Ni catalyst film
$U_c = \varphi_o$	Substrate potential
k_B	Boltzmann constant
θ =0.01	Total surface coverage
U (=3.74 eV for Ni)	Binding energy of material surface [54]
T_S and T_{surr}	Substrate temperature and temperature of plasma environment
ν_{thst}	Thermal velocity of neutral species.

3.3.4 Charging of CNT-PGL Hybrid

Charge (Z') is evolved over the surface of the CNT- PGL hybrid because of the augmentation of positive charges and electrons, and is computed through equation,

$$\dot{Z}' = \sum_{w=1}^{r}\left(\sum_{t}^{j,k,l}\xi_{it}^{tipw} + \sum_{t}^{j,k,l}\xi_{it}^{curw} + \sum_{t}^{j,k,l}\xi_{it}^{pgw} - \Upsilon_e\left(\xi_e^{tipw} + \xi_e^{curw} + \xi_e^{pgw}\right)\right), \tag{11}$$

where, r represents number of CNTs , $\xi_{it}^{tipw}, \xi_{it}^{curw}, \xi_{it}^{pgw}$ represents the ion collection current at w[th] - CNT tip, curved surface and PGL and are defined as,

$$\xi_{it}^{tipw} = \left[\frac{\pi D_w^2}{4}\left(\frac{8k_BT_{it}}{\pi m_{it}}\right)^{\sqrt{0.25}} n_{it}(z)\left(1-Z_{CNT}\Psi_V\right)\exp\left(\frac{-eU_c}{k_BT_s}\right)\right], \tag{11a}$$

$$\xi_{it}^{curw} = \left[n_{it}(z)\frac{D_w}{2}L_w\left(\frac{2\pi k_BT_{it}}{m_{it}}\right)^{\sqrt{0.25}}\left(2\left(\frac{eV_{cur}}{\pi k_BT_{it}}\right)^{\sqrt{0.25}} + \exp\left(\frac{eV_{cur}}{k_BT_{it}}\right)erfc\left(\frac{eV_{cur}}{k_BT_{it}}\right)^{\sqrt{0.25}}\right)\exp\left(\frac{-eU_c}{k_BT_s}\right)\right], \tag{11b}$$

$$\xi_{it}^{pgw} = n_{it}(z)\left(\begin{matrix}l_{pgw}t_{pgw}\\ +t_{pgw}h_{pgw}\\ +h_{pgw}l_{pgw}\end{matrix}\right)\left(\frac{k_BT_{it}}{2\pi^2 m_{it}}\right)^{\sqrt{0.25}} \times \left(\begin{matrix}\frac{2}{\sqrt{\pi}}\left(\frac{eV_{pg}}{k_BT_{it}}\right)\\ +\exp\left(\frac{eV_{pg}}{k_BT_{it}}\right)erfc\left(\frac{eV_{pg}}{k_BT_{it}}\right)\end{matrix}\right)\times \exp\left(\frac{-eU_c}{k_BT_s}\right), \tag{11c}$$

D_w and L_w are the average height and diameter of the w[th] CNT in CNT array. l_{pgw}, t_{pgw} and h_{pgw} are the length, thickness and height of PGL on w[th] catalyst nanoparticle. $\Psi_v = \frac{2e^2}{D_w 4\pi\varepsilon_\circ}$, V_{cur} and V_{pg} denotes potential at tip, curved surface of w[th] CNT (refer Eq. (A1) of the Appendix) and at surface of PGL on w[th] catalyst nanoparticle [57].

$\xi_e^{tipw}, \xi_e^{curw}, \xi_e^{pgw}$ represents the electron collection current at w[th] - CNT tip, curved surface and PGL and are defined as,

$$\xi_e^{tipw} = \left[n(z)\pi \frac{D_w^2}{4} \sqrt{\left(\frac{8k_B T_e}{\pi m_e} \right)} \exp\left[\frac{Z_{CNT}\psi_V}{k_B T_e} + \frac{eU_c}{k_B T_s} \right] \right], \quad (11d)$$

$$\xi_e^{curw} = \left[n(z)\frac{D_w}{2} L_w \sqrt{\left(\frac{2\pi k_B T_e}{m_e} \right)} \exp\left[\frac{eV_{cur}}{k_B T_e} + \frac{eU_c}{k_B T_s} \right] \right], \quad (11e)$$

$$\xi_e^{pgw} = n(z)\left(l_{pgw} t_{pgw} + t_{pgw} h_{pgw} + h_{pgw} l_{pgw} \right) \left(\frac{k_B T_e}{2\pi^2 m_e} \right)^{\sqrt{0.25}} \left(\exp\left(\frac{eV_{pg}}{k_B T_e} + \frac{eU_c}{k_B T_s} \right) \right), \quad (11f)$$

In equation (11), on right-hand side, the first, second, and third term outlines the accreting positive charges of type j, k, l on CNT array and PGL with time whereas the last term depicts a decrease in charge due to electron accumulation with time.

3.3.5 Kinetics of electrons in plasma

The time evolution of electrons in the bulk plasma is attributed to ionization of neutral atoms, ion-electron recombination, electron collection current on the hybrid surface, and electron loss to the chamber wall. It is computed using the following equation,

$$\dot{n} = \sum_{t}^{j,k,l} \delta_t n_t - \sum_{t}^{j,k,l} \alpha_t n n_{it} - \gamma_e \Lambda_{hyb} \sum_{w=1}^{r} \begin{pmatrix} \xi_e^{tipw} + \xi_e^{curw} \\ + \xi_e^{pgw} \end{pmatrix} - K_{wall}^{e} n, \quad (12)$$

where, δ_t is the ionization coefficient of neutral atoms. α_t is the recombination coefficient of electrons and ions, and is expressed as $\alpha_t \left(= \alpha_{to} \left(\frac{300}{T_e} \right)^q \right) cm^3 \sec^{-1}$ with q (= -1.2) constant, $\alpha_{to} = 1.12\times10^{-7}$ $cm^3 sec^{-1}$. $\gamma_e(\approx 1)$ is the sticking coefficient of electrons, Λ_{hyb} represents hybrid number density. $K_{wall}^{e} n = \left(\frac{\gamma_e \nu_{the} Sn}{4V} \right)$ is the loss of

electrons per unit time per unit volume on the chamber wall , $v_{the}$is the thermal velocity of electrons ($\approx 5.13\times10^7$ cm sec^{-1}) S is the chamber surface area with inner diameter 32 cm and length 23 cm [58], V denotes the chamber volume ($\approx 1.05 \times 10^4 cm^3$).

The first term on the right-hand side of equation (12) represents the increase in electron density over time as a result of ionization of neutral atoms in plasma. The second and third terms represent the electron density timely decay induced by ion-electron recombination and collection current on the CNT-PGL Hybrid The final term represents the electron density loss on the chamber wall per unit time. For electron impact reactions [cf. 59, 60].

3.3.6 Kinetics of positive ions in plasma

The following equations describe the time evolution of positive ions in the bulk plasma due to, the ionization of neutral atoms, electron–ion recombination, ion collection current at the hybrid's surface, loss of ions to the chamber wall, thermal dehydrogenation, and ion-neutral reactions.

$$\dot{n_{ij}} = A_j - B_j - C_j - D_j + E_j + F_j - G_j , \qquad (13a)$$

$$\dot{n_{ik}} = A_k - B_k - C_k - D_k + E_k - F_k + G_k , \qquad (13b)$$

$$\dot{n_{il}} = A_l - B_l - C_l - D_l + E_l + F_l - G_l , \qquad (13c)$$

Description of the terms in equations (13a) – (13c) is provided in Table 3.5.

Table 3.5 Description of the terms in equation (13a) – (13c)

Terms	Description
$A_t = \delta_t n_t$	The rate of gain of ions of type t (t corresponds to type j, k, l) due to neutral atom ionization in plasma
$B_t = \alpha_t n n_{it}$	The rate of loss of ions of type t (t corresponds to type j, k, l) due to ion-electron recombination.

$C_t = \Lambda_{hyb} \sum_{w=1}^{r} \left(\xi_{it}^{tipw} + \xi_{it}^{curw} + \xi_{it}^{pgw} \right)$	The rate of loss of ion of type t (t corresponds to type j, k, l) due to the ion collection current at the hybrid surface.
$D_t = K_{wall}^{it} n_{it} = \left(\frac{\gamma_{it} v_{thit} S n_{it}}{4V} \right)$	The rate of loss of ions of type t (t corresponds to type j, k, l) to chamber wall
$E_j = \sum_i P_{ij} n_j n_{il}$	The rate of gain of ions of type j due to reaction between neutral of type j and ion of type l , as listed in Table 3.6
$F_j = \sum_i P_{ij} n_j n_{ik}$	The rate of gain of ions of type j due to reaction between neutral of type j and ion of type k, as listed in Table 3.6.
$G_j = \sum_i P_{il} n_l n_{ij}$	The rate of loss of ions of type l due to reaction between neutral of type l and ion of type j, as listed in Table 3.6.
$E_k = F_{th}$	The rate of gain of ions of type k due to thermal dehydrogenation
$F_k = \sum_i P_{ij} n_j n_{ik}$	The rate of loss of ions of type j due to reaction between neutral of type j and ion of type k, as listed in Table 3.6.
$G_k = \sum_i P_{ik} n_k n_{ik}$	The rate of gain of ions of type k due to reaction between neutral of type k and ion of type k, as listed in Table 3.6.
$E_l = \sum_i P_{il} n_l n_{ij}$	The rate of gain of ions of type l due to reaction between neutral of type l and ion of type j, as listed in Table 3.6.
$F_l = \sum_i P_{il} n_l n_{il}$	The rate of gain of ions of type l due to reaction between neutral of type l and ion of type l, as listed in Table 3.6.
$G_l = \sum_i P_{ij} n_j n_{il}$	The rate of loss of ions of type j due to reaction between neutral of type j and ion of type l, as listed in Table 3.6.
P_{it}	Rate constant for ion-neutral reactions, as listed in Table 3.6.
v_{thit}	Thermal velocity of ions of type t (t corresponds to type j, k, l) [60]

Table 3.6 Ion-neutral reactions between various species considered in the present plasma model [60, 61]

Reactions	Rate Constant (P_{it}) $\left(cm^3/_{sec}\right)$
$H^+ + CH_4 \rightarrow CH_3^+ + H_2$	2.30×10^{-9} [61]
$H^+ + CH_3 \rightarrow CH_3^+ + H$	3.40×10^{-9} [61]
$H^+ + NH_3 \rightarrow NH_3^+ + H$	5.20×10^{-9} [61]
$H^+ + C_2H_3 \rightarrow C_2H_3^+ + H$	2.00×10^{-9} [61]
$H_2^+ + H \rightarrow H^+ + H_2$	6.40×10^{-10} [61]
$H_2^+ + H_2 \rightarrow H_3^+ + H$	2.50×10^{-9} [61]
$H_2^+ + C_2H_2 \rightarrow C_2H_2^+ + H_2$	5.30×10^{-9} [61]
$CH_3^+ + C_2H_2 \rightarrow C_3H_3^+ + H_2$	1.15×10^{-9} [61]
$CH_3^+ + NH_3 \rightarrow NH_4^+ + CH_2$	3.04×10^{-10} [61]
$CH_4^+ + H_2 \rightarrow CH_5^+ + H$	3.50×10^{-11} [60]
$CH_4^+ + CH_4 \rightarrow CH_5^+ + CH_3$	1.50×10^{-9} [60]
$CH_4^+ + C_2H_2 \rightarrow C_2H_2^+ + CH_4$	2.72×10^{-9} [60]
$CH_4^+ + C_2H_2 \rightarrow C_2H_3^+ + CH_3$	2.45×10^{-9} [61]
$CH_4^+ + NH_3 \rightarrow NH_3^+ + CH_4$	2.70×10^{-9} [61]
$CH_4^+ + HCN \rightarrow HCNH^+ + CH_3$	1.20×10^{-9} [61]
$C_2H^+ + H_2 \rightarrow C_2H_2^+ + H$	1.25×10^{-9} [61]
$C_2H^+ + CH_4 \rightarrow C_2H_2^+ + CH_3$	3.70×10^{-10} [61]
$C_2H^+ + C_2H_2 \rightarrow C_4H_2^+ + H$	1.85×10^{-9} [61]
$C_2H^+ + HCN \rightarrow C_2H_2^+ + CN$	2.70×10^{-9} [61]
$C_2H_2^+ + H_2 \rightarrow C_2H_3^+ + H$	1.00×10^{-11} [61]
$C_2H_2^+ + CH_4 \rightarrow C_3H_4^+ + H_2$	6.25×10^{-10} [60]
$C_2H_2^+ + C_2H_2 \rightarrow C_4H_2^+ + H_2$	4.90×10^{-10} [61]
$C_2H_2^+ + NH_3 \rightarrow NH_3^+ + C_2H_2$	2.14×10^{-9} [61]
$C_2H_3^+ + HCN \rightarrow HCNH^+ + C_2H_2$	2.90×10^{-9} [61]
$C_2H_3^+ + NH_3 \rightarrow NH_4^+ + C_2H_2$	2.50×10^{-9} [61]
$H^+ + C_4H_2 \rightarrow C_4H_2^+ + H$	2.06×10^{-9} [61]
$C_3H_2^+ + C_3H_4 \rightarrow C_4H_3^+ + C_2H_3$	1.96×10^{-10} [61]
$HCN^+ + CH_4 \rightarrow C_2H_3^+ + NH_2$	2.60×10^{-10} [61]
$NH_3^+ + NH_3 \rightarrow NH_4^+ + NH_2$	2.10×10^{-9} [61]
$N_2^+ + NH_3 \rightarrow NH_3^+ + N_2$	1.94×10^{-9} [61]
$N_2^+ + CH_4 \rightarrow CH_3^+ + N_2 + H$	9.30×10^{-10} [61]
$CN^+ + NH_2 \rightarrow NH_2^+ + CN$	9.10×10^{-10} [61]
$CN^+ + NH_3 \rightarrow HCN^+ + NH_2$	2.00×10^{-9} [60]
$CN^+ + HCN \rightarrow HCN^+ + CN$	2.70×10^{-9} [61]
$HCN^+ + C_2H_2 \rightarrow C_2H_2^+ + HCN$	1.50×10^{-9} [61]
$HCN^+ + NH_3 \rightarrow NH_3^+ + HCN$	1.68×10^{-9} [61]

3.3.7 Kinetics of neutrals in plasma

The following equations describe the time evolution of neutrals in bulk plasma due to, electron-ion recombination, neutralization of ions at the hybrid's surface, ionization of neutral atoms followed by neutrals loss to the chamber wall, their accretion, adsorption, desorption over the hybrid surface, and numerous ion-neutral processes.

$$\dot{n_j} = H_j + I_j - J_j - K_j - L_j - M_j + N_j - O_j - P_j + Q_j \,, \qquad (14a)$$

$$\dot{n_k} = H_k + I_k - J_k - K_k - L_k - M_k + N_k + O_k - P_k \,, \qquad (14b)$$

$$\dot{n_l} = H_l + I_l - J_l - K_l - L_l - M_l + N_l - O_l - P_l + Q_l \,, \qquad (14c)$$

Description of the terms in equations (14a)-(14c) is provided in Table 3.7.

Table 3.7 Description of the terms in equations (14a)-(14c)

Terms	Description
$H_t = \alpha_t nn_{it}$	The rate of gain of neutrals of type t (t corresponds to type j, k, l) due to electron- ion combination.
$I_t = \Lambda_{hyb}(1-\gamma_{it})\sum_{w=1}^{r}\left(\xi_{it}^{tipw} + \xi_{it}^{curw} + \xi_{it}^{pgrw}\right)$	The rate of gain of neutrals of type t (t corresponds to type j, k, l) due to ion neutralization on hybrid surface.
$J_j = K_{wall}^{t} n_t = \left(\frac{\gamma_t D_t}{\ell}\right)$	The rate of loss of neutrals of type t to chamber wall. (t corresponds to type j, k, l) D_t =Diffusion coefficient of neutrals within plasma, ℓ = Effective diffusion length of cylindrical chamber [35, 62].
$K_t = \delta_t n_t$	The rate of loss of neutrals of type t due to ionization of neutral atoms (t corresponds to type j, k, l).

Shruti Sharma
Delhi Technological University

L_t= $\Lambda_{hyb}(\gamma_t)\sum_{w=1}^{r}\begin{pmatrix} j_{it}^{tipw} + j_{it}^{curw} \\ + j_{it}^{pgw} \end{pmatrix}$	The rate of loss of neutrals of type t due to their accretion at hybrid's surface (t corresponds to type j, k, l).
M_t= $F_{adt} = \frac{p_t}{\left(2\pi m_{it} k_B T_{it}\right)^{\sqrt{0.25}}} \times \frac{n_t}{F_t}$	The rate of loss of neutrals of type t due to their adsorption at hybrid's surface. p_t = partial pressure of adsorbing species (t corresponds to type j, k, l).
N_t= $F_{dest} = n_t f \exp\left(-\frac{U_{ads}}{k_B T_{it}}\right)$	The rate of gain of neutrals of type j due to their desorption from hybrid's surface with adsorption energy $U_{ads;}$ (t corresponds to type j, k, l).
$O_j = \sum_i P_{ij} n_j n_{il}$	The loss of neutrals of type j due to reaction between neutral of type j and ion of type l, as listed in Table 6.
$P_j = \sum_i P_{ij} n_j n_{ik}$	The loss of neutrals of type j due to reaction between neutral of type j and ion of type k, as listed in Table 6.
$Q_j = \sum_i P_{il} n_l n_{ij}$	The gain of neutrals of type l due to reaction between neutral of type l and ion of type j, as listed in Table 6.
$O_k = \sum_i P_{ij} n_j n_{ik}$	The gain of neutrals of type j due to reaction between neutral of type j and ion of type k, as listed in Table 6.
$P_k = \sum_i P_{ik} n_k n_{ik}$	The loss of neutrals of type k due to reaction between neutral of type k and ion of type k, as listed in Table 6.
$O_l = \sum_i P_{il} n_l n_{ij}$	The loss of neutrals of type l due to reaction between neutral of type l and ion of type j, as listed in Table 6.
$P_l = \sum_i P_{il} n_l n_{il}$	The loss of neutrals of type l due to reaction between neutral of type l and ion of type l, as listed in Table 6.
$Q_l = \sum_i P_{ij} n_j n_{il}$	The gain of neutrals of type j due to reaction between neutral of type j and ion of type l, as listed in Table 6.

3.3.8 Generation of hydrogen and carbon species over catalysts surface

The interaction of neutrals and ions of type j, k, and l with catalyst nanoparticles results in the formation of hydrogen radicals (H_a) and carbon species (C_a) on the catalyst surface.

Eq. (1)-(2) represent hydrogen radical and carbon species generation over all catalyst nanoparticles because of various surface processes namely adsorption of hydrogen, thermal dissociation of adsorbed hydrocarbon, ion induced dissociation of adsorbed hydrocarbon, hydrogen desorption, ion induced dissociation of adsorbed ammonia, hydrocarbon adsorption, decomposition of hydrocarbons and many others.

$$\dot{H}_a = \left\{ \sum_{w=1}^{s} \left[\begin{array}{l} \sum_k F_{kw}(1-\theta) + \sum_j O_{jsw} f \exp\left(\frac{-\delta U_{td}}{k_B T_s}\right) + \sum_{ij}\left(\sum_j \frac{O_{jsw} S_p}{a_o}\right) F_{ijw} - \sum_{il} F_{ilw} \\ -\sum_k O_{ksw} f \exp\left(\frac{-\delta U_{hd}}{k_B T_S}\right) - \sum_k O_{ksw}\sigma_{ads} F_{lw} - \sum_{ik}\left(\sum_k O_{ksw}\sigma_{ads}\right) F_{ikw} + \sum_{il}\left(\sum_l \frac{O_{lsw} S_p}{a_o}\right) F_{ilw} \end{array} \right] \right\}, \quad (15),$$

$$\dot{C}_a = \left\{ \sum_{w=1}^{s} \left[\begin{array}{l} \sum_j F_{jw}(1-\theta) + \sum_j O_{jsw} f \exp\left(\frac{-\delta U_{td}}{k_B T_s}\right) + \sum_{ij}\left(\sum_j \frac{O_{jsw} S_p}{a_o}\right) F_{ijw} + \\ \sum_{ij} O_{ijw} + \sum_{ik}\left(\sum_{ij} \frac{O_{ijw}\sigma_{ads}}{f}\right) O_{ikw} - C_{aw} f \exp\left(\frac{-Uevp}{k_B T_S}\right) - \Gamma_C \end{array} \right] \right\} \left(1-\Omega_c\right) \quad (16),$$

where $\dot{H}_a$ and $\dot{C}_a$ in Eqs. (15) and (16) represents variation in concentration of hydrogen radicals and carbon species over catalysts surface with time. θ is total surface coverage. $O_{tsw} (= \theta_t \nu_o)$ is areal concentration of neutral species of type t (t corresponds to type j ,k, l), on wth catalyst nanoparticle. θ_t is the surface coverage by species of type t. $\nu_o \approx (10^{15} cm^{-2})$ is adsorption sites per unit area. $\sigma_{ads} (= 6.8 \times 10^{-16}\ cm^2)$ is the cross-section for reaction with atomic hydrogen.

$\delta U_{td}(=2.1eV)$, $\delta U_{hd}(=1.8\,eV)$, $U_{evp}(=1.8eV)$ are thermal dissociation energy of hydrocarbons, desorption energy of hydrogen species, evaporation energy of carbon.[57]. f ($\approx 10^{13}Hz$) denotes thermal vibration frequency,

$S_p(\approx 10^{-2}(2.5+3.3\,U_i))$ is stitching probability, U_i is ion energy respectively.

Table 3.8 describes the surface processes accounted in Eqs. (15) and (16).

Table 3.8 Description of surface processes accounted in Eqs. (15) and (16)

Operating terms on wth catalyst particle	**Description**
$\sum_k F_{kw}\left(1-\theta_t\right)$	Neutral hydrogen adsorption $H_{2(plasma)} \rightarrow 2H_{(ads)}$
$O_{jsw} f \exp\left(\frac{-\delta U_{td}}{k_B T_s}\right)$	Adsorbed hydrocarbons thermal dissociation $C_2H_{3(ads)} \rightarrow 2C_{(ads)} + 3H_{(ads)}$, $CH_{3(ads)} \rightarrow C_{(ads)} + H_{(ads)} + H_{2(plasma)}$
$\sum_{ij}\left(\sum_j \frac{O_{jsw}S_p}{a_o}\right) F_{ijw}$	Dissociation of adsorbed hydrocarbons via ions $C_2H_2^+ + C_2H_{3(ads)} \rightarrow 2C_{(ads)} + 3H_{(ads)} + C_2H_2^+$
$\sum_k O_{ksw} f \exp\left(\frac{-\delta U_{hd}}{k_B T_S}\right)$	Desorption of hydrogen $H_{(ads)} \rightarrow H_{(des)}$
$\sum_k O_{ksw}\sigma_{ads} F_{kw}$	Loss of adsorbed hydrogen via interaction with incoming neutral hydrogen flux
$\sum_{ik}\left(\sum_k O_{ksw}\sigma_{ads}\right) F_{ikw}$	Loss of adsorbed hydrogen via interaction with incoming hydrogen ion flux
$\sum_{il}\left(\sum_l \frac{O_{lsw}S_p}{a_o}\right) F_{ilw}$	Hydrogen adsorption via ion assisted dissociation of adsorbed ammonia $NH_4^+ + NH_{4(ads)} \rightarrow N_{(ads)} + 4H_{(ads)} + NH_4^+$
$\sum_{il} F_{ilw}$	Hydrogen species loss owing to decomposition of ammonia ion $NH_4^+ \rightarrow N_{(ads)} + 2H_{2(plasma)}$
$\sum_j F_{jw}\left(1-\theta_t\right)$	Hydrocarbon adsorption on catalyst surface $C_2H_{3(plasma)} \rightarrow C_2H_{3(ads)}$ $CH_{3(plasma)} \rightarrow CH_{3(ads)}$

$C_{aw} f \exp\left(\frac{-Uevp}{k_B T_S}\right)$	Carbon evaporation $C_{(ads)} \rightarrow C_{(ev)}$
$\sum_{ik}\left(\sum_{ij}\frac{O_{ijw}\sigma_{ads}}{f}\right)O_{ikw}$	Carbon adsorption due to communing hydrocarbon and hydrogen ion $C_2H^+_{3(plasma)} + H^+_{(plasma)} \rightarrow 2C_{(ads)} + 2H_{2(plasma)}$
$\sum_{ij} O_{ijw}$	Decomposition of hydrocarbons ion $C_2H_3^+ \rightarrow 2C_{(ads)} + 3H_{(ads)}$ $CH_3^+ \rightarrow C_{(ads)} + H_{(ads)} + H_{2(plasma)}$
$(1-\Omega_c)$, $\Omega_c = C_a \pi D_w^2$	Impeding term representing formation of amorphous carbon on catalyst nanoparticle, hence inhibiting hydrocarbon dissociation on catalyst nanoparticle surface.
r_c	Flux of carbon species leaving the surface

3.3.9 Growth rate equation of CNT array

The average growth rate of wth CNT in the CNT array is assessed by the change in the average volume of wth CNT, represented by the left-hand side of equation (15). The outer diameter of the wth CNT is comparable to the diameter of the wth catalyst nanoparticle (D_{Ni}).

The right-hand side of equation (15) evaluates the growth processes of wth CNT in the CNT array. The carbon monomers and carbon clusters that are generated on the catalyst surface because of several surface processes - such as hydrocarbon adsorption, ion-induced and thermal dissociation of adsorbed hydrocarbons, decomposition of hydrocarbon ions, hydrocarbon and hydrogen ions interaction, diffuse over the surface and into the bulk of the wth Ni catalyst nanoparticle with different energy barriers. The temperature of the catalyst nanoparticles has a considerable impact on these diffusion processes. At lower catalyst temperatures, the surface diffusion process dominates CNT array growth, whereas at higher catalyst temperatures, CNT array growth is primarily owing to the bulk diffusion process, and at intermediate temperatures, both processes contribute. As a result, in this paper, we have studied both the diffusion process in CNT array growth because the temperature of the catalyst nanoparticle is assumed constant.

After this, the carbon atoms in w[th] Ni catalyst bulk precipitate out with an energy barrier for incorporation along the CNT-Ni interface and result in the formation of a graphitic cylindrical tube. The highly active hydrogen species contribute to array expansion by eliminating amorphous carbon from the w[th] catalyst surface during array formation. The expansion also incorporates the accumulation of neutrals of type j and l throughout the surface of w[th] CNT [56, 63]. The accumulated neutrals of type l in the CNTs lattice significantly affect the growth of CNTs.

$$\frac{\pi}{4}\frac{d\left(D_{Niw}^2-D_w^2\right)L_w}{dt}=$$

$$\frac{1}{r}\sum_{w=1}^{r}\left[\begin{array}{l}\left(\begin{array}{l}\frac{D_aD_{Niw}}{f}\exp\left(\frac{-U_{voc}}{k_BT_s}\right)\\+\frac{D_b}{f}\exp\left(\frac{-U_{arc}}{k_BT_s}\right)\\+\frac{D_c}{f}\exp\left(\frac{-U_{arcl}}{k_BT_s}\right)\\\frac{A_sD_{Ni}w}{f}\exp\left(\frac{-\delta U_{INc}}{k_BT_s}\right)\end{array}\right)\times\left(C_a\times\xi_{ij}\times\left(\frac{M}{\rho}\right)_w\right)\\+\left(\left[\pi D_{Niw}L_w\times H_a\times\xi_{ik}\times\left(\frac{M_{Ni}}{\rho_{Ni}}\right)_w\right]+\left[\left(\Upsilon_j\xi_j+\Upsilon_l\xi_l\right)\times\left(\frac{M}{\rho}\right)_w\right]\right)\end{array}\right], \quad (17)$$

The details of growth processes integrated in equation (17) are in given table 3.9.

Table 3.9 Details of growth processes and parameters integrated in equation (17)

Functions/Parameters	Description
$\frac{D_aD_{Niw}}{f}\exp\left(\frac{-U_{voc}}{k_BT_s}\right)$	Bulk diffusion of carbon monomer into w[th] catalyst nanoparticle.
$\frac{D_b}{f}\exp\left(\frac{-U_{arc}}{k_BT_s}\right)$	Diffusion of carbon monomer over surface of w[th] catalyst nanoparticle.
$\frac{D_c}{f}\exp\left(\frac{-U_{arcl}}{k_BT_s}\right)$	Diffusion of carbon cluster over surface of w[th] catalyst nanoparticle.

$\frac{A_s D_{Niw}}{f} \exp\left(\frac{-\delta U_{INc}}{k_B T_s}\right)$	Incorporation of carbon monomer into wth CNT through wth CNT - Ni confluence.
$\left[\pi D_{Niw} L_w \times H_a \times \xi_{ik} \times \left(\frac{M_{Ni}}{\rho_{Ni}}\right)_w\right]$	Etching of amorphous carbon over the wth catalyst nanoparticle surface.
$\left[\left(\Upsilon_j \xi_j + \Upsilon_l \xi_l\right) \times \left(\frac{M}{\rho}\right)_w\right]$	Accumulation of neutrals of type j and l throughout the surface of wth CNT
U_{voc} = (1.6 eV)	Energy barriers for bulk diffusion in catalyst nanoparticle [63]
U_{arc} = (0.3 eV)	Energy barriers for surface diffusion of carbon monomer over catalyst surface [63].
U_{arcl} = (0.48 eV)	Energy barriers for surface diffusion of carbon clusters over catalyst surface [64].
U_{INc}= (0.4eV)	Energy barrier for incorporation along CNT- Ni interface [63]
D_a	Bulk diffusion coefficients [63]
D_b ,D_c	Surface diffusion coefficients [63]
A_s	Incorporation speed of carbon monomer into wth CNT
M ($\approx$12g)	Mass of wth CNT
ρ	Density of wth CNT
Υ_t ($\approx$1)	Sticking coefficient of neutrals of type j and l [63]

3.3.10 Growth rate equation of PGL

When the chamber is cooled, carbon atoms begin to diffuse out from the bulk of the wth catalyst nanoparticles and onto its surface, forming graphene nuclei. These nuclei combine and bridge the spaces between nanoparticles to produce PGLs. Subsequently, the adsorbed carbon is then etched over the catalyst surface, resulting in clean graphene layers**.**

The growth of PGL is computed in terms of areal (thickness (t_{pg}), and height (h_{pg})) change with time, as expressed by the left-hand side of equation (18).

$$l_{pg}\frac{d\left(h_{pg}\times t_{pg}\right)}{dt}=\sum_{w=1}^{r}\left[\left(D_a\frac{\left(C_1-C_0\right)}{\sqrt{\pi D_a t}}\pi D_{Niw}^2+\frac{\left(C_1-C_0\right)}{\sqrt{\pi D_a t}}D_b\pi D_{Niw}^2+y_i I_K n_{it}\vartheta_0\theta_c l_{pgw}h_{pgw}\right)\frac{M_{wpg}}{\rho_{wpg}}\right],$$

(18)

where, M_{wpg} (≈12g) and ρ_{wpg} are the mass and density of graphene layer on wth catalyst nanoparticle. y_i and I_K are the etching yield and rate coefficient for ions incident on the catalyst nanoparticle [65].

The right-hand side of equation (16) includes the growth processes involved in PGL growth. The first phrase refers to the outward diffusion of carbon atoms from the bulk of the wth Ni catalyst nanoparticle, followed by diffusion over the catalyst surface to generate graphene layers with activation energy barriers [66]. The final part of the equation represents the etching of adsorbed carbon atoms over the catalyst surface, promoting the formation of clean graphene.

3.3.11 Field enhancement factor

Understanding the field emission characteristics requires the study of the field enhancement factor. Equations (17) and (18) show the approximated field enhancement factor of the CNT array and CNT-PGL hybrid.

$$\beta_a\approx\beta\left\{1-\exp\left(-2.3172\frac{s}{L_w}\right)\right\},\tag{19}$$

$$\beta_{hyb}\approx\beta_a\times\beta_g\times\exp(-\phi'),\tag{20}$$

where β_a and β_{hyb} denotes the field enhancement factor of CNT array and CNT-PGL hybrid. $\exp(-\phi')$ refers to the exponential fall in field enhancement factor owing to a decrease in electric field penetration due to graphene coverage over the CNT array, with $\phi = \sigma'\sqrt{\mu}\Big/\sqrt{\varepsilon}$. σ', μ, ε, β_g are the conductivity, electric dipole moment, dielectric constant, and field enhancement factor of PGL. s is the spacing among CNTs [32, 67, 68, 69, 70, 71, 72].

3.4 Results and Discussion

In this paper, an analytical model is used to describe the growth of the CNT-PGL hybrid under appropriate conditions i.e., C_2H_2 flow rate, catalyst film thickness, substrate temperature, and cooling rate. The analytical model incorporates first-order simultaneous differential equations for plasma sheath, plasma species densities, carbon and hydrogen species surface concentration, growth rate of CNT array and PGL as well as field enhancement factor of CNT and CNT-PGL hybrid. The equations are solved via Mathematica software. In computations, we use substrate area to be 500 x 500 μm^2 covered with Ni film, with average centre-to-centre spacing (s) of 1 μm among the catalyst nanoparticles formed. Tables 3.10 and 3.11 list relevant initial conditions and parameters that were determined experimentally. They are utilized to solve equations presented in section (2) at t = 0.

Table 3.10 Initial number density of various plasma species considered in present model [48, 66, 73, 74].

Species	Mass (1 amu= 1.66×10^{-27} kg)	Number density (cm^{-3})
Electron	0.0005486 amu	7×10^{10}
C_2H_2	26 amu	7×10^{13}
CH_4	16 amu	2×10^{14}
CH_3	15 amu	1×10^{13}
C_2H_3	27 amu	7×10^{13}
C_3H_4	40 amu	3×10^{13}
C_4H_2	50 amu	1×10^{13}
H_2	2 amu	2×10^{15}
H	1 amu	3×10^{13}
H_3	3 amu	5×10^{15}
NH_3	17 amu	5×10^{13}
NH_4	18 amu	2×10^{11}
HCN	27 amu	9×10^{11}
N_2	28 amu	4×10^{9}
$C_2H_2^+$	26 amu	7×10^{8}
CH_3^+	15 amu	2×10^{8}
$C_2H_3^+$	27 amu	2×10^{7}
$C_4H_2^+$	50 amu	7×10^{7}
H_2^+	2 amu	1×10^{8}
H^+	1 amu	1×10^{8}

H_3^+	3 amu	1×10^8
NH_3^+	17 amu	9×10^8
NH_4^+	18 amu	1×10^9
HCN^+	27 amu	1×10^8
CN^+	26 amu	1×10^8

Table 3.11 Parameters used in present model [25, 37]

Parameters	**Value**
Electron temperature (T_{eo})	2.2 eV
Neutral temperature (T_{no})	0.17 eV
Ion temperature (T_{io})	0.15 eV
Plasma Power	120 W
Substrate Potential (U_c)	-500 V
Substrate temperature (T_s)	750°C
sGas pressure while CNT array growth	7 Torr
Gas pressure while graphene growth	22 Torr
Initial bulk concentration in Ni catalyst nanoparticle (C_1)	0
NH_3 gas flow rate	200sccm
N_2 flow rate	10,000 sccm

In the present analysis, the obtained potential distribution inside the plasma sheath, ion, and neutral density are used to compute the average diameter (D_{Ni}) of the catalyst nanoparticle together with hydrogen and carbon flux over the catalyst surface. The obtained carbon and hydrogen flux are used to calculate the growth rates of planar graphene and CNT arrays. Then we start the next time by solving the differential equations again, with new boundary conditions derived from the dimensions of the recently acquired hybrid.

First, we analyze the effect of C_2H_2 flow rate, catalyst film thickness, and substrate temperature on the growth of the CNT array, followed by an analysis of the growth of PGL over the CNT array by cooling the chamber.

3.4.1 Time variation of CNT array growth with C_2H_2 gas flow rate

Lighter and etchant ions (NH_4^+, HCN^+, $C_2H_2^+$, $C_2H_3^+$, H_2^+) are predominant under low C_2H_2 gas flow rate [cf. figure 3.2 (a)-(e)] assisting in the formation of a clean

CNT array [75]. With further increase in C_2H_2 gas flow rate, the neutral number density of type j in plasma bulk increases [cf. figure 3.2 (f)-(i)] leading to their increased adsorption on the catalyst surface. In addition, NH_3 is insufficient to suppress the decomposition of C_2H_2. So low etchant ion density and insufficient NH_3 at high C_2H_2 flow rate results in excess carbon deposition as amorphous carbon, poisoning the catalyst particle, retarding the CNT array growth. Hence, at a low C_2H_2 gas flow rate (i.e. up to 60 sccm) the relative carbon and hydrogen radical surface concentration [cf. figure 3.3 (a)-(b)] is competent for an increase in the growth rate of CNT, as carbon species generated over the surface of the catalyst are deposited and amorphous carbon is etched.

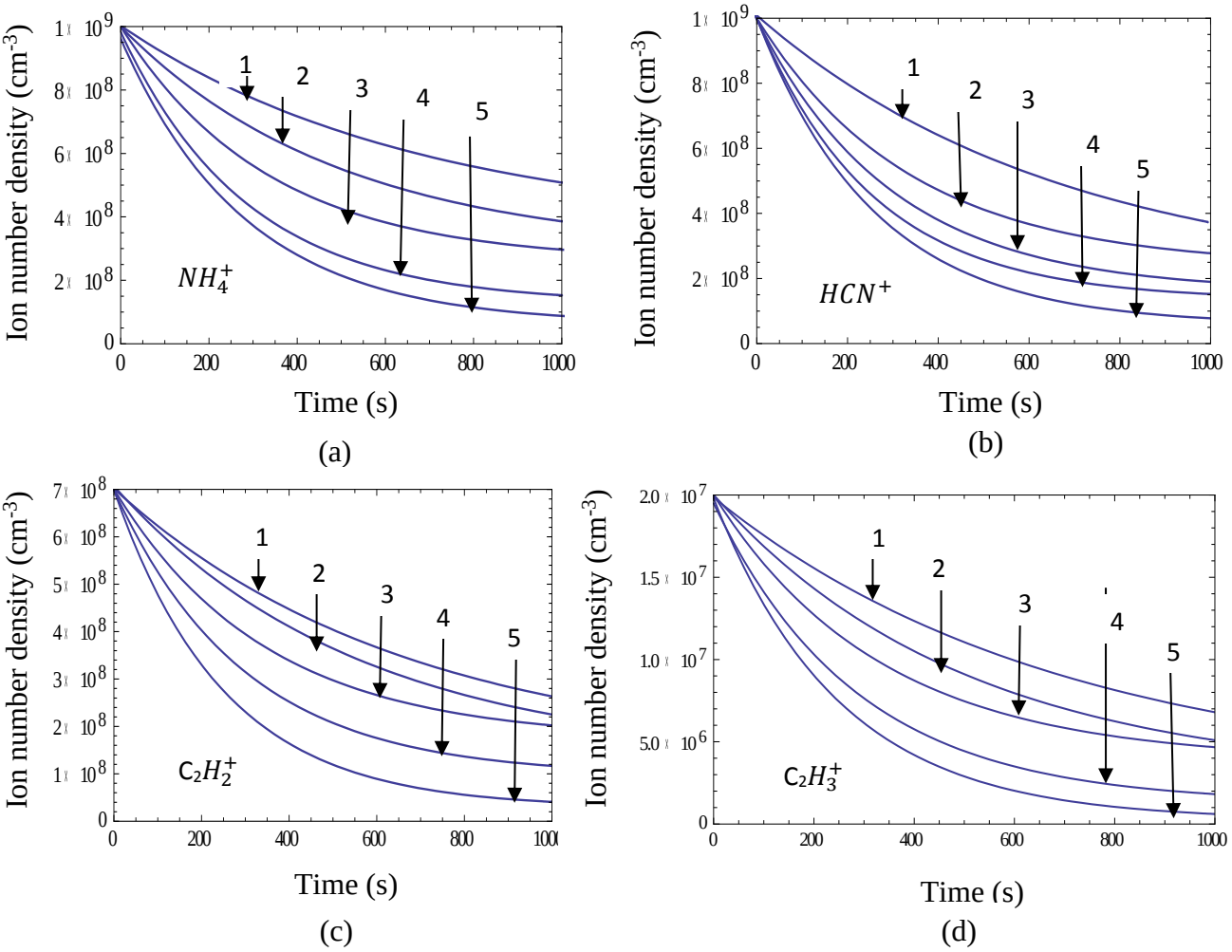

Shruti Sharma
Delhi Technological University

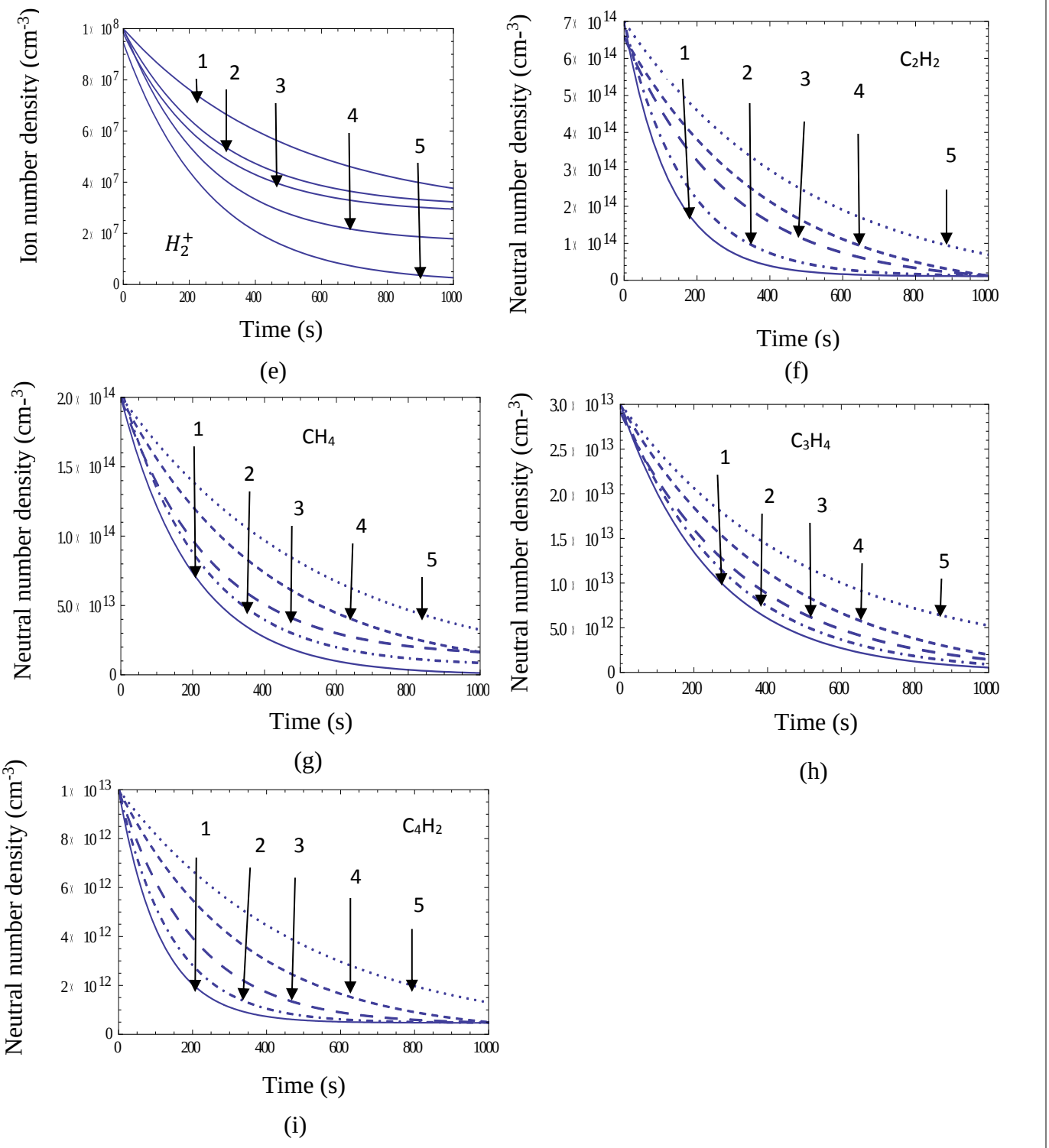

Figure 3.2 Time varying ion and neutral number density of (a) NH_4^+, (b) HCN^+ (c) $C_2H_2^+$ (d) $C_2H_3^+$ (e) H_2^+ (f) C_2H_2 (g) CH_4 (h) C_3H_4 (i) C_4H_2 varying C_2H_2 flow rate and constant NH_3 flow rate (200 sccm). (1=20 sccm), (2= 40 sccm), (3= 60 sccm), (4=100 sccm) (5=150 sccm)

Figure 3.3(c) shows that the average CNT height in the CNT array increases up to a C_2H_2 flow rate of 60 sccm and then it declines with a further rise in C_2H_2 flow at fixed ammonia (NH_3) gas flow rate (200 sccm). Chhowalla et al. [30] reported an initial increase in CNT growth rate up to 30% C_2H_2 concentration then it dropped further and according to Bell et al. [31], CNTs are well aligned between 4 and 20% of C_2H_2, with a growth peak at 20%. At 29% C_2H_2, CNTs resemble obelisks while at 38%, amorphous C deposition was detected.

Because of carbon deposition on the catalyst nanoparticle surface, the average diameter of CNTs in an array increases as the flow rate of C_2H_2 increases [cf. figure 3.3 (d)]. The findings are in line with Merkulov et al. [76], who found a 36 nm tip diameter at a C_2H_2/NH_3 ratio of 0.625 and a 46 nm tip diameter at a ratio of 0.80.

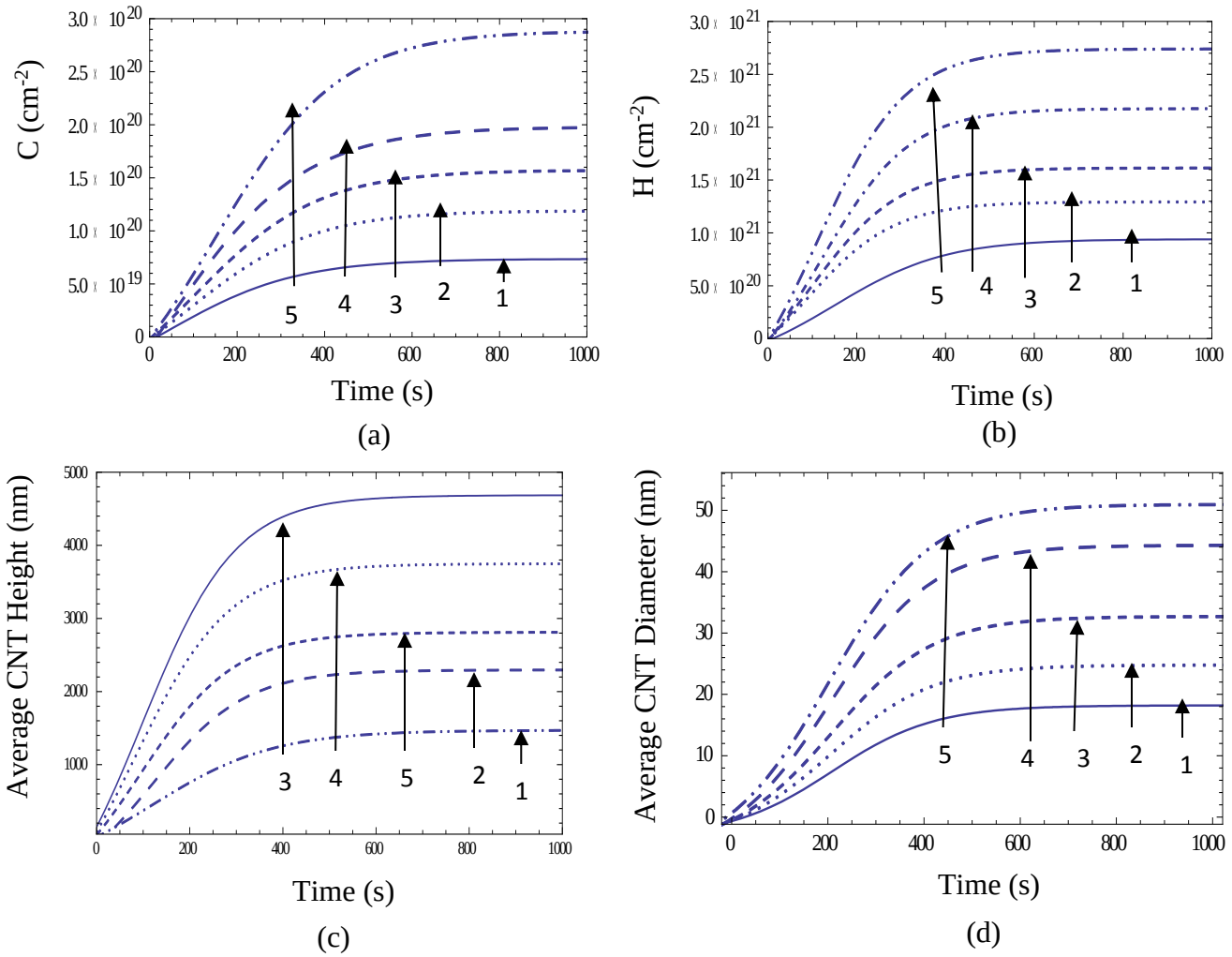

Figure 3.3 Time varying (a) Surface concentration of Carbon (C_a), (b) Surface concentration of Hydrogen (H_a), (c) Average CNT Height, (d) Average CNT diameter for varying C_2H_2 flow rate and constant NH_3 flow rate (200 sccm). (1=20 sccm), (2= 40 sccm), (3= 60 sccm), (4=100 sccm) (5=150 sccm)

3.4.2 Variation of CNT array length and diameter with catalyst thickness

Figure 3.4(a) shows the average CNT height in an array with increasing Ni film thickness. As thickness increases (up to 10 nm), catalyst particle size increases, raising average CNT height because catalyst particle remain active for dissolution, surface, and bulk diffusion of C- atoms [77]. Above 10 nm thickness, a decrease in average CNT height is observed owing to an increase in diffusion length of carbon inside the catalyst particle, so not enough particles can diffuse out from the catalyst bulk; consequently, shorter nanotubes are obtained. The obtained results comply with the studies of Lee et al. [77] where an increase of Ni catalyst thickness from 4 to 10 nm, enhances the length and growth rate of CNT by a factor of 0.7. As per Han et al. [78], the acquired data indicate that, in the case of a 100 nm Ni layer, carbon nanoparticles rather than carbon nanotubes appear in the SEM pictures [cf. figure 2 of Han et al. [78]]. Ma et al. [79] conducted an experiment wherein they noticed that the average length of CNTs decreased with increasing Ni film thickness up to 20 nm [cf. figure 4 of Ma et al. [79]].

Additionally, the size of the Ni nanoparticles, which grow with Ni film thickness, controls the average diameter of CNT [cf. figure 3.4(b)]. This comes after Han et al.'s study [78], in which the mean diameter of CNTs increased from 32 to 113 nm when the thickness of the Ni film increased from 10 to 100 nm.

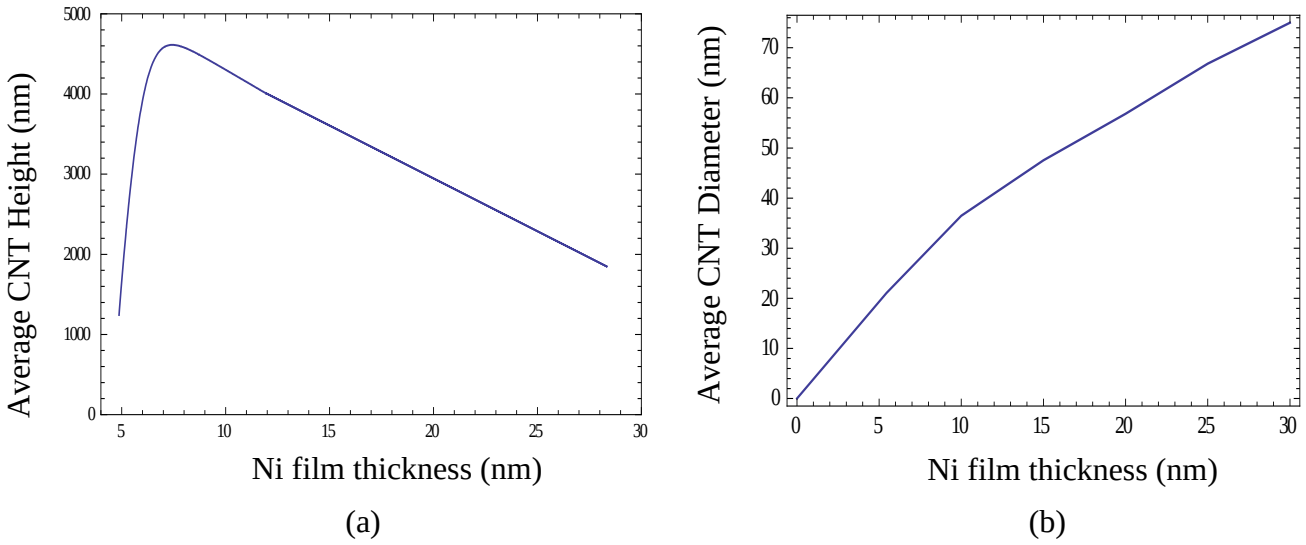

Figure 3.4 (a) Average CNT Height, (b) Average CNT diameter for varying Ni film thickness

3.4.3 Variation of growth rate of CNT array with substrate temperature

With increasing substrate temperature, the concentration of carbon atoms (C_{bulk}) inside Ni catalyst nanoparticles increases [cf. figure 3.5(a)] .This can be attributed to an increase in ion-driven hydrocarbon and ammonia species dissociation and decomposition over Ni catalyst nanoparticle. As a result, C_a and H_a increases across Ni nanoparticle surface. Increases in H_a cause etching, which removes excess carbon from the Ni surface. This opens up the catalyst surface area, allowing a larger intake of carbon and a rise in carbon atom solubility [80] and diffusivity. Studies by Bleu et al. [81], Shurman et al. [27], have shown that the concentration of carbon in the Ni bulk increases with substrate temperature.

As a result, the average growth rate of CNT in the array rises [cf. figure 3.5 (b)].This is in line with research done by Chhowalla et al., who found that CNT height increased between 520° C and 700° C [30].

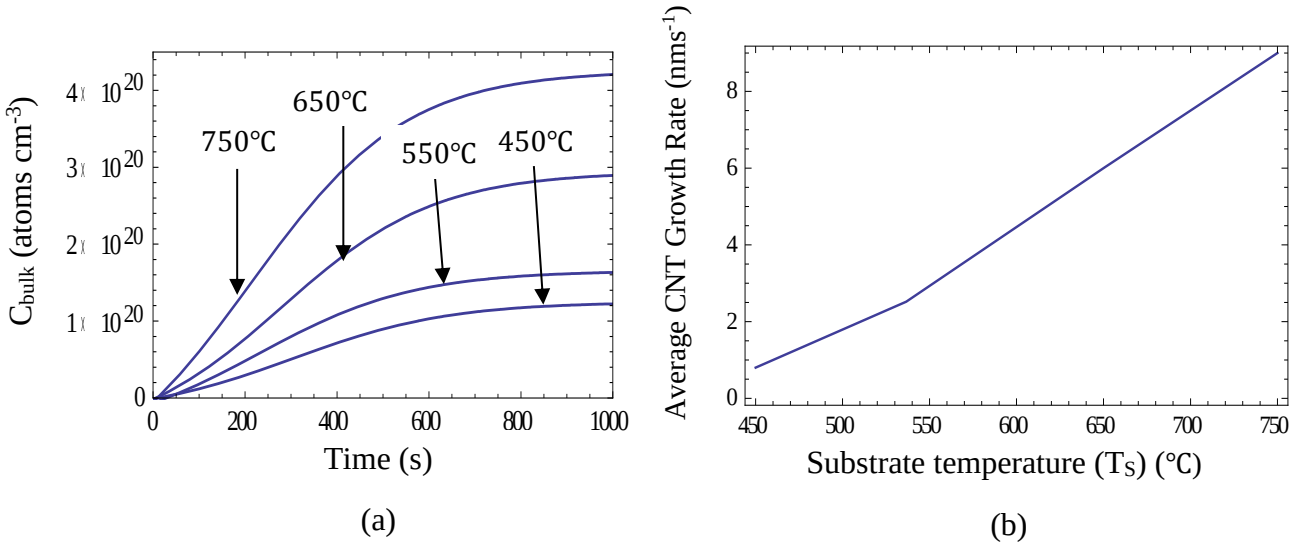

Figure 3.5 (a) Time varying Carbon atom concentration (C_{bulk}) in Ni nanoparticle. (b) Average CNT growth rate with substrate temperature.

3.4.4 Variation of: diffusion length with cooling rate, hydrocarbon density with time in N_2 environment to obtain PGL

The carbon diffusion length inside Ni nanoparticles is explored for graphene precipitation. This is done in the N_2 environment after stopping C_2H_2/NH_3 flow. At a slow cooling rate (5°C/s), the diffusion length is larger than the size of Ni nanoparticles, which leads to Ni completely carburizing and inhibits the formation of graphene [46]. At a rapid cooling rate (25°C/s), a shorter diffusion length is obtained. Therefore, carbon atoms near the Ni surface precipitate more quickly than they diffuse in the Ni bulk, resulting in the formation of amorphous carbon [82]. Figure 6(a) illustrates the effective average diffusion length of carbon into Ni nanoparticle bulk at slow, moderate (15°C/s), and fast cooling rates. The calculated diffusion lengths agree with the results of Gkouzou et al. [46]. According to Yu et al. [26] and Reina et al. [82], the average diffusion length decreases with a rise in cooling rates.

Starting N_2 flow and stopping C_2H_2/NH_3 flow after the formation of the CNT array, causes a gradual decrease for species remaining in the chamber [cf. figure 3.6(b)]. This is explained by the fact that N_2 helps to eliminate volatile byproducts such as HCN, C_2N_2, CN, and volatile hydrocarbons as well as any remaining unreacted precursors [83, 84]. This prevents the catalyst from contamination during the precipitation process. As a result, precipitation processes dominate surface reaction processes in the formation of PGL.

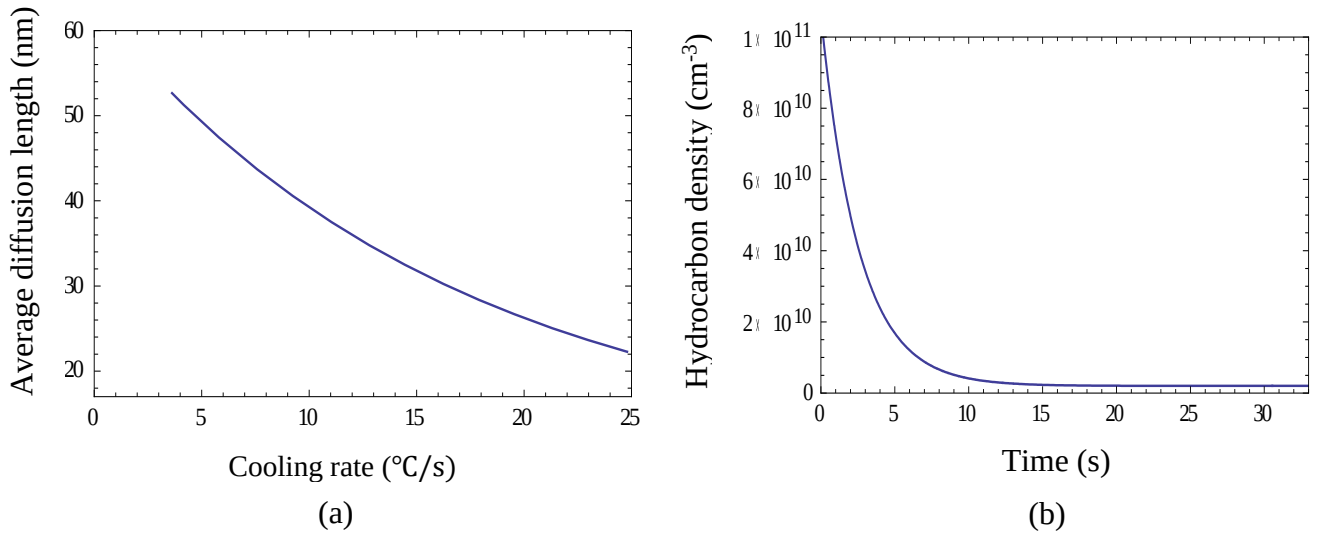

Figure 3.6. (a) Average diffusion length with varying cooling rates (b) Time varying hydrocarbon density

With time as the temperature of the chamber decreases at a rate of 15°C/s, the carbon atoms start precipitating out from the Ni nanoparticle catalyst bulk. The excess carbon atoms that precipitate out to form graphene layers are proportionate to the difference in concentration of the saturated (C_1) and supersaturated (C_0) solution of carbon atoms inside the Ni catalyst [46]. More carbon precipitates out when the temperature drops because the concentration difference between saturated and supersaturated solutions increases and acts as a constant driving force [45, 46].

Consequently, the synthesis of graphene is guided by the outward and surface diffusion of carbon atoms from and on the Ni surface [47, 65, 85]. Therefore, we can depict that the number of graphene layers; hence the thickness of graphene increases with time on cooling [27, 50], [cf. figure 3.7(a)-(b)]. The experimental work of Choi et al. [25] regarding number of graphene layers (4-7 layers), is similar to the obtained value (≈5 layers). Reina et al. [50] have obtained thickness within the range of 1-5nm corresponding to approximately 1-12 graphene layers. Gupta et al. [86] have plotted the thickness of the graphene layer for different values of graphene layer number [cf. figure 1 of Gupta et al. [86]].

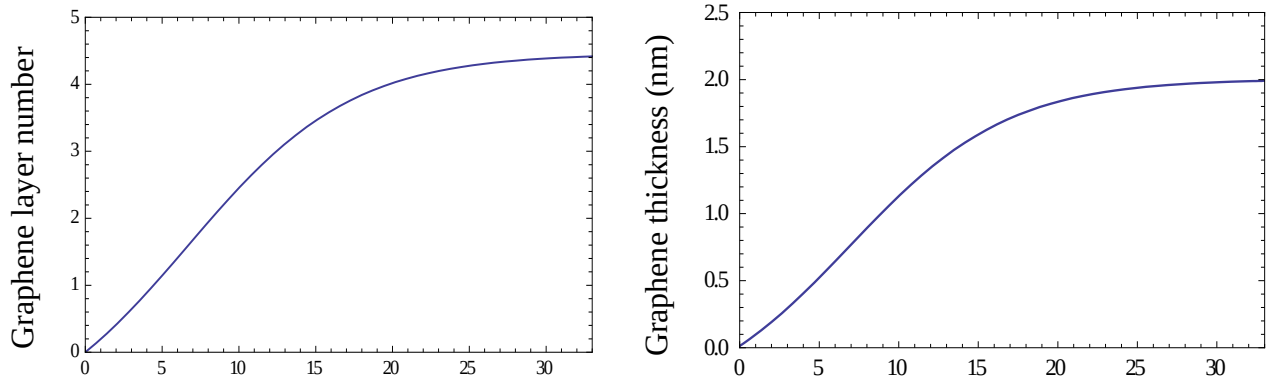

Figure 3.7 (a) Time varying (a) graphene layer number (b) graphene thickness

3.4.5 Variation of graphene layer number with Ni film thickness

At Ni film thicknesses of less than 3 nm, small catalyst nanoparticles form. Carbon

atoms rapidly saturate these catalyst nanoparticles by forming a carbon shell around them [77]. The catalyst nanoparticle size rises with the thickness of the Ni film, causing the CNT array to grow due to increased carbon atom dissolution and diffusion [77]. This simultaneously increases the number of carbon atoms available for precipitation, eventually leading to the formation of graphene layers [47]. Up to a film thickness of 3 nm, figure 3.8 displays no graphene layer; beyond that, the layer number starts to rise with an increase in film thickness. For a 7 nm thick Ni film, Choi et al. [25] got 4–7 graphene layers; Peng et al. [47] and Kim et al. [87], have shown that the number of graphene layers increases with the thickness of the Ni film.

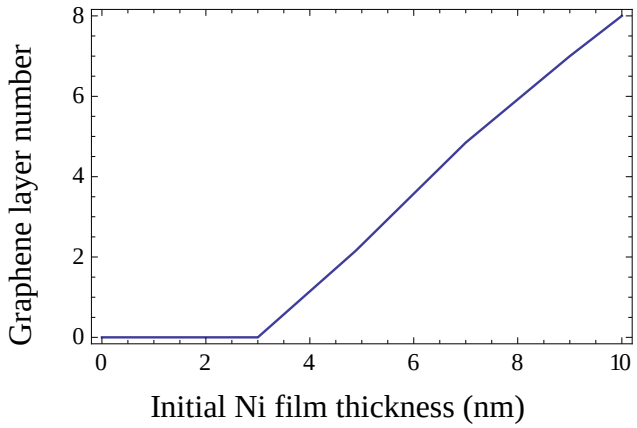

Figure 3.8 Varying graphene layer number with initial Ni film thickness.

3.4.6 Field enhancement factor of CNT array and CNT-PGL hybrid

The procured results from the present study are utilized to determine the field enhancement factor of the CNT-PGL hybrid (β_{hyb}) and to compare it with the field enhancement factor of CNT array (β_a). Table 3.12 lists the dimensions of the CNT array and CNT-PGL hybrid obtained at a C_2H_2 flow rate of 60 sccm, Ni film thickness of 8nm, substrate temperature 750℃, cooling rate 15°C/s.

Table 3.12 Optimized dimensions of CNT array and CNT-PGL hybrid considered

CNT array	CNT –PGL Hybrid
Average height of CNT (L_w) ≈ 5 μm Average diameter of CNT (D_w)≈ 32 nm	Thickness of graphene (t_{pg}) ≈ 2 nm Average height of CNT ≈ 5μm

Spacing among CNT $\approx 1\mu$m	Average diameter of CNT ≈ 32 nm

The obtained β_a [cf. figure 3.9] is consistent with the experimental results of Bonard et al. [32], who got $\beta_a (\approx 800)$ for the following parameters of CNT film: mean height 3μm, mean tube radius 19 nm, and inter-tube distance 1.02μm. Furthermore, it is observed that β_a is less than β_{hyb}. Because CNTs are densely packed, the higher coulomb-repelling force of neighboring CNTs results in a significant reduction of β_a. The large β_{hyb} is ascribed to the field emission from (i) the PGL's edges and (ii) the spaces between CNTs since PGL is present on CNT [87, 88]. Therefore, precipitating PGL across a CNT array considerably increases the field enhancement factor, exceeding βa. Obtained β_{hyb} is following Qu et al. [89] who have obtained $\beta_{hyb} (\approx 5780)$. Kaur et al. [33] [cf. table 2 of Kaur et al. [33]], Hong et al. [34], Kaushik et al. [88] [cf. table 3 of Kaushik et al. [88]] have also reported an escalation in β_{hyb} than β_a.

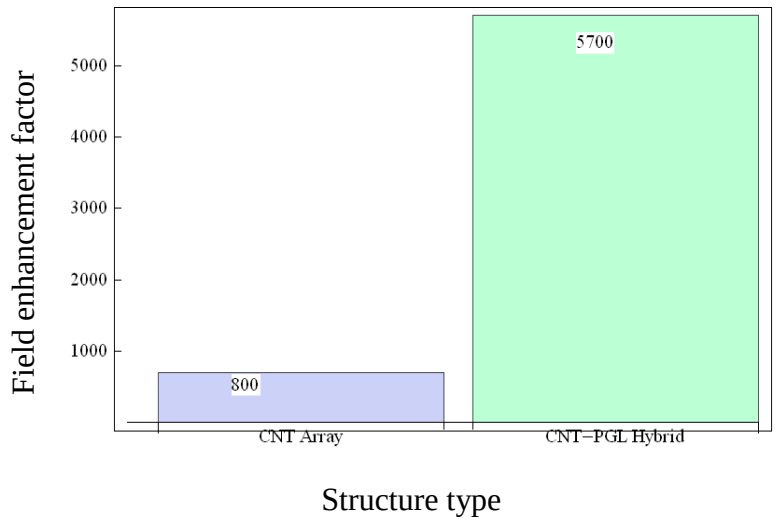

Figure 3.9 Field enhancement factor of CNT array and CNT-PGL Hybrid

3.5 Conclusion

The model can configure and characterize the growth of the CNT-PGL hybrid by adjusting the C_2H_2 flow rate, catalyst film thickness, substrate temperature, and cooling rate. The effect of varying C_2H_2 flow rates on ion and neutral number density, as well as on carbon and hydrogen radical surface concentration is evaluated, to investigate their influence on the growth of the CNT array. It has been noted that as the C_2H_2 flow rate and Ni film thickness increase, the growth rate of the CNT array first increases and subsequently drops. Furthermore, the solubility and diffusivity of carbon atoms inside the Ni catalyst increase with substrate temperature, enhancing the average growth rate of CNTs. Moreover, as chamber temperature decreases at a rate of 15°C/s and catalyst film thickness increases the number of graphene layers grows. The procured results are employed to determine the field enhancement factor of densely packed CNT array and CNT-PGL hybrid and it is concluded that precipitated graphene layers on the CNT array top can enhance the field enhancement factor of the densely packed CNTs. Thus gas flow rate, catalyst film thickness, substrate temperature, and cooling rate may all be regulated to control the formation of a CNT-PGL hybrid, which may then be employed in efficient field emission devices.

References:

1. Sang M, Shin J, Kim K, Yu KJ (2019) Nanomater **9**, 374. https://doi.org/10.3390/nano9030374
2. De Volder MFL, Tawfick SH, Baughman RH, Hart AJ (2013) Science **339**, 535. https://doi.org/10.1126/science.1222453
3. Shim W, Kwon Y, Jeon SY, Yu WR (2015) Sci Rep **5,** 1-10. https://doi.org/10.1038/srep16568
4. Deng JH, Liu RN, Zhang Y, Zhu WX, Han AL, Cheng GA (2017) J Alloys Compd **723**, 75-83. https://doi.org/10.1016/j.jallcom.2017.06.280
5. Gong J, Yang H, Yang P (2015) Compos B Eng **75**, 250-255. https://doi.org/10.1016/j.compositesb.2015.01.035
6. Koh ATT, Chen T, Pan L, Sun Z, Chua DHC (2013) J Appl Phys **113**, 1-5. https://doi.org/10.1063/1.4804238
7. Parmee RJ, Collins CM, Milne WI, Cole MT (2015) Nano Converg **2,** 1-27. https://doi.org/10.1186/s40580-014-0034-2
8. Ji D, Jang J, Park JH, Kim D, Rim YS, Hwang DK, Noh YY (2020) J Inf Disp **22**, 1-11. https://doi.org/10.1080/15980316.2020.1818641
9. Kumar V (2021), Trans Electr Electron Mater **22**, 515-518. https://doi.org/10.1007/s42341-020-00260-6
10. Fang R, Chen K, Yin L, Sun Z, Li F, Cheng HM (2019) Adv Mater **31,** 1800863. https://doi.org/10.1002/adma.201800863
11. Seman RNAR, Azam MS, Mohamad AA (2017) Renew Sustain Energy Rev **75**, 644-659. https://doi.org/10.1016/j.rser.2016.10.078
12. Kumar YA, Koyyada G, Ramachandran T, Kim JH, Sajid S, Moniruzzaman, Alzahmi S, Obaidat IM (2023) Nanomater **13**, 1049. https://doi.org/10.3390/nano13061049
13. Komatsubara K, Suzuki H, Inoue H, Kishibuchi M, Takahashi S, Marui T, Umezawa S, Nakagawa T, Nasu K, Maetani M, Tanaka Y, Yamada M, Hada M, Hayashi Y (2022) ACS Appl Nano Mater **5**, 1521-1532. https://doi.org/10.1021/acsanm.1c04236
14. Ferrier DC, Honeychurch KC (2021) Biosensors-Basel **11**, 486. https://doi.org/10.3390/bios11120486

15. Levchenko I, Xu S, Teel G, Mariotti D, Walker MLR, Keidar M (2018) Nat Commun **9**, 879. https://doi.org/10.1038/s41467-017-02269-7
16. Singh LA, Walker MLR, Sanborn GP, Turano SP, Ready WJ, " Operation of spindt-type, carbon nanotube cold cathodes in a Hall effect thruster environment," paper presented at the 33rd International Electric Propulsion Conference, Washington D.C.,USA, 6-10 October 2013, Paper IEPC-2013-348.
17. Yap YK, Menda J, Vanga LK, Kayastha V, Wang J, King LB, Dimovski S, Gogotsi Y (2004) M.R.S Online Proc Libr **821**, 147-151. https://doi.org/10.1557/PROC-821-P3.7
18. Liu J, Zeng B, Wang X, Wang W, Shi H (2013) Appl Phys Lett **103**, 053105. https://doi.org/10.1063/1.4816751
19. Hong X, Shi W, Zheng H, Liang D (2019) Vacuum **169**, 108917. https://doi.org/10.1016/j.vacuum.2019.108917
20. Neyts EC (2012) J Vac Sci Technol B **30**, 030803. https://doi.org/10.1116/1.3702806
21. Marvi Z, Xu S, Foroutan G, Ostrikov K (2015) Phys Plasmas **22**, 013504. https://doi.org/10.1063/1.4905522
22. Deng JH, Cheng GA, Zheng RT, Yu B, Li GZ, Hou XG, Zhao ML, Li DJ (2014) Carbon **67**, 525-533. https://doi.org/10.1016/j.carbon.2013.10.025
23. Wei YY, Eres G, Merkulov VI, Lowndes DH (2001) Appl Phys Lett **78**, 1394. https://doi.org/10.1063/1.1354658
24. Yesilbag YO, Yesilbag FNT, Huseyin A, Tuzluca M, Ismail I, Ertugrul M (2021) J Mater Sci: Mater Electron **32**, 7943-7955. https://doi.org/10.1007/s10854-021-05519-z
25. Choi JW, Youn SK, Park HG (2013) J Nanomater **2013,** 734686. https://doi.org/10.1155/2013/734686
26. Yu Q, Lian J, Siriponglert S, Li H, Chen YP, Pei SS (2008) Appl Phys Lett **93**, 113103, https://doi.org/10.1063/1.2982585
27. Al- Shurman, KM Naseem H (2014) Excerpt from the Proceedings of the 2014 COMSOL Conference in Boston
28. Lee MW, Haniff MASM, Teh AS, Bein DCS, Chen SK (2015) J Exp Nanosci **10**, 1232-1241. https://doi.org/10.1080/17458080.2014.994679
29. Thapa A, Jungjohann KL, Wang X, Li W (2020) J Mater Sci **55**, 2101-2117. https://doi.org/10.1007/s10853-019-04156-6

30. Chhowalla M, Teo KBK, Ducati C, Rupesinghe NL, Amaratunga GAJ, Ferrari AC, Roy D, Robertson J, Milne WI (2001) J Appl Phys **90**, 10. https://doi.org/10.1063/1.1410322
31. Bell MS, Teo KBK, Lacerda RG, Milne WI, Hash DB, Meyyappan M (2006) Pure Appl Chem **78**, 1117-1125, https://doi.org/10.1351/pac200678061117
32. Bonard JM, Weiss N, Kind H, Stöckli T, Forró L, Kern K, Châtelian A (2001) Adv Mater **13**, 184-188. https://doi.org/10.1002/1521-4095(200102)13:3%3C184::AID-ADMA184%3E3.0.CO;2-I
33. Kaur G, Pulagara NV, Kumar R, Lahiri I (2020) Diam Relat Mater **106**, 107847. https://doi.org/10.1016/j.diamond.2020.107847
34. Mao M, Bogaerts A (2010) J Phys D: Appl Phys **43**, 205201. https://doi.org/10.1088/0022-3727/43/20/205201
35. Bell MS, Lacerda RG, Teo KBK, Rupesinghe NL, Amaratunga GAJ, Milne WI, Chhowalla M (2004) Appl Phy Lett **85**, 1137. https://doi.org/10.1063/1.1782256
36. Gulas M, WDS'07 Proceedings of Contributed Papers, Part III, 123-127, 2007.
37. Cruden BA, Cassell AM, Hash DB, Meyyappan M (2004) J Appl Phys **96**, 5284. https://doi.org/10.1063/1.1779975
38. Mehdipour H, Ostrikov K, Rider AE (2010) Nanotechnology **21**, 455605. https://doi.org/10.1088/0957-4484/21/45/455605
39. Mehdipour H, Ostrikov K, Rider AE, Han Z (2011) Plasma Process Polym **8**, 386-400. https://doi.org/10.1002/ppap.201000150
40. Gupta R, Sharma SC (2020) Plasma Chem Plasma Process 40: 1331-1350, https://doi.org/10.1007/s11090-020-10090-2
41. Cui H, Yang X, Simpson ML, Lowndes DH, Varela M (2004) Appl Phys Lett **84**, 4077. https://doi.org/10.1063/1.1751624
42. Wang XD, Vinodgopal K, Dai GP (2019) Synthesis of carbon nanotubes by catalytic vapor deposition, IntechOpen, https://doi.org/10.5772/intechopen.86995
43. Thapa A, Neupane S, Guo R, Jungjohann KL, Pete D, Li W (2018) Diam Relat Mater **90**, 144-153. https://doi.org/10.1016/j.diamond.2018.10.012
44. McCarty KF, Feibelman PJ, Loginova E, Bartelt NC (2009) Carbon **47**, 1806-1813. https://doi.org/10.1016/j.carbon.2009.03.004

45. Gkouzou A, Janssen GCAM, van Spengen WM, Sens Actuator A: Phys (2020) **303**, 111837. https://doi.org/10.1016/j.sna.2020.111837
46. Peng KJ , Wu CL, Lin YH, Liu YJ, Tsai DP, Pai YH, Lin GR (2013) J Mater Chem C **1**, 3862-3870. https://doi.org/10.1039/C3TC30332B
47. Sodha MS, Misra S, Mishra SK (2009) Phys Plasmas **16**, 123705. https://doi.org/10.1063/1.3273073
48. Ostrikov K, Xu S, Plasma-Aided Nanofabrication From Plasma Sources to Nanoassembly, Wiley Publishers Since 1807, https://download.e-bookshelf.de/download/0000/6030/70/L-G-0000603070-0002364804.pdf
49. Reina A, Jia X, Ho J, Nezich D, Son H, Bulovic V, Dresselhaus MS, Kong J (2009) Nano Lett **9**, 30-35. https://doi.org/10.1021/nl801827v
50. Liu H, Liu Y (2017) Phys Sci Rev **2**, 20160107. https://doi.org/10.1515/psr-2016-0107
51. John and Marica Price College of Engineering, The University of Utah, Department of Material Science and Engineering, The Zang Research Group, lecture-4.pdf, last modified: 2023-01-19. Available Online https://my.eng.utah.edu/~lzang/images/lecture-4.pdf (accessed on 14 April.2024)
52. Fang, W. (2012). "Bilayer graphene growth by low pressure chemical vapor deposition on copper foil "(Doctoral dissertation, Massachusetts Institute of Technology).
53. Gupta R, Sharma SC, Sharma R (2017) Plasma Source Sci. Technol. **26**, 024006. https://doi.org/10.1088/1361-6595/aa5120
54. Sodha MS, Misra S, Mishra SK, Srivastava S (2010) J Appl Phys **107**, 103307. https://doi.org/10.1063/1.3410676
55. Gupta R, Gupta N, Sharma SC (2018) Phys Plasmas **25**, 043504. https://doi.org/10.1063/1.5020561
56. Trott M, 3D Charges and Configurations with sharp edges (September 27,2012) Wolfram Available Online https://blog.wolfram.com/2012/09/27/3d-charges-and-configurations-with-sharp-edges/ (accessed on 14 April 2024)
57. Denysenko IB, Xu S, Long JD, Rutkevych PP, Azarenkov NA, Ostrikov K (2004) J Appl Phys **95**, 2713. https://doi.org/10.1063/1.1642762
58. Carrasco E, Redondo MJ, Tanarro I, Herrero VJ, (2011) Phys Chem Chem Phys 13, 19561-19572. https://doi.org/10.1039/C1CP22284H

59. Alman DA, Ruzic DN, Brooks JN, (2000) Phys Plasmas **7**, 1421. https://doi.org/10.1063/1.873960
60. The UMIST database for astrochemistry 2012
See http://www.udfa.net/ for database of neutral-ion reactions rate coefficients
61. A. M. da Cruz Baptista Dias, Modeling of Low Pressure Plasmas in CH4-H2 Mixtures (Instituto Superior Tecnico, Universidade de Lisboa, 2012).
62. Gupta R, Sharma SC (2018) Contrib Plasma Phys **59**, 72-85. https://doi.org/10.1002/ctpp.201700138
63. Li J (2014) Thesis "Theoretical Investigations of Catalytic Methane Cracking and Carbon Nanotube Growth". UWSpace. Available Online https://uwspace.uwaterloo.ca/bitstream/handle/10012/8629/N_Li_Jingde.pdf?sequence=1&isAllowed=y (accessed on 14 April 2024)
64. Sharma S, Sharma SC (2022) Plasma Chem Plasma Process **42**, 413-433. https://doi.org/10.1007/s11090-022-10229-3
65. Liu N, Fu L, Dai B, Yan K, Liu X, Zhao R, Zhang Y, Liu Z (2011) Nano Lett **11**, 297-303. https://doi.org/10.1021/nl103962a
66. Lv S, Li Z, Liao J, Wang G, Li M, Miao W (2015) Sci Rep **5**, 15035. https://doi.org/10.1038/srep15035
67. Milovzorov DE (2018) 'Local Electric Fields in Dielectric and Semiconductors', in M. S. Kandelousi (ed.), Electric Field, IntechOpen, London. https://doi.org/10.5772/intechopen.74310.
68. Kim TS, An YJ, Kim KH, Chung WS, Cho YR (2006) Met Mater Int **12**, 339-343. https://doi.org/10.1007/BF03027551
69. Santos EJG, Kaxiras E (2013) Nano Lett **13**, 898-902. https://doi.org/10.1021/nl303611v
70. Murata H , Nakajima Y, Saitoh N, Yoshizawa N, Suemasu T, Toko K (2019) Sci Rep **9**, 4068. https://doi.org/10.1021/nl303611v
71. Liu X, Wang CZ, Hupalo M, Lin HQ, Ho KM, Tringides MC (2013) Crystals **3**, 79-111. https://doi.org/10.3390/cryst3010079
72. Hash D, Bose D, Govindan TR, Meyyappan M, (2003),J. Appl. Phys. **93**, 6284. https://doi.org/10.1063/1.1568155

73. Teo KBK, Hash DB, Lacerda RG, Rupesinghe NL, Bell MS, Dalal SH, Bose D, Govindan TR, Cruden BA, Chhowalla M, Amaratunga GAJ, Meyyappan M, Milne WI, (2004) Nano Lett **4**,921–926. https://doi.org/10.1021/nl049629g
74. Mao M, Bogaerts A (2010) J.Phys.D: Appl. Physs. **43**, 315203. https://doi.org/10.1088/0022-3727/43/31/315203
75. Merkulov VI, Hensly DK, Melechko AV, Guillorn MA, Lowndes DH, Simpson ML (2002) J Phys Chem B **106**, 10570-10577. https://doi.org/10.1021/jp025647f
76. Lee MW, Haniff MASM, Teh AS, Bien DCS, Chen SK, Talib ZA, Shaari AH (2015) Adv Mater Res **1107**, 314-319. https://doi.org/10.4028/www.scientific.net/AMR.1107.314
77. Han JH, Kim HJ, Yang MH, Yang CW, Yoo JB, Park CY, Song YH, Nam KS (2001) Mater Sci Eng C **16**, 65-68. https://doi.org/10.1016/S0928-4931(01)00277-6
78. Ma W, Zhou Z, Li G, Li P (2016) High Temp Mater Proc **35**, 857-863. https://doi.org/10.1515/htmp-2015-0084
79. Baraton L, He ZB, Lee CS, Cojocaru CS, Châtelet M, Maurice JL, Lee YH, Pribat D (2011) EPL **96**, 46003. https://doi.org/10.1209/0295-5075/96/46003
80. Bleu Y, Barnier V, Christien F, Bourquard F, Loir AS, Garelie F, Donnet C (2019) Carbon **155**, 410-420. https://doi.org/10.1016/j.carbon.2019.08.084
81. Reina A, Thiele S, Jia X, Bhaviripudi S, Dresselhaus MS, Schaefer JA, Kong J (2009) Nano Res **2**, 509-516. https://doi.org/10.1007/s12274-009-9059-y
82. Wilson RL (2017) "Deposition of ultra-thin metal oxide films for gas sensing applications". Doctoral thesis (Ph.D), UCL (University College London).
83. Schlüter M, Hopf C, Jacob W (2008) New J Phys **10**, 053037. https://doi.org/10.1088/1367-2630/10/5/053037
84. Weatherup RS, Bayer BC, Blume R, Baehtz C, Kidambi PR, Fouquet M, Wirth CT, Schlögl R, Hofmann S (2012) ChemPhysChem **13**, 2544-2549. https://doi.org/10.1002/cphc.201101020
85. Gupta A, Chen G, Joshi P, Tadigadapa S, Eklund PC (2006) Nano Lett.**6,** 2667-2673. https://doi.org/10.1021/nl061420a
86. Kim KS, Zhao Y, Jang H, Lee SY, Kim JM, Kim KS, Ahn JH, Kim P, Choi JY, Hong BH (2009) Nature **457**, 706–710. https://doi.org/10.1038/nature07719

87. Kaushik V, Shukla AK, Vankar VD (2014) Appl Phys A **117**, 2197-2205. https://doi.org/10.1007/s00339-014-8646-2
88. Qu K, Zhang X, Zhang Y, Li C, Cole MT, Zhao N, Shi C, Ding S, Ying K, Lie W, Wang B, Milne WI (2013) IEEE 14th International Vacuum Electronics Conference (IVEC), 2013, pp.1-2.

Chapter 4

Effect of H_2 flow and catalyst film thickness on the growth of CNT-G hybrid.

- **Numerical analysis on H_2 plasma assisted growth of graphitic leaves on carbon nanotubes**
- **Optimizing the Cobalt film thickness for the growth of carbon nanotube with few layer graphene foliates**

4.1 Brief outline

Numerical conceptual design explaining the growth of graphitic leaves over carbon nanotube (CNT) in C_xH_y/ H_2 and CH_4/ Ar plasma environment employing PECVD technique is evolved. Growth of linear defect density (investigated via energy balance equation over CNT), CNT, graphitic leaves is explored by varying input plasma power (600-1200W). The results indicate drop in defect density, growth rate of CNT and graphitic leaves with rising plasma power. In addition, catalyst film thickness is varied to investigate the morphology of carbon nanostructure. It is found that the growth rate of few layer graphene (FLG) increases with Co film thickness and switches to FLG grown on CNT morphology, with further increase in catalyst film thickness. Growth of FLG on CNT is defect mediated. Also, field enhancement (FE) factor is computed for different morphologies obtained. An enhancement in FE factor is observed for CNT with FLG foliates in comparison to bare FLG. Our theoretical results are in agreement with the experimental observations.

4.2 Introduction

Graphenated Carbon Nanotubes synthesized using solution process, electric arc discharge, CVD, PECVD are a beginning to hybrid having exfoliated graphene framing carbon nanotubes. This 3D material is promising in wide range of applications but not limited to field emitters, electrodes for lithium ion batteries, transparent conductors.

Deng et al. [1] experimentally grew CNT- graphene hybrid by varying C_2H_2 gas ratio, plasma power, and growth time and showed that each parameter influences the hybrid's growth.

Liu et al. [2] experiment validate that growth of graphene over CNT is defect mediated, wherein defects are due to high- energy ion bombardments and further lengthening by epitaxial mechanism.

Lee et al. [3] have shown that the Co and Ni catalyst thickness has a significant impact on both nanotube diameter and growth rate, as well as the morphology of nanoparticles generated during the process, without affecting CNT quality.

Qi et al. [4] experimentally shown that V-FLG growth and morphology are heavily influenced by the Co catalyst and its film thickness. V-FLG demonstrated slower growth rate and poorer density on substrates without catalyst than with catalyst, since the V-FLG nucleation on the former was delayed.

4.3 Model

Examining the buildup of graphenated carbon nanotubes in electron, positively charged ions, and neutrals of C_xH_y (denoted as 1), H_2 (denoted as 2) plasma and in electron, positively charged ions and neutrals of CH_4 (denoted as 1) , Ar (denoted as 2). Ionization of gas by applied RF power creates the plasma species (hydrocarbon, hydrogen- radicals, neutrals, ions) of relatively high energy. Electric field from the plasma to the CNT plane due to hydrocarbon, hydrogen, argon ions results in, high energetic ions bombarding CNT surface, breaking some C-C bonds, creating dangling bonds defects on the CNT surface [5-6]. Vertical graphene sheet grow upon CNT via these defects (nucleation sites), wherein carbon atoms nucleate to carbon aggregate which further diffuse and collide to form graphene islands [7-8]. Then under the resultant of tensile and electrostatic force vertical graphene sheet grow as leaf over CNT [9]. Hydrocarbons (formed by the reaction of CNTs with hydrogen plasma) promote graphene growth.

4.3.1 Growth rate equation of carbon species over catalyst surface

Due to adsorption of hydrocarbon, thermal dissociation of adsorbed hydrocarbons, hydrocarbon ion decomposition and various other process carbon species are generated on the catalyst surface and is expressed via equation 1.

$$\dot{S_C} = \sum_a J_a\left(1-\theta_t\right)+\sum_a n_{sa}\omega\exp\left(\frac{-\delta E_{td}}{k_B T_S}\right)+\sum_{ia}\left(\sum_a \frac{n_{sa}Y_d}{\upsilon_o}\right)J_{ia} + \sum_{ia} J_{ia}+\sum_{ib}\left(\sum_{ia}\frac{J_{ia}\sigma_{ads}}{\omega}\right)J_{ib} - S_C\omega\exp\left(\frac{-E_{evp}}{k_B T_S}\right) - \Gamma_C \qquad (1)$$

Where the first, second, third, fourth, fifth term represents gain due to adsorption of hydrocarbon, thermal dissociation of adsorbed hydrocarbon, ion- induced dissociation of adsorbed hydrocarbon, hydrocarbon ion decomposition, hydrocarbon and hydrogen ion interaction on catalyst surface and loss due to carbon evaporation and carbon flux leaving the catalyst surface.

$\delta E_{td}\ (= 2.1eV), E_{evp}\ (= 1.8\ eV)$ are the hydrocarbon thermal dissociation energy, carbon evaporation energy [10]. $n_{sk}(= \theta_k\vartheta_0), \omega\ (\approx 10^{13}Hz), Y_d\ (\approx 2.49 \times 10^{-2} + 3.29 \times 10^{-2} \times E_i)$ are the surface concentration of neutral species, thermal vibration frequency, stitching probability. $\sigma_{ads}(\approx 10^{-16}cm^2)$ and $\upsilon_0\ (\approx 10^{15}cm^{-2})$ are cross section of reaction with atomic hydrogen and area density of adsorption sites.

4.3.2 Growth rate equation of CNT

The average growth rate of CNT is assessed by the change in the volume of CNT of diameter D_w and height L_w.

$$\pi \frac{d\left(R_w^2 H_w\right)}{dt} = \left[\begin{array}{l} \left(\begin{array}{l} \frac{D_d R_w}{f} \exp\left(\frac{-Xvoc}{k_B T_s} \right) + \\ \frac{D_e}{f} \exp\left(\frac{-X_{arc}}{k_B T_s} \right) + \\ \frac{B_s R_w}{f} \exp\left(\frac{-\delta X_{INc}}{k_B T_s} \right) + \\ \frac{D_f}{f} \exp\left(\frac{-X_{arcl}}{k_B T_s} \right) \end{array} \right) \times \left(S_C \times \xi_{ij} \times \left(\frac{M_{cy}}{\rho_{cy}} \right)_w \right) + \\ \left(\left[\pi R_w H_w \times H_a \times \xi_{ik} \times \left(\frac{M_{ct}}{\rho_{ct}} \right)_w \right] + \left[\left(\Upsilon_j \xi_j + \Upsilon_l \xi_l \right) \times \left(\frac{M_{cy}}{\rho_{cy}} \right)_w \right] \right) \end{array} \right], \quad (2)$$

Where the first, second, third and fourth terms in equation 2 represents growth due to : bulk diffusion of carbon monomer into catalyst nanoparticle, diffusion of carbon monomer over surface of catalyst nanoparticle, diffusion of carbon cluster over surface of catalyst nanoparticle and incorporation of carbon monomer into CNT through CNT - catalyst confluence. Etching of amorphous carbon over the catalyst nanoparticle surface and accumulation of neutrals of type j and l throughout the surface of CNT which also assist in growth is represented by the fifth and sixth terms.

X_{voc} = (1.6 eV), X_{arc} = (0.3 eV), X_{INc} = (0.48 eV) and X_{arcl} = (0.4 eV) are the energy barriers for: bulk diffusion in catalyst nanoparticle, surface diffusion of carbon monomer over catalyst surface, surface diffusion of carbon clusters over catalyst surface and for incorporation along CNT- catalyst interface [11-12]. D_d and D_e, D_f are the bulk diffusion coefficients and surface diffusion coefficients. B_s is the incorporation speed of carbon monomer into CNT. M_{cy} (≈12g) and ρ_{cy} are mass and density of CNT.

4.3.3 Generation of defects on CNT surface

Growth rate equation of defects on CNT surface under ion irradiation of hydrocarbon and hydrogen is described as:

$$P = \rho_{cy} V S_c T_s \frac{1}{d}\frac{\partial d}{\partial t} = \left[\sum_{m}^{1,2}\left[\left[\left(\varsigma_{im}^{cur} + \varsigma_{im}^{tip}\right)\epsilon_{im}^{c}\right] + \left[\left(\varsigma_{m}^{cur} + \varsigma_{m}^{tip}\right)\epsilon_{k}^{c}\right]\right] + \left(\varsigma_{e}^{cur} + \varsigma_{e}^{tip}\right)\epsilon_{e}^{c}\right] + \left[\frac{3}{2}k_B T_s \sum_{m}^{1,2}\left(1-\psi_{im}\right)\left(\varsigma_{ik}^{cur} + \varsigma_{ik}^{tip}\right)\right] + \left[\left(\upsilon_o \sigma_{ads} F_b E\right) A_c\right] + \left[\left(\sum_{m}^{1,2} F_{im} Y\left(E_i\right)\left(1-\theta_n\right) A_c\right)\right] - A_{Cy}\sigma\varepsilon\left(T_s - T_a\right) \quad (3)$$

Where the first, second and third term in equation 3 represents formation of defects on CNT surface owing to power transferred : due to its interaction with positively charged ions, neutrals, and electrons, due to neutralization of ions collected at the CNT surface and due to etching of the CNT surface. Fourth term represent power transferred due to ion sputtering. Energy loss from the surface to surroundings is represented by fifth term.

ρ_{cy}, S_C, T_s and d denotes the density of CNT, specific heat of CNT, substrate temperature and defect density. ς_k and ϵ_k denotes collection current and average energy accumulated on CNT surface due to ions (type 1 and 2), neutrals (type 1 and 2) and electrons. F_b and F_{im} denotes flux of impinging neutrals and ions on CNT surface. Y(E_i) and E denotes sputtering yield and surface binding energy of carbon in CNT. $\theta_n (\approx 0.01)$ represents total surface coverage. A_{cy} and T_a denotes area of CNT and ambient temperature.

4.3.4 Graphitic leaf growth equation

Equation 4 describes the growth processes involved in graphitic leaf growth of length L, thickness T, and Height H. Carbon atoms diffuse and incorporate at the surface and peripherals of the growing graphene sheet along with their etching by hydrogen atoms from the plasma. Graphene sheet growth is defect mediated.

$$L\frac{d\left[(T\times H)\right]}{dt}=$$

$$\left[\frac{S_C}{\nu}Dexp\left(\frac{-\left(E_{sc}+E_{Inc}\right)}{k_BT_s}\right)\times\varsigma_{i1}^{g}+(\eta_1\varsigma_1^{g})\times(A_D\,2\pi R)+\left(\left[\left(\psi_{i2}\varsigma_{i2}^{g}+\psi_2\varsigma_2^{g}\right)\times\left(2\pi R\times 2\pi R_D\right)\times H_a\right]\right)\right]\left(\frac{m}{\rho}\right) \quad (4)$$

Where surface diffusion and incorporation of carbon atoms at the surface and peripherals of the growing vertical graphene (VG) sheet is described via first term. Second term represents sticking of neutral atom of type 1 at the graphene sheet. Third term is etching of terminal carbon at the edges of the VG sheet by interaction with hydrogen atoms from the plasma assisting in clean graphene growth.

$E_{SC} \approx 0.1$ eV, $E_{INC} \approx 0.42$ eV are the energy barriers for surface diffusion of carbon monomer and incorporation of carbon monomer [13]. A_D, R_D, R denotes area, radius of defect, radius of graphene island. m, ρ denotes mass and density of graphene sheet. ς_k^g denotes collection current on graphene sheet due to ions (type 1 and 2), neutrals (type 2). H_a represents hydrogen surface concentration.

4.4 Results and discussion

The equations listed above are solved simultaneously with those described in our prior work for the energy balance and kinetics of electrons, ions, and neutrals under appropriate boundary conditions viz., at , t=0, $n_{i10} = 6\times10^{18}cm^{-3}$, $n_{i20} = 5\times10^{7}cm^{-3}$, $n_{10} = 1\times10^{12}cm^{-3}$, $n_{20} = 1\times10^{13}cm^{-3}$, Substrate temperature (T_s) = 900℃, Plasma pressure = 60 Torr, Plasma Power = 600- 1200 W.

For plasma environment **I:** C_xH_y + H_2, temporal variations of CNT height, linear defect density, graphene sheet height for different input plasma powers.

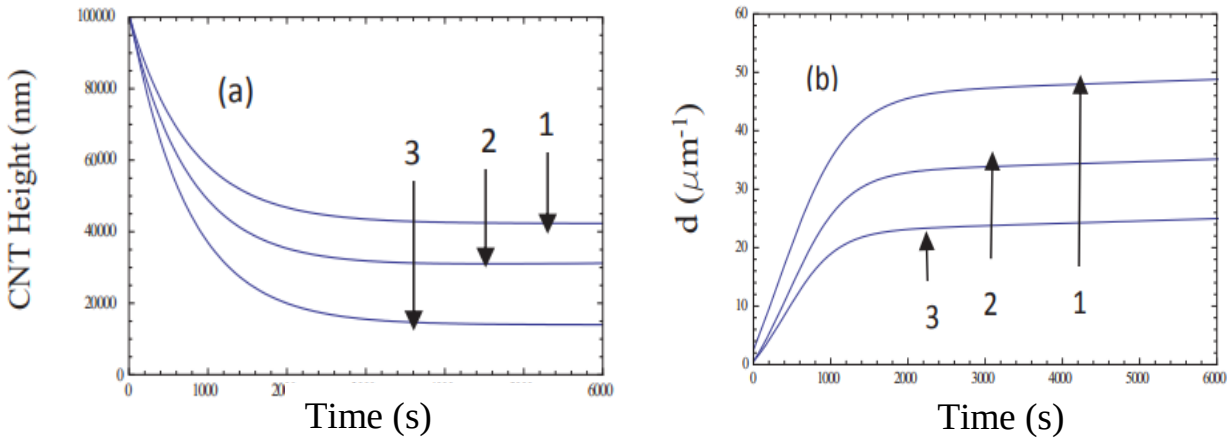

Figure 4.1 Time variation of (a) CNT height (b) linear defect density for different input plasma power (1=600W), (2=900W), (3= 1200 W)

Figure 4.1 (a) shows temporal variation of CNT height for different input plasma power. Increase in input plasma power rises hydrogen etchant density and plasma power of hydrogen etchant. As a result, height of CNT drops due to less availability of carbon on surface for growth, following a study conducted by Gorodetskiy et al. [14].

Figure 4.1 (b) represents time varying linear defect density on CNT with input plasma power. Number of defects on CNT surface decreases with increase of input plasma power following a study conducted by Gorodetskiy et al. because no. of defect is a function of no. of carbon away from the catalyst surface, carbon surface concentration decreases with rise in power as discussed above. In addition, their exist proportionality between defect amount and CNT length.

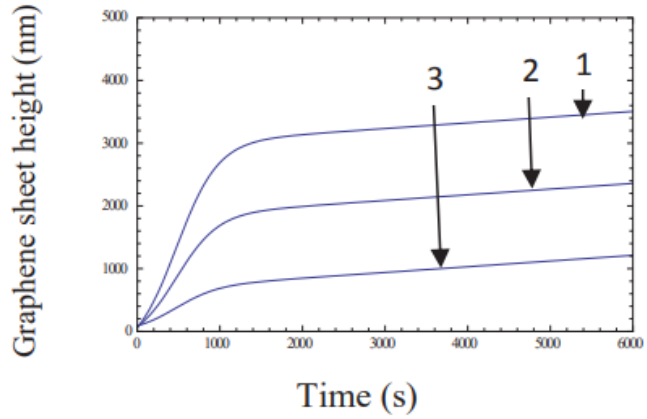

Figure 4.2 Time variation of graphene sheet height for different input plasma power (1=600W), (2=900W), (3= 1200 W)

Figure 4.2 represents rate of change of height of graphene sheet with input plasma power. Increase of plasma power leads to etching of growing graphene sheet owing to rise in hydrogen density and plasma power of etchant. Consequently, growth rate (height) of graphene sheet decreases with increase of plasma power, comply with the observations of Gorodetskiy et al. [14].

For plasma environment **II:** CH_4 + Ar, temporal variations of : surface carbon concentration, CNT height, graphene height for different catalyst film thickness.

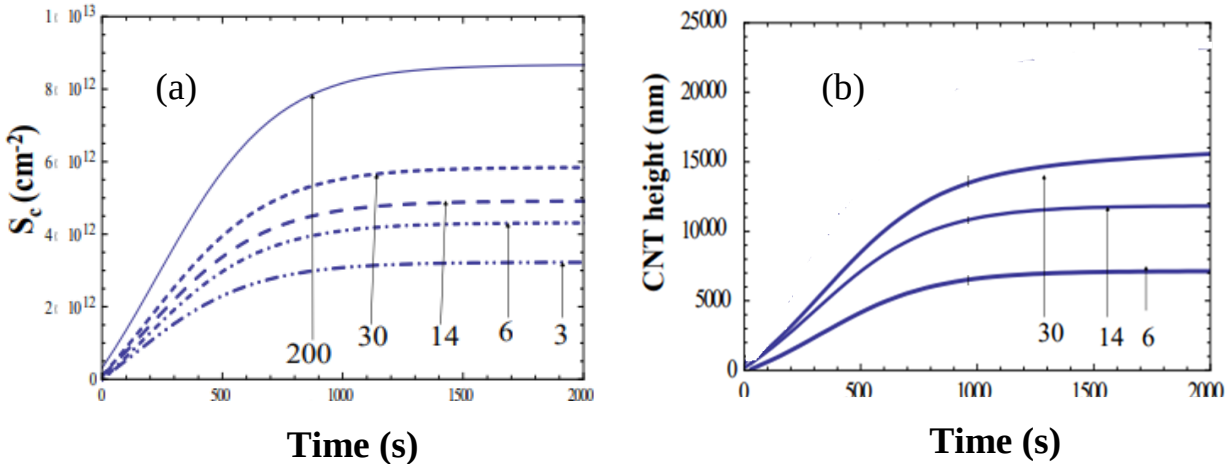

Figure 4.3 Temporal variation of (a) surface carbon concentration (b) CNT height for different catalyst film thickness (nm).

Figure 4.3 (a) represents surface carbon concentration for different catalyst film thickness. With increase of nanofilm thickness, size of nanoparticle increase which lead to increase in surface area for hydrocarbon dissociation on catalyst surface. Thus a large number of carbon species generate on catalyst surface in compliance with the work of Qi et al. [4].

Figure 4.3 (b) represents CNT height for different catalyst film thickness. Small catalyst nanoparticles are less proficient to encourage CNT growth due to amorphous carbon deposition leading to growth of small graphene flakes only and no CNT for 3 nm film thickness. With further increase of catalyst film thickness (upto 30 nm) CNT height increases. Large Co catalyst particles are not suitable for growth of CNTs, and the graphite layer will cover the large Co particle surface to form graphite shell-encapsulated Co particles. In compliance with the work of Qi et al. [4].

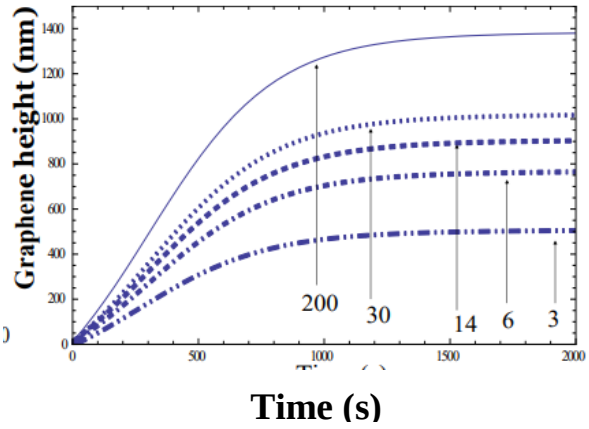

Figure 4.4 Temporal variation of graphene height for different catalyst film thickness

Figure 4.4 represents graphene height for different catalyst film thickness. With the increase of nanofilm thickness, size of nanoparticle increases, thus a large number of carbon species generate at catalyst surface and precipitate out through catalyst bulk. Thus graphene height increase with increase of catalyst film thickness. In compliance with the work of Qi et al.[4].

4.5 Conclusions

A model is developed to better understand the effects of plasma power and Co film thickness on CNT and graphene height. The findings show that when plasma power increases, CNT height, defect density, and graphene height decrease. With plasma power, hydrogen density rises, supporting the drop in CNT and graphene height. Furthermore, as plasma power increases, the height of the CNT lowers, reducing defect density on the CNT surface. We also investigated the influence of Co catalyst film thickness on the growth of CNT and graphene. The study found that carbon surface concentrations rise with Co film thickness, resulting in graphite shell-encapsulated Co particles that inhibit CNT formation on thick Co films. In addition, the height of the graphene sheet grows with the thickness of the Co film. The findings can be used to gain a better understanding of the formation of CNT-decorated graphene in plasma and to investigate field emission applications.

References:

1. Deng JH, Cheng GA, Zheng RT, Yu B, Li GZ, Hou XG, Zhao ML, Li DJ (2014), Carbon **67**, 525-533. https://doi.org/10.1016/j.carbon.2013.10.025
2. Liu J, Zeng B, Wang X, Wang W, Shi H (2013), Appl Phys Lett **103**, 1-4 https://doi.org/10.1063/1.4816751
3. Lee MW, Haniff MASM, The AS, Bien DCS, Chen SK (2015), J Exp Nanosci **10**, 1232-1241, https://doi.org/10.1080/17458080.2014.994679
4. Qi JL, Zhang F, Wang X, Zhang LX, Cao J, Feng JC (2014), RSC Adv. **4,** 44434-44441. https://doi.org/10.1039/C4RA08109A
5. Gautier LA, Borgne VL, Khakani MAE, (2016), Carbon **98**, 259-266. https://doi.org/10.1016/j.carbon.2015.11.006
6. Zeng L, Lei D, Wang W, Liang J, Wang Z, Yao N, Zhang B, (2008), Appl Surf Sci **254,** 1700-1704. https://doi.org/10.1016/j.apsusc.2007.07.131
7. Wang BB, Zhu K, Ostrikov K, Shao RW, K. Zheng K, (2016), J Appl Phys, **119**, 1-7.
8. Mehdipour H, Ostrikov K, (2012), ACS Nano, **6**, 10276-10286. https://doi.org/10.1021/nn3041446
9. Wang BB, Zheng K, Cheng QJ, Ostrikov K, (2015), Appl Surf Sci **325**, 251-257. https://doi.org/10.1016/j.apsusc.2014.11.072
10. Marvi Z, Xu S, Foroutan G, Ostrikov K (2015) Phys Plasmas **22**, 013504. http://dx.doi.org/10.1063/1.4905522
11. Gupta R, Sharma SC (2018) Contrib Plasma Phys **59**, 72-85. https://doi.org/10.1002/ctpp.201700138
12. Li J (2014) Thesis "Theoretical Investigations of Catalytic Methane Cracking and Carbon Nanotube Growth". UWSpace. Available Online https://uwspace.uwaterloo.ca/bitstream/handle/10012/8629/N_Li_Jingde.pdf?sequence=1&isAllowed=y (accessed on 14 April 2024)
13. Mehdipour H, Ostrikov K (2012) ACS Nano **6**. 10276-10286. https://doi.org/10.1021/nn3041446
14. Gautier LA, Borgne VL, Khakani MAE, (2016), Carbon **98**, 259-266, https://doi.org/10.1016/j.carbon.2015.11.006

Chapter – 5
SUMMARY AND FUTURE SCOPE OF THE WORK

5.1 Summary

The current thesis seeks to develop an analytical model to understand the mechanisms of CNT-graphene hybrid growth in a reactive plasma environment. A theoretical and analytical model is developed that incorporates the plasma sheath equations , the energy and fluxes of the plasma species, (electrons, positively charged and neutral species), kinetics of the plasma species, dissociation of the plasma species over the catalyst nano particle surface to generate building units (carbon species). The diffusion of building units leads to formation of carbon clusters and growth of CNT with graphene leaves on top, which eventually grow vertically in the presence of an electric field created in the plasma sheath. The present study of the thesis may contribute to a better understanding of the effects of plasma parameters, optimum conditions, and Co film thickness on the growth properties of the CNT-graphene hybrid. The hybrid's field emission characteristics are estimated using the results acquired in this study. In brief, the work done in the current thesis can be summarized as follows.

The effect of total gas pressure (250 mTorr–5 Torr) and input plasma power (300–700 W) on the growth attributes of the N-NCN-VG hybrid, such as height, thickness, and number density of carbon, as well as the kinetics of plasma species, such as electrons, positive ions, and neutrals, is investigated in C_2H_2/NH_3 plasma. Furthermore, the model explains how the creation of defects on the nanocone causes the VG sheet to grow. Our theoretical studies reveal that as total gas pressure increases and input plasma power decreases the height of the nanocone and graphene sheet increases, simultaneously with rise in carbon number density on the nanocone surface. Furthermore, when input power increases, the N-NCNVG hybrid’s field enhancement factor falls.

When dense CNT arrays and planar graphene layers were utilized as field emitters, the field enhancement factor decreased considerably. As a result, we quantitatively examine the evolution of a dense CNT array topped with planar graphene layers (PGLs), yielding a CNT-PGL hybrid and the corresponding field enhancement

factor. The growth of the CNT array is studied in a C_2H_2/NH_3 environment with variable C_2H_2 flow, Ni catalyst film thickness, and substrate temperature, followed by PGL precipitation on top at an optimal cooling rate and Ni film thickness. Our research indicates that when the catalyst film thickness and C_2H_2 flow rate increase, the average growth rate of CNTs first rises and subsequently falls. As the temperature of the substrate rises, CNT growth rate increases. Moreover, the number of graphene layers increases as the chamber temperature is dropped from 750°C to 250°C in a N_2 environment and the thickness of the Ni film increases. The ideal parameter values are then used to determine the field enhancement factors for the hybrid and CNT array. It has been discovered that by covering densely packed CNTs with planar graphene layers, can increase the field enhancement factor.

To have a better understanding of how Co film thickness and plasma power affect CNT and graphene height, a model is developed. The results demonstrate that CNT height, defect density, and graphene height decrease with increasing plasma power. We also looked into how the thickness of the Co catalyst sheet affected the growth of graphene and CNT. According to the findings, thicker Co films prevent CNT production because higher carbon surface concentrations lead to graphite-shell-encapsulated Co particles. Furthermore, as the thickness of the Co film increases, so does the height of the graphene sheet. The results can be applied to field emission applications and to better understand the formation of CNT-decorated graphene hybrid in plasma.

5.2 Future scope of the present work

The present work of the thesis can be extended to fabricate CNT- graphene hybrid for their potential applications in the field emitters as the field emission characteristics of the CNT- graphene hybrid depend on its geometrical characteristics, i.e., height and thickness.

The present work covers most of the important aspects for the deterministically controlled synthesis of the hybrid in plasma. However, there are some aspects which can be deepen further for the future development of the synthesis of the hybrid.

Nonetheless, many aspects concerning plasma-assisted CNT development remain unexplored experimentally and conceptually, which has the potential to broaden our understanding of this field. Some of the recommendations for future work that needs to be done are:

- The temperature of the CNT-G hybrid surface is assumed to remain constant and equal to that of the catalyst surface during the growing process. However, examinations into the temperature of the hybrid's surface are required to analyse its effect on the hybrid growth.

- It is essential to comprehend the impact of catalyst-substrate interactions on hybrid development in a reactive plasma. As the research has shown, the development of hybrids requires the presence of a catalyst. As a result of the catalyst and substrate interacting, it can be observed at the tip of fully-grown CNTs or at the base of the CNT, anchored to the substrate. The relationship between the catalyst and the substrate has not been fully examined and require more research.

Appendix: Potential at curved surface of w[th] CNT (V_{cur}) [1]

$$V_{cur} = \frac{\rho_q}{4\pi\varepsilon_\circ} \iiint \frac{1}{\sqrt{(x'^2+y'^2+(z-z')^2}} d\tau'$$

$$x' = r'\cos\varphi', y' = r'\sin\varphi', z = z'$$

$$\frac{\rho_q}{4\pi\varepsilon_\circ} \int_{-L_w/2}^{L_w/2} \int_0^{2\pi} \int_0^{R_w} \frac{1}{\sqrt{((r'\cos\varphi)'^2+(r\sin\varphi)'^2+(z-z')^2}} r'dr'd\varphi'dz'$$

where ρ_q is charg density on curved surface of w[th] CNT, R_w is the radius of w[th] CNT.

$$\frac{\rho_q}{4\pi\varepsilon_\circ} \int_{-L_w/2}^{L_w/2} \int_0^{2\pi} [\int_0^{R_w} \frac{r'}{\sqrt{r'^2+(z-z')^2}} dr'] d\varphi' dz'$$

on solving

$$V_{cur} = \frac{\rho_q}{4\pi\varepsilon_\circ} \left[-2L_w z + \left(z+\frac{L_w}{2}\right)\sqrt{\left(R_w^2+\left(z+\frac{L_w}{2}\right)^2\right)} - \left(z-\frac{L_w}{2}\right)\sqrt{\left(R_w^2+\left(z-\frac{L_w}{2}\right)^2\right)} + R_w^2 \ln \frac{\sqrt{\left(R_w^2+\left(z+\frac{L_w}{2}\right)^2\right)}+\left(z+\frac{L_w}{2}\right)}{\sqrt{\left(R_w^2+\left(z-\frac{L_w}{2}\right)^2\right)}+\left(z-\frac{L_w}{2}\right)} \right]$$

(*A*1)

Reference:

1. Griffiths DJ, (2013) Introduction to Electrodynamics, 4th edn., Pearson, Boston

Shruti Sharma
Delhi Technological University